

Investigation of the Magnetic Field
Dependence of the Strongly
Correlated Electron System, SrRu_2O_6

A thesis presented for the degree of
MSc by research

By Luke Cornwell

University of
Kent

School of Physical Sciences

University of Kent

September 2019

Abstract

Ruthenate systems have attracted a large amount of attention due to the interesting physical phenomena that can manifest as a result of the competition between fundamental interactions arising from the $4d$ electrons in the Ru ions. This is exemplified by systems such as Sr_2RuO_4 , a layered perovskite which exhibits superconductivity at a critical temperature, $T_c \approx 1$ K and $\text{Sr}_3\text{Ru}_2\text{O}_7$, an itinerant metamagnet which has been shown to contain spin density waves. Hence ruthenates prove to be promising materials to produce and explore new physics which could lead to new innovative technologies.

More recently the ruthenate, SrRu_2O_6 has been synthesised and shown to have an unusually high antiferromagnetic ordering temperature, $T_N = 565$ K. While the physical properties of SrRu_2O_6 have been studied by several groups, no field dependent studies have yet been reported in the literature. As such the main aim of the research discussed within this thesis was to conduct the first magnetic field dependent study on SrRu_2O_6 .

The structural and magnetic properties were investigated in applied magnetic fields ranging from 0.1 to 7 T, using neutron powder diffraction and DC susceptibility measurements, over a range of temperatures from 1 to 150 K. The hexagonal layered structure of SrRu_2O_6 and its antiferromagnetic order were found to remain constant over both the temperatures and fields studied. With the magnetic moment of the Ru ions being found to have a value of $1.465(18) \mu_B$. In addition to the previously reported anisotropic thermal expansion a positive magnetostriction in the order of $\sim \times 10^{-5} \text{ \AA}$ was observed, over the temperatures and fields studied, suggesting that there are large amounts of magnetoelastic coupling between intralayer Ru^{5+} ions. This is expected to originate from the dominant superexchange interaction mediated by the O ions.

Acknowledgments

Firstly, I would like to thank the University of Kent for funding my research and making it possible, as well as for the opportunities the University has provided me with to further my education and grow as an individual. Similarly, I am extremely grateful for all of the guidance and support provided by my supervisors Donna Arnold and Emma Pugh. I also wish to express my gratitude to Alexandra Gibbs and Fabio Orlandi, from the ISIS Neutron and Muon source, as well as Craig Hiley, for useful discussion.

I would also like to recognise and thank Craig Hiley and Richard Walton, from the university of Warwick, for producing the samples used within this thesis. In addition to Silvia Ramos, D. Arnold, E. Pugh and F. Orlandi for conducting the neutron diffraction experiment, analysed within this thesis, as part of proposal number RB1610324.

I am equally grateful to my fellow postgraduates Kevin Etherdo-Sibley and Richard Dixey for the training and useful discussion they provided. Thanks, should also go to Luke Alesbrook, for his help with the collection of SEM data, and all those not mentioned, who have helped me in my journey such as, Tim Kinnear, Gavin Mountjoy and Mark Price.

Lastly, I would like to thank my family for their support and encouragement, as well as always being there for me when I need them most.

Contents

Abstract.....	i
Acknowledgments.....	ii
Contents.....	iii
List of Acronyms.....	vi
Chapter 1: Introduction.....	1
1.1: Transition Metal Magnetism	1
1.1.1: Magnetisation	3
1.1.2: Types of Magnetism.....	4
1.1.3: Frustrated Magnetism.....	5
1.1.3.1: Geometrically Frustrated Magnetism	6
1.1.3.2: Spin Glasses.....	6
1.1.4: The Exchange Interaction	7
1.1.5: The Heisenberg Model.....	9
1.2: Superconductivity.....	9
1.3: The Current State of Research on 4d and 5d Transition Metal Oxides.....	11
1.4: Previous Work on SrRu ₂ O ₆	16
1.5: Scope of this Work	20
Chapter 2: Experimental Techniques	21
2.1: Diffraction	21
2.1.1: Crystallography	21
2.1.1.1: The Reciprocal Lattice.....	22
2.1.1.2: Lattice Planes and Miller Indices.....	23
2.1.2: X-ray Diffraction	25
2.1.2.1: The Bragg Formulation	26

2.1.2.2: The Von Laue Formulation.....	27
2.1.2.3: Equivalence of the Two Formulations.....	29
2.1.2.4: X-ray Powder Diffraction	30
2.1.2.5: Crystal Structure Refinement from a Powder Diffraction Pattern	30
2.1.3: Neutron Diffraction.....	32
2.1.3.1: Magnetic Scattering of Neutrons	34
2.1.3.2: Neutron Powder Diffraction	34
2.1.3.3: Time-of-Flight Neutron Diffraction	34
2.1.4: Data Analysis, the Rietveld Method.....	35
2.1.5: X-ray Powder Diffraction Experimental Method	38
2.1.6: Neutron Powder Diffraction Experimental Method	38
2.1.7: Rietveld Analysis Using XRD Data	39
2.1.8: Rietveld Analysis Using NPD Data.....	40
2.1.8.1: Refinement of the Magnetic Structure	40
2.1.8.2: Origin of the Magnetic Form Factor for Ru ⁵⁺	42
2.1.9: Errors Associated with GSAS	43
2.1.10: The Le Bail Method	44
2.2: SQUID Magnetometers and Magnetisation Measurements.....	44
2.2.1: The Josephson Effect.....	45
2.2.2: Design and Operation of a SQUID Magnetometer	45
2.2.3: Experimental Method	46
2.3: Scanning Electron Microscopy and Energy dispersive X-ray spectroscopy	47
2.3.1: Design and Operation of an SEM	47
2.3.2: Electron Beam Interactions	48
2.3.2.1: Elastic Scattering Events	48
2.3.2.2: Inelastic Scattering Events	49
2.3.3: Energy Dispersive X-ray Spectroscopy	50

2.3.4: Experimental Method	50
2.4: A Word on Experimental Work	51
Chapter 3: Results.....	52
3.1: Determination of Structure and Purity	52
3.2: Magnetisation Measurements.....	54
3.2.1: Surface Volume Effects	56
3.3: Zero Field Powder Neutron Diffraction Data.....	58
3.4: Applied Field Powder Neutron Diffraction Data	65
3.5: Temperature Dependence of the Nuclear and Magnetic Structures	70
3.6: Magnetoelastic and Magnetostrictive Effects	73
3.7: Nitrogen Contamination	82
Chapter 4: Conclusions.....	90
4.1: Future Research	91
Bibliography.....	92
Appendices	98
Appendix 1.....	100
Appendix 2.....	127

List of Acronyms

AFM	Antiferromagnetic
BSE	Back scattered electron
CCD	Charged-coupled device
EDS	Energy dispersive X-ray spectroscopy
FC	Field cooled
FM	Ferromagnetic
GFM	Geometrically frustrated magnetism
GSAS	General Structure Analysis System
NPD	Neutron powder diffraction
PD	Path Difference
RKKY	Ruderman–Kittel–Kasuya–Yosida
SE	Secondary electron
SEM	Scanning electron microscopy
SDW	Spin density wave
SG	Spin Glass
SQUID	Superconducting quantum interference device
XRD	X-ray powder diffraction
XRF	X-ray fluorescence
ZFC	Zero field cooled

Chapter 1: Introduction

New materials that show novel and complex physical properties are critical for the advancement of technologies, such as those used on board spacecraft, in hospitals and even the phones in our pockets, affecting everyone's lives. As a result, new materials platforms which can provide these exotic properties and/or help determine their underlying physics are of great interest. For this reason, there is a particular interest in materials which contain the $4d$ and $5d$ elements as they typically exhibit competition between fundamental interactions such as the Coulomb and exchange interactions [1]. As a result, this is a very promising area of research with the exciting prospect of uncovering new physics.

Before discussing the research presented within this thesis, on the $4d$ ruthenate SrRu_2O_6 , it is first important to understand some of the relevant theory behind the physics observed. In addition to becoming familiar with the nomenclature used to describe them. This will be the initial focus of this chapter before concluding by discussing the current state-of-the-art in this field of research.

1.1: Transition Metal Magnetism

Magnetism is an emergent phenomenon which arises from how atoms within a material interact with one another and self-organise to produce magnetic properties. In this section we will focus on some of the relevant theory for the magnetism of transition metals. Firstly, atoms have two types of angular momentum, orbital angular momentum, \mathbf{L} , and spin angular momentum, \mathbf{S} , which are determined by the values of L and S for the electrons within the atom, and sum to give a total angular momentum \mathbf{J} :

$$\mathbf{J} = \mathbf{L} + \mathbf{S} \quad (1.1)$$

Atoms are comprised of many electrons however only unfilled shells have a net angular momentum and therefore contribute to the magnetic moment of the atom. In these unfilled shells the electrons spin and orbital angular momenta can combine together in $(2L + 1)(2S + 1)$ different ways, each with a different energy labelled by J ,

due to L-S coupling. This L-S coupling (also known as spin orbit coupling or Russell-Saunders coupling) describes a weak perturbation in the energy determined by electrostatic interactions associated with L and S , arising from spin-orbit interactions, resulting in the splitting of energy levels into fine structure levels labelled by J [2].

Clearly there are many ways in which angular momentum quantum numbers can be combined. The set of quantum numbers which minimise the energy, i.e. belong to the ground state, can be estimated using Hund's rules (listed below) [2]. Note these rules are applied in consecutive order i.e. they follow rule one first, then rule two and so on.

- 1) Electrons are arranged in a way which maximises S while still observing the Pauli principle, that no two electrons can have the same set of quantum numbers, or similarly an orbital can only contain one electron of each spin. Electrons do this to minimise the Coulomb energy.
- 2) After satisfying the first rule electrons try to maximise L and in so doing reduce the Coulomb energy. This can be considered to occur because electrons orbiting in the same direction can remain further apart, as electrons orbiting in opposite directions would continually pass each other becoming very close.
- 3) Lastly the value of J will be at a minimum, $L - S$, if the shell is less than half full or at a maximum, $L + S$, if the shell is more than half full, in order to minimise the spin-orbit energy. Note that the third rule only applies in certain cases as the spin-orbit energy can be small compared to other energies such as the crystal field energy in transition metals which can cause the third rule not to apply.

The ground state can then be labelled by a term symbol given by $^{2S+1}L_J$, where L is written as a letter and not a number according to:

L	0	1	2	3	4	5	6	...
	S	P	D	F	G	H	I	...

Using this information, we can calculate the predicted magnetic moment for an atom using the following equation [2]:

$$\mu = g_J \mu_B \sqrt{J(J+1)} \quad (1.2)$$

Here μ_B is the Bohr magneton with a value of $\mu_B \approx 9.274 \times 10^{-24} \text{ Am}^2$ and g_J is the Landé g-factor:

$$g_J = \frac{3}{2} + \frac{S(S+1) - L(L+1)}{2J(J+1)} \quad (1.3)$$

Although these assumptions work well for 3d and 4f ions they are less successful for heavier ions as the strength of L-S coupling increases and as such they may not be ideal for 4d row elements. Further to this, transition metals experience a reduction in symmetry (resulting in a loss of degeneracy) due to crystal field effects, which can result in a loss of the orbital contribution to the magnetic moment, known as orbital quenching.

1.1.1: Magnetisation

Magnetic materials contain a large number of atoms each with their own moments. To better describe these large number of moments the quantity magnetisation, \mathbf{M} , was defined and represents the magnetic moment per unit volume. Magnetisation therefore also represents the intrinsic induction of a magnetic sample. Due to this intrinsic induction when a magnetic sample is in the presence of an applied field, \mathbf{H} , the total magnetic induction, \mathbf{B} , is the sum of \mathbf{H} and \mathbf{M}

$$\mathbf{B} = \mu_0(\mathbf{H} + \mathbf{M}) \quad (1.4)$$

where μ_0 is the permeability of free space.

In a linear magnetic material the magnetisation is linearly related to the applied magnetic field and can be written as shown in Eq. 1.5 [2]:

$$\mathbf{M} = \chi \mathbf{H} \quad (1.5)$$

Where the magnetic susceptibility, χ , defined as

$$\chi = \frac{\partial \mathbf{M}}{\partial \mathbf{H}} \quad (1.6)$$

can be considered as a measure of how much a material magnetises in an applied field or equivalently as a measure of the moment induced by the field.

1.1.2: Types of Magnetism

The most common types of magnetism are diamagnetism, paramagnetism, ferromagnetism and antiferromagnetism [2]. Diamagnetism in a material is when an applied magnetic field produces a moment which opposes the applied field, thus diamagnetic materials have a negative susceptibility. To a certain extent this effect occurs in all materials with paired electrons, however, it is only weak and is easily dominated by the other stronger forms of magnetism. In complete contrast to this, paramagnetism corresponds to materials that have a positive susceptibility. Physically, paramagnetism describes the weak alignment of randomly orientated moments with an applied magnetic field to produce a net magnetisation and hence an additional magnetic induction, shown in Fig.1.1a.

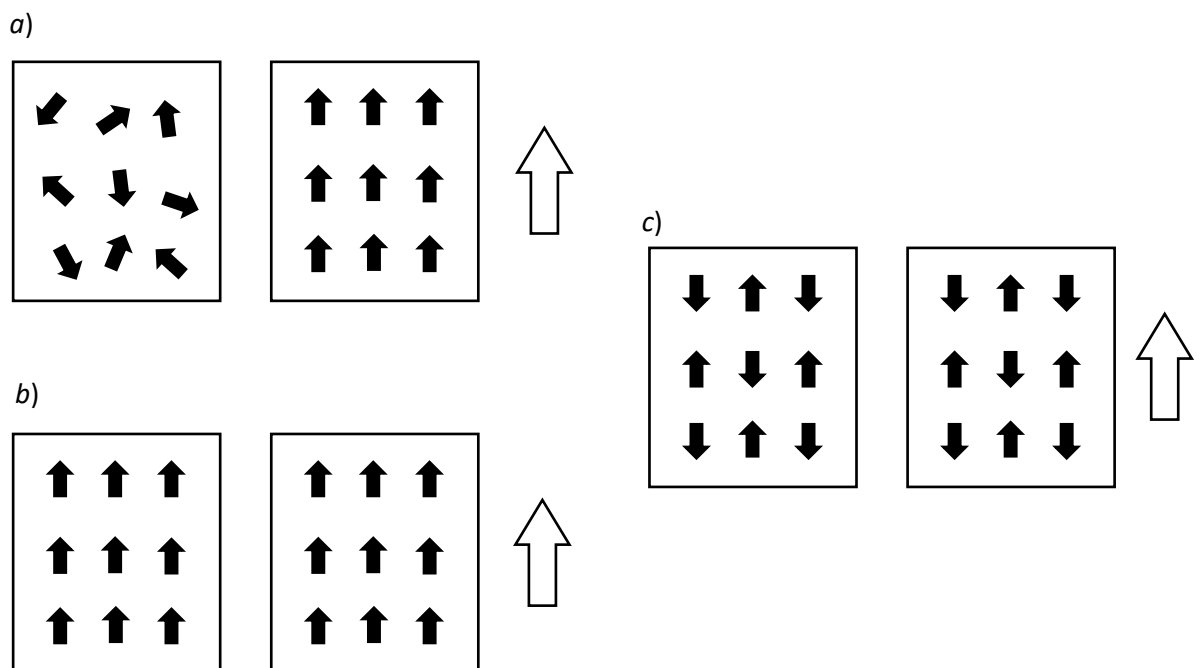


Fig. 1.1: Schematic representation of how magnetic moments order in a) paramagnetic, b) ferromagnetic and c) antiferromagnetic materials. The configurations on the right, next to the large arrows, show how these materials moments order in a magnetic field applied in the direction of the arrow, while the configurations on the left represent the order in zero field [2].

In both of these types of magnetism the magnetic moments only interact¹ very weakly, producing no long range order and acting relatively independently.

On the other hand, moments within a material can interact with one another considerably producing ordered arrangements of magnetic moments, which give rise to spontaneous magnetisation. Ferromagnetism (FM) is one such type of magnetism which shows long range order between magnetic moments, wherein neighbouring moments within a domain align in parallel and can lead to a net magnetisation, even in the absence of an applied magnetic field, as shown in Fig. 1.1*b*. Antiferromagnetism (AFM) also produces long range order only this time the interactions between neighbouring ions cause them to align anti-parallel to each other, Fig. 1.1*c*. Magnetic order has a large dependence on energy, with both FM and AFM materials only ordering beneath a critical temperature, the Curie and Néel temperatures, respectively. Above these temperatures the thermal energy is larger than that gained from ordering and causes disorder, resulting in the material changing to a paramagnetic state. Changes of state such as these are known as magnetic phase transitions.

Further to these types of magnetism, there are other more exotic types of magnetic order, such as ferrimagnetism and helimagnetism however, these will not be introduced here.

1.1.3: Frustrated Magnetism

Another type of less common magnetic order is frustrated magnetism. Broadly speaking there are two types of magnetic frustration, Geometrically Frustrated Magnetism (GFM) and the random distribution of moments known as a Spin Glass (SG). Unlike SG behaviour which arises from conflicting interactions between many randomly distributed moments, GFM occurs due to conflicting interactions that are a direct result of the geometry of the structure.

¹ While there is an interaction between moments due to magnetic dipole, dipole interactions, these are very weak and do not give rise to the magnetic order we commonly observe. These originate from the much stronger Coulomb repulsion as discussed within the section concerning the exchange interaction, section 1.1.4.

1.1.3.1: Geometrically Frustrated Magnetism

In magnetic systems the moments of each atom are vector quantities which can interact with their neighbouring moments; magnetically ordered states occur when there is a gain in potential energy associated with the aligned state. When the interactions between moments are FM all configurations of the moments in any symmetry are equivalent, all aligned with each other, and so no frustration can occur Fig. 1.2a. However, for AFM interactions some systems and geometries can lead to competition between interacting moments leading to an unstable, frustrated state [3].

The most basic and intuitive example of a frustrated system used to demonstrate the concept is a system of three equivalent moments positioned at the corners of a two dimensional equilateral triangle, shown in Fig. 1.2 [4]. In this system once any two moments are aligned anti-parallel to one another an issue occurs with how the third moment should be ordered. As the AFM interaction between each moment are equal; no matter which moment the third spin tries to align anti-parallel to there will be an energy penalty from aligning parallel to the other and hence the state is frustrated. For classical spins frustration can cause a compromise in the spin geometry such as canted or helical order [4].

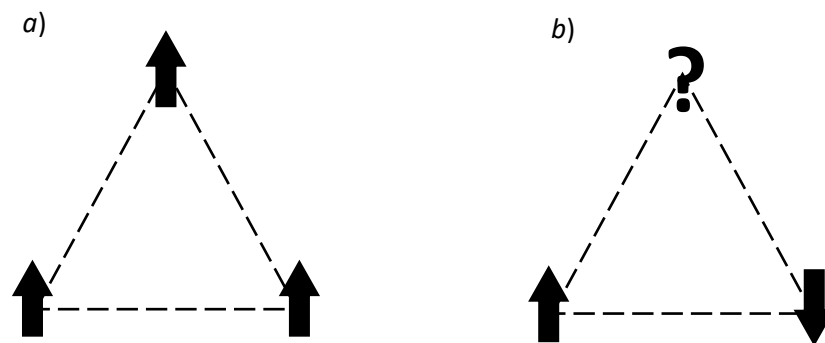


Fig. 1.2: Spin arrangement on a equilateral triangular lattice **a)** for a ferromagnet and **b)** for an antiferromagnet, which is a frustrated system [20].

1.1.3.2: Spin Glasses

A spin glass is a random distribution of magnetic moments that freeze into a glass of spins at a given temperature, known as the freezing temperature (T_f), shown in Fig. 1.3. The term glass is used, as the random order of spins is analogous to the

amorphous structure of a glass [5, 6]. Much like the case for GFM the conflicting interactions between moments occurs due to a frozen in structural disorder. However, these interactions can be far more complicated than in the case of GFM due to spin glass ordering being non-unique. In other words, a spin glass can order in one of many degenerate thermodynamic states described by statistical mechanics each with the same macroscopic state but with different microscopic configurations [6].

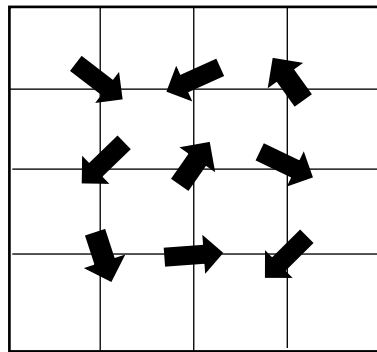


Fig. 1.3: Schematic representation of a 2D spin glass state.

1.1.4: The Exchange Interaction

Within solids, the long range ordering of moments is caused by the exchange interaction. This interaction correlates the spins of unpaired electrons in neighbouring atoms through a combination of Coulomb interactions and the Pauli principle allowing electrons to exchange between the orbitals of adjacent atoms. To describe how this happens one must consider how the Coulomb interaction between electrons and the electrons kinetic energy can be minimised. Firstly, to minimise the Coulomb potential electrons would try to localise themselves tightly to their corresponding ions. However, they also have kinetic energy which is minimised when the electrons are in a plane wave state. In opposition to localisation, plane wave states have a probability distribution which extends uniformly across the crystal lattice. In an attempt to minimise both these energies the electrons make a compromise between the two states resulting in their wave functions being centred on their respective ions with a little overlap to some of the neighbouring ions [2].

Now that the electrons have a small probability of being on a neighbouring ion the spins of the electrons in the neighbouring ions become important. Take for example an electron which has its wave function overlapping with another orbital which already holds one electron. Through Pauli's exclusion principle the electron can only be in this neighbouring orbital if it has a spin of the opposite sign to the one already in the orbital. If it does, then there is a small probability that it can hop into this orbital. Equally, the electron may hop into a shell with an empty orbital but be surrounded by electrons with aligned spins. In this case the Pauli principle does not apply. However, it is favourable for the electrons spin to align with the others according to Hund's first rule. The former case describes antiferromagnetic exchange which makes spins point in opposite directions, and the latter describes ferromagnetic exchange, which tends to make spins align, shown in Fig. 1.4a.

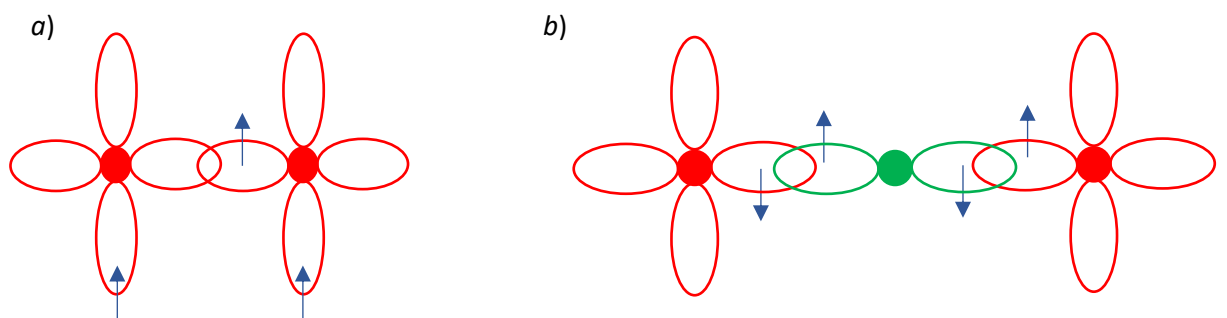


Fig. 1.4: Schematic representation of exchange pathways. Within these figures red represents magnetic ions and their orbitals; green represents a nonmagnetic ion and its orbital, and the blue arrows represent electrons with the corresponding spins. a) Shows ferromagnetic direct exchange and b) shows antiferromagnetic super exchange. Reproduced from [2].

Through either of these mechanisms the ability to transfer to a neighbouring ion, thus decreasing the electrons kinetic energy by spreading out its wave function, depends on the spins of the electrons. Therefore, the spin which maximises its ability to transfer between ions lowers its energy and becomes the preferred direction. So, through these means an unpaired electrons spin can become correlated with the spins of nearby unpaired electrons [2].

The exchange interaction; featuring electrons on neighbouring atoms becoming directly coupled to one another is known as direct exchange. Another form of

exchange interaction is super exchange. This form of exchange sees ions, which are separated by a nonmagnetic ion, correlate with one another through the nonmagnetic ion. This correlation occurs in a similar way to direct exchange, whereby electrons in the magnetic ions can exchange with those in the nonmagnetic ion Fig.1.4b. Similarly, itinerant exchange, also known as indirect exchange, can couple spins over slightly larger distances. In this form of interaction, the coupling is mediated by the itinerant electrons, which are free to move between the magnetic ions and thus propagate magnetic fluctuations [2].

1.1.5 The Heisenberg Model

As we have seen, the associated energy with the exchange interaction, exchange energy, between two atoms is dependent on the spins of the atoms. Applying this dependence to all nearest neighbours leads to the Heisenberg Hamiltonian seen in Eq. 1.7

$$\hat{\mathcal{H}} = - \sum_{\langle ij \rangle} J_{ij} \mathbf{S}_i \cdot \mathbf{S}_j \quad (1.7)$$

where \mathbf{S}_i and \mathbf{S}_j represent the spins of the i^{th} and j^{th} atoms and J_{ij} represents the exchange constant between those two atoms. Note that in the summation, $\langle ij \rangle$ represents the sum over nearest neighbours. Which means the sum is doubled, to account for i 's interaction with j and j 's interaction with i , in addition to the i^{th} and j^{th} terms not corresponding to neighbouring sites being excluded.

The Heisenberg Hamiltonian is an effective Hamiltonian which calculates the energy between neighbours in ordered magnetic materials; forming the bases of the Heisenberg model, which is one of the most popularly used to understand magnetic behaviours as well as mathematically predict them [2].

1.2: Superconductivity

Superconductivity is another example of an emergent phenomena and arguably one of the most interesting. These materials in the superconducting state are characterized by having an immeasurably small electrical resistance and can be considered perfect conductors. Additionally, they also have a susceptibility of $\chi = -1$ i.e. they are perfect

diamagnets and expel all magnetic fields in a phenomenon known as the Meissner effect. There are two types of superconductors: type I which shows the Meissner effect as described above and type II which differs slightly as they allow magnetic flux to penetrate regions of the material when the field exceeds a certain strength, the lower critical field H_{c1} . When this happens tube like regions of field form throughout the material putting it into something known as a vortex state.

The conventional theory of superconductivity proposed by Bardeen, Cooper and Schrieffer, given the name BCS theory, explains superconductivity through the condensation of electrons into weakly bonded Cooper pairs, via the exchange of phonons [7]. The size of these pairs is described by the superconducting coherence length, ξ , which describes the range these pairs can remain bound over. Cooper pairs can pair into a state with a total spin of $S = 0$ or $S = 1$, known as singlet and triplet pairing respectively. The orbital wave function which accompanies a singlet state is symmetric i.e. $L = 0$ (s-wave), $L = 2$ (d-wave) and so on. Whereas the orbital wave function which accompanies the spin-triplet state is antisymmetric i.e. $L = 1$ (p-wave), $L = 3$ (f-wave), etc [8]. More important is the fact that Cooper pairs can exchange partners, which explains the zero resistance in terms of all the electrons becoming correlated and moving as one coherent wave function i.e. the electrons do not actually move to another location, during which they could be scattered and cause resistance but instead they exchange their way through the material.

Cooper pairs can be separated by kinetic, thermal or magnetic interactions described by the critical current density, J_c , critical temperature, T_c , and critical field, H_c or H_{c2} for type II superconductors, respectively. Hence above these critical points the materials will transition to the normal state and no longer remain superconducting. Similar to these, the Pauli limiting field is a theoretical limit for the magnetic field which can be applied before pair breaking due to the Pauli paramagnetism of the electrons occurs [9].

1.3: The Current State-of-the-art of Research on 4d and 5d Transition

Metal Oxides

Opportunities to produce and explore new physics in materials containing heavier transition metals, from the 5th and 6th rows of the periodic table, can be exemplified by the research that has been carried out on Ir, Os and Ru oxide compounds. Some of these compounds such as Sr₂RuO₄, which shows evidence of exotic superconducting pairing, will be discussed here [1].

For 5d iridate compounds the competition between interactions and spin-orbit excitations that can lead to magnetic ground states is not expected due to spin-orbit coupling (L-S coupling) generally dominating [10]. However, magnetic properties have been observed in 6H-hexagonal perovskite iridates, with the chemical formula Ba₃MIr₂O₉ (for M = Mg, Zn, Ca, Sr) [11]. Here the Ir⁵⁺ ions form face-sharing octahedra causing their nearest neighbour to be another Ir⁵⁺ ion and as such it is suggested that super exchange via the O ions becomes important [11], in addition to the direct exchange between Ir ions.

Nag *et al.* [10] presents resonant inelastic x-ray scattering (RIXS) measurements on the 6H-hexagonal Ba₃MIr₂O₉ compounds; a technique which can detect the changes in energy and momentum of inelastically scattered X-rays associated with elementary excitations within the target material [12]. Within an octahedral crystal field the electrons of a 5d⁴ electron configuration would have their spins of $S = 1$ coupled to their orbital angular momenta $L = 1$, normally forming non-magnetic L-S coupled states with $J = 0$ [10]. Contrary to this, the RIXS data collected by Nag *et al.* shows the L-S coupling strength to be lowered, compared to the expected value of 0.4 – 0.5 eV, to ≈ 0.26 eV causing the ground state to deviate from the non-magnetic singlet [10]. They suggest that the enhanced intersite hopping stemming from the small separation between the Ir⁵⁺ ions in these 6H iridates is the cause of the lowered L-S coupling. In addition to their RIXS measurements they performed exact diagonalisation of a minimal two-site model which included Hund's coupling and intradimer hopping terms to compare to their low energy RIXS measurements. They found that the collected

data corresponded to a two-site model with a finite intersite hopping [10], not unsurprisingly considering the direct and super exchange interactions expected.

Another group of 5d transition metal oxides which have produced compounds that show interesting physical phenomena are the osmates pyrochlores (with structures formed from a framework of corner sharing tetrahedra). KOs_2O_6 , found by Yonezawa *et al.* [13], has been shown to have a relatively high superconducting transition temperature ($T_c = 9.6$ K) and has been characterised by electrical resistivity, magnetic susceptibility and specific heat measurements [14]. Structural analysis found the material to crystallise in the β -pyrochlore structure, in which K atoms are located at the O' sites of the ideal pyrochlore oxide, $\text{A}_2\text{B}_2\text{O}_6\text{O}'$, and the A sites are vacant. Resistivity measurements showed a sharp decrease at a temperature of 10 K falling to zero resistance at 9.6 K. Below this temperature diamagnetism associated with the Meissner effect was observed. Additionally, a jump in the specific heat of the material was also reported, suggesting that the superconducting onset temperature is 10 K with $T_c = 9.6$ K.

The superconductivity shown by KOs_2O_6 is unusually unaffected by magnetic field, with a large second critical field of $H_{c2} \approx 38.3$ T, twice the size of the Pauli's limiting field of $H_p = 17.8$ T. This suggests that the superconductivity shown by KOs_2O_6 is unconventional in nature and from μSR experiments [15] it was shown to be a type II superconductor, with a coherence length, $\xi(0) = 3.0$ nm, penetration depth, $\lambda(0) = 270$ nm and a Ginzburg-Landau parameter, $K(0) = 90$. The London penetration, or penetration depth, is the distance which a magnetic field can penetrate into the surface of a superconducting material before it decays to zero and the Ginzburg-Landau parameter is the ratio of the penetration depth to the coherence length i.e. $\frac{\lambda}{\xi}$ [16, 17, 18]. It is suggested that the origin of this superconductivity, capable of withstanding high fields, is related to electron correlations near a metal-insulator transition and the frustration of the pyrochlore lattice.

Ruthenate systems show many unusual magnetic and electronic properties. Sr_2RuO_4 , one of the most famous of these was found to be superconducting by Maeno *et al.* [19] from AC susceptibility and resistivity measurements, which showed strong

diamagnetism and a drop in resistivity to zero. Sr_2RuO_4 is a layered perovskite with a tetragonal K_2NiF_4 -type structure, shown in Fig. 1.5a, [8, 19] and a superconducting transition temperature, $T_c \sim 1 \text{ K}$ [20].

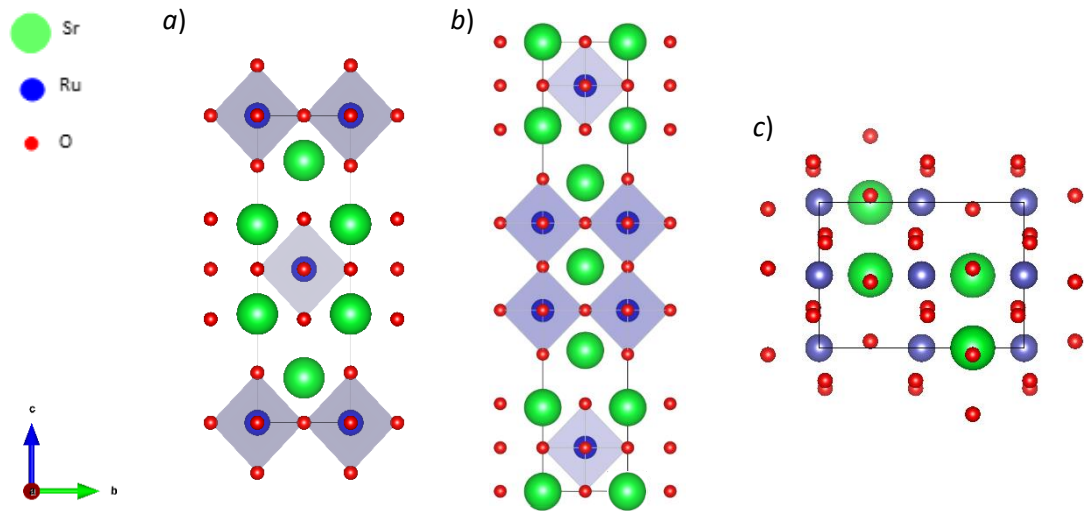


Fig. 1.5 a, b and c: Representations of the crystal structures of Sr_2RuO_4 [19], $\text{Sr}_3\text{Ru}_2\text{O}_7$ [21] and SrRuO_3 [22] shown parallel to the c -axis. Green spheres represent Sr atoms, blue Ru atoms and red O atoms.

Furthermore, Sr_2RuO_4 is isostructural to the high T_c superconductor $\text{La}_{2-x}\text{Ba}_x\text{CuO}_4$ and shares a similar electronic structure to the cuprate superconductors. The material features Ru-4d and O-2p hybridisation which dominates the states near the Fermi level. Strong Coulomb correlations between electrons are also suggested by their larger effective masses [19].

Further to this, Sr_2RuO_4 is an unconventional superconductor believed to have spin-triplet Cooper pairing, corresponding to p-wave superconductivity, instead of the conventional singlet, s-wave, Cooper pairing. This is evidenced by the observation of a change in the spin susceptibility measured by the NMR Knight shift [23], which suggests spin-triplet pairing due to singlet Cooper pairs having no spin susceptibility [19]. While s-wave superconductivity is insensitive to scattering from disorder this is not the case for unconventional superconductivity which is affected by strong scattering at the Fermi surface [24]. Here strong refers to scattering with an elastic mean free path equal to the superconducting coherence length [25] meaning that the shorter the coherence length the smaller the constraints on the sample purity [19]. This in turn explains why unconventional superconductivity took so long to find and

why most of the best known examples have small coherence lengths. Another interesting feature is that Sr_2RuO_4 is intrinsically superconducting, whereas the cuprate superconductors are typically a product of carrier doping an insulating parent compound, which creates new states within the correlation gap at the Fermi level [19].

$\text{Sr}_3\text{Ru}_2\text{O}_7$ is the $n = 2$ member of the Ruddlesden-Popper series $\text{Sr}_{n+1}\text{Ru}_n\text{O}_{3n+1}$, also a layered perovskite with an orthorhombic unit cell and a $I4/mmm$ space group [21, 26], shown in Fig. 1.5b. The symmetry is lowered from tetragonal to orthorhombic as a consequence of the oxygen octahedra being rotated in the a - b plane by approximately 6.8° . The electronic structure of the materials is based on partially filled bands formed from the hybridisation of Ru $4d$ levels with O $2p$ states, as seen to occur for many of the ruthenates [27].

In its ground state $\text{Sr}_3\text{Ru}_2\text{O}_7$ is a paramagnetic Fermi liquid [28], where the Fermi liquid phase extends up to 10–15 K in zero field and is suppressed to zero as the critical field of $B_c \approx 8$ T (for B parallel to the c -axis) is approached [29]. The electronic specific heat of $\text{Sr}_3\text{Ru}_2\text{O}_7$ is also amongst the highest in any oxide, with $\gamma = 110$ mJ/molRuK² [28]. Further to this and crucial to its popularity, it has been shown to be an itinerant metamagnet with $B_c \approx 7.95$ T [30, 31]; i.e. a material that undergoes a sudden change to a highly magnetised state when a certain strength of magnetic field is applied [32, 33]. This is believed to be caused by its proximity to ferromagnetism [34] as well as there being a local minimum or maximum in the density of states at the Fermi level. These minima or maxima may result from a van Hove singularity, as proposed by angle resolved photo-emission spectroscopy [29].

The critical field of approximately 8 T (for B parallel to the c -axis) which is responsible for destroying the Fermi liquid behaviour at low temperatures has also been shown to produce field tuneable spin density waves (SDW) [31]. Two phases of SDW have been observed, the first, A phase, was observed between 0 and 1 K for fields from 7.95 to 8.1 T, and the second, B phase, was observed between 0 and 0.5 K for fields from 8.1 to 8.4 T. This was observed in neutron diffraction experiments as satellite peaks in reciprocal space, corresponding to an ordered moment modulated in space characteristic of SDW [31]. These results were further supported by the fields and temperatures at which magnetic order disappeared coinciding with the phase

boundaries determined by anomalies in the susceptibility, resistivity and magnetostriction measurements. Additionally, the direction of the applied magnetic field was found to control the SDW population and similarly can explain the resistivity anisotropic behaviour observed by Grigera *et al.* [35].

Reich *et al.* [22] performed AC susceptibility and DC magnetisation measurement on single crystal and sintered samples of SrRuO₃, shown in Fig. 1.5c. DC measurements showed ferromagnetic behaviour, while the AC measurements showed a sharp peak at 167.6 K, at a frequency of 1000 Hz. Below this temperature the susceptibility was found to be finite and did not appear to be limited by the demagnetisation factor. These results are not expected from a ferromagnet below its curie temperature, $T_c \approx 167$ K. The AC susceptibility measurements for both the single crystal and sintered samples showed AC maxima at T_c , which was found to shift to higher temperatures with an increase in field strength [22]. The amplitude of these peaks $\sim 10^{-2}$ emu/g is comparable in size to that observed in spin glass systems such as Eu_{0.2}Sr_{0.8}S, of 1.6×10^{-2} emu/g [36].

Field cooled (FC) (10000 Oe) AC measurements, collected at different frequencies show a frequency dependence of the maximum in the susceptibility where by the peak is found to shift to higher temperatures and decrease in amplitude with an increase in frequency, a trend characteristic of spin glasses [22]. Further to this a large divergence was observed between FC and zero field cooled (ZFC) DC data, below the freezing temperature of $T_f = 163$ K, as well as the ZFC curve featuring a cusp at T_f . All of these features are again characteristic of a spin glasses.

Spin glass behaviour is predominantly found to originate in systems which would typically be expected to exhibit antiferromagnetic order and/or frustration. Therefore, it is somewhat unusual to see it occur for a system suggested to be ferromagnetic, with no obvious geometric frustration, such as SrRuO₃ [37]. To explain this irregularity Reich *et al.* [22] proposed that covalence between the Ru and O ions is responsible for producing the necessary frustration to allow spin glass formation in pure SrRuO₃.

Another ruthenate system showing frequency dependence and FC - ZFC divergence characteristic of a spin glass is the hollandite, K_xRu_{4-y}Ni_yO₈ [38], which shows spin glass

behaviour below $T_f = 28$ K. In agreement with the results from the AC and DC susceptibility measurements, the isothermal remnant magnetisation was found to decay exponentially with time and remain nonzero across the whole temperature range studied, which is consistent with the results of other spin glass systems [39]. Hollandites have the general formula of $A_xM_8O_{16}$, where A is usually an alkali or alkaline earth metal and M is a transition metal. They crystallise into a structure that can be described as a network of corner sharing and edge sharing MO_6 octahedra which form tube like structures, at the centre of which lie the A cations. This structure can be related to geometrically frustrated triangular lattices by considering the Hollandite structure to come from rolling infinite MO_6 layers to form 1D tubes [40]. X-ray diffraction measurements showed the samples of $K_xRu_{4-y}Ni_yO_8$ synthesised in the study by Vera Stimpson *et al.* [38], to crystallise into a tetragonal $I4/m$ symmetry, corresponding to the Hollandite structure, with Ni and Ru disordered over the MO_6 framework. X-ray Fluorescence (XRF) spectroscopy suggested the final approximate composition of the samples was $K_{0.73(3)}Ni_{1.9(5)}Ru_{2.1(5)}O_8$. The total observed moment of $4.8 \mu_B$ was significantly lower than the calculated moment for each formula unit of $8.1 \mu_B$ [38]; this could be due to the hybridisation between $4d$ and $2p$ orbitals in the RuO_6 octahedra, however, this was not suggested as the cause for the glassy behaviour. Instead the authors attribute this behaviour to the nature of the frustrated structure and B-site cation disorder leading to the spin glass formation. It is believed that different strength spin correlations arise from Ni-Ni, Ni-Ru and Ru-Ru Interactions [38].

1.4: Previous Work on $SrRu_2O_6$

As we can see (strontium) ruthenate systems show many interesting phenomena. $SrRu_2O_6$, the subject of this thesis, exhibits an unusually high antiferromagnetic (AFM) ordering temperature, with a Néel temperature, T_N , of 565 K [41, 42]. This is interesting because the layered structure of $SrRu_2O_6$ (discussed in more detail below) allows its AFM order to be easily destroyed, by inducing quantum fluctuations through doping or pressure [43]. It is believed that AFM fluctuations near the AFM boundary could mediate singlet Cooper pairing in unconventional superconductors [43, 44]. Therefore, it may be the case that $SrRu_2O_6$ could be a parent compound for an unconventional superconductor [43]. In addition to this it is a new materials platform

to allow the study of the mechanisms which lead to high temperature magnetic order in 4d transition metal oxides.

SrRu_2O_6 was first reported by Hiley *et al.* [41] in 2014 and has since been studied by several other groups [42, 43, 45]. The structure was reported as a layered oxide with a quasi-two-dimensional structure [41, 42, 45]. This structure consists of stacks of honeycomb lattice planes of Ru^{5+} ions which form alternating layers of edge sharing RuO_6 octahedra, with octahedrally co-ordinated Sr^{2+} residing between the layers forming a hexagonal lattice, Fig. 1.6. This can equally be described as a PbSb_2O_6 type structure; which has a $P\bar{3}1m$ space group and hexagonal unit cell with lattice constants $a = b = 5.20573 \text{ \AA}$ and $c = 5.23454 \text{ \AA}$ [41].

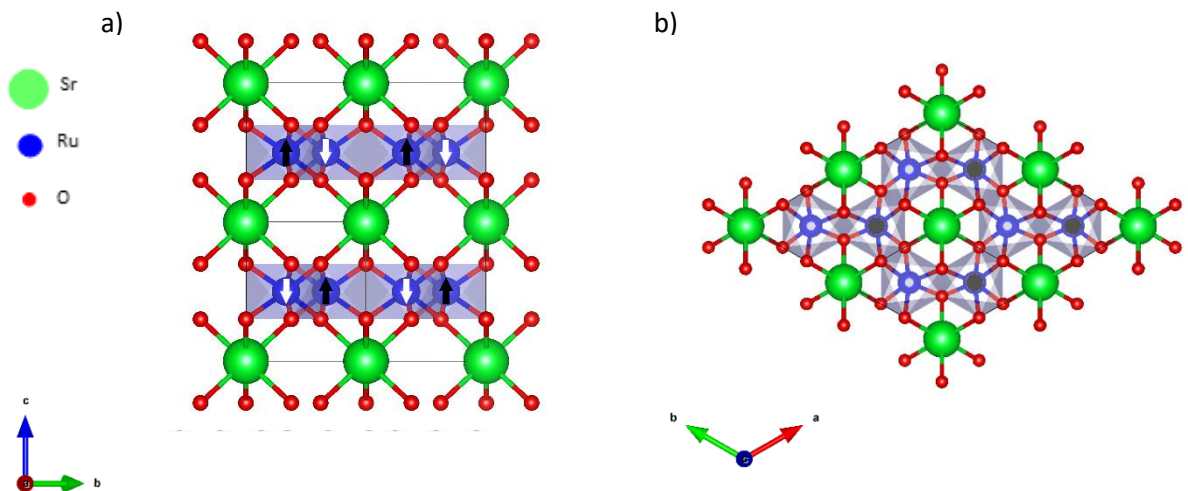


Fig. 1.6 : The crystal structure of SrRu_2O_6 shown perpendicular to the c -axis, a), and parallel to the c -axis, b). Green represents the Sr atoms, blue the Ru atoms and red the oxygen atoms. Black arrows represent spin up moments and white spin down. [reproduced using the experimental data discussed in this thesis using VESTA].

In a later study by Hiley and others [46] it was found that the c lattice constant increased with temperature, while the a constant slightly decreased from 5.20652 \AA , at 7.5 K , to 5.20560 \AA , at 313 K , before remaining constant up to 623 K . It is suggested that this anisotropic thermal expansion could be attributed to magneto-elastic coupling between Ru ions in the ab plane; seeing that the Ru-Ru interlayer distance remains constant over the temperature range studied by Hiley and others [46]. This

anisotropic expansivity continues above the Néel temperature, T_N , and thus strong intralayer coupling, on a local scale, could be present above this temperature.

From *in-situ* powder neutron diffraction (PND) the same study found the Ru^{5+} ions to have a magnetic moment directed along the c -axis with a value of $\mu_{\text{Ru}} = 1.425 \mu_B$ at 7.5 K. This is smaller than the spin only value expected for a d^3 ion, of $3.78 \mu_B$ [41]. The magnetic structure of SrRu_2O_6 can be indexed to have a $P\bar{3}1c$ space group, with lattice constants $a = 5.20573(3) \text{ \AA}$, $c = 10.46908(14) \text{ \AA}$ (46). The spins of the Ru moments are arranged so that there is antiferromagnetic ordering within the ab plane (intralayer) and along the c -axis (interlayer) also shown in Fig. 1.16. This type of ordering is hexagonal type II, as classified by Goodenough [47].

In addition to neutron diffraction, susceptibility and resistivity measurements have been made by different groups [42, 46]. Measuring resistivity as a function of temperature Hiley and others observed the resistivity of SrRu_2O_6 to decrease with temperature and showed SrRu_2O_6 to be a semiconductor [46]. Furthermore, the magnetic susceptibility measurements by Hiley and others and Tian *et al.* show that above room temperature the susceptibility increases with temperature [42, 46]. When the Néel temperature, $T_N = 565 \text{ K}$, is reached there is a discontinuity and then above T_N the temperature dependence is linear up to $\approx 800 \text{ K}$; the maximum temperature studied [42]. Similar behaviour has been seen in some iron-based superconductors and at 400 K the susceptibility is comparable to that of iron pnictides [48]. In these materials the susceptibility characteristics shown are thought to originate from the coexistence of local and itinerant electrons [42, 46].

Theoretical studies by Streltsov *et al.* [49] and Okamoto *et al.* [50] using Density Functional Theory (DFT) and Dynamical Mean Field Theory (DMFT) also suggest that SrRu_2O_6 has both localized and itinerant electrons. They suggest that molecular orbitals dominate the electronic structure. Wherein, each electron is localised to a particular Ru_6 hexagon and delocalized over those six Ru sites. This model is consistent with nearest neighbour antiferromagnetism and has an excitation gap which prevents ferromagnetic bands from forming [43], consistent with the observed magnetic properties [42, 46]. DFT calculations, used to calculate the electronic structure, presented in three papers by Hiley and others, Tian *et al.* and Singh show that there is

strong Ru $4d$ and O $2p$ hybridization in the valence band which is thought to be the cause of the reduction in the Ru magnetic moment [42, 45, 46].

Within SrRu_2O_6 the Ru atoms are Ru^{5+} ions, with half-filled t_{2g} shells. It is the case that $4d$ orbitals, such as these overlap significantly with neighbouring atoms leading to generally covalent electronic structures [45]. In addition to the DFT calculations reported in several papers this suggests a large amount of covalence between the Ru and O atoms in these materials. Connected to this, an increase in covalence should increase the inter-site interactions and with it the ordering temperature [45]. Hence it is believed that hybridisation is also responsible for the high ordering temperature of SrRu_2O_6 [43, 45]

It is unusual for $4d$ and $5d$ oxides to be magnetic, unlike $3d$ oxides which are commonly magnetic. This is a consequence of the $4d$ shell being more extended than the $3d$ shell. Meaning that the Coulomb integrals which give rise to the on-site exchange interaction are smaller for $4d$ elements than for $3d$ elements [45]. However, SrRu_2O_6 has two processes contributing to the exchange interactions: There is direct overlap between half filled, Ru, t_{2g} orbitals leading to a second order AFM interaction and there is AFM super exchange coupling between the O p_z and Ru d_{zx} and d_{yz} orbitals of neighbouring atoms.

A more recently published study which performed Raman spectroscopy measurements on SrRu_2O_6 has been reported by Ponosov *et al.* [51]. They conclude that the concept of the delocalisation of electrons across a particular Ru_6 hexagon explains the non-Heisenberg magnet characteristics presented by DFT calculations [49]. It also predicts that molecular orbitals can manifest in experimental spectra due to certain selection rules. However, the molecular orbital picture is less agreeable with $d-d$, direct exchange between Ru, and strong on site correlation effects [51]. Also, of note is the fact that molecular orbitals are commonly found in materials having structures with complex clusters of transition metals or when such a structure is formed in a structural phase transition. This is not the case for SrRu_2O_6 and yet it still shows properties related to molecular orbitals forming. Ponosov *et al.* suggests that this is similar to benzene molecules in which molecular orbitals appear due to the specific symmetry of

d-p-d electronic hopping on a honeycomb lattice [51]. This Raman study also found no new phonon lines near T_N , excluding a structural phase change at this point.

Even more recently, a study by Suzuki *et al.* [52], performed inelastic neutron scattering experiments on SrRu₂O₆ finding many of the same results reported by the others [41, 42, 43, 45, 46]. However, they suggested that the extended molecular orbitals suggested by Streltsov *et al.* and Okamoto *et al.* may not be necessary as their results can be explained using a nearest neighbour exchange, Heisenberg model, which suggests that the valence electrons are in the localised regime [49, 50, 52].

1.5: Scope of this Work

SrRu₂O₆ is clearly an interesting material with much research having been and still being carried out. However, although the magnetic properties have been investigated no magnetic field dependent studies have yet been reported. The main aim of the work presented in this thesis is to perform a magnetic field dependent study to further investigate the magnetic properties of SrRu₂O₆ originating from strong correlations between electrons. In addition, this work further extends the current knowledge base for this exciting material; which is important if we are to truly understand the complexities of SrRu₂O₆.

To do this, among other measurements, a temperature and magnetic field dependent neutron powder diffraction study was carried out on the WISH instrument at the ISIS Neutron and Muon Source (UK). Data were collected over a range of temperatures from 1 to 150 K in applied magnetic fields from 0.1 to 7 T. Analysis of the data collected allowed the magnetostrictive properties of SrRu₂O₆ to be determined for the first time as well as providing further evidence to support many of the previously reported results. In addition, this thesis presents evidence for nitrogen contamination observed in the neutron powder diffraction data, as confirmed by Rietveld refinement.

Chapter 2: Experimental Techniques

This chapter describes the experimental techniques and methods used to collect and analyse the data presented within this thesis. In addition to this, further relevant theory is also presented. To begin with the samples used to collect all of the data within this thesis were prepared by Craig I. Hiley and Richard I. Walton. A full explanation of their synthesis can be found in reference [41]. The samples received were in powdered form and were used as received.

2.1: Diffraction

2.1.1: Crystallography

Within a crystalline solid the constituent atoms are arranged in an ordered manor which repeats itself throughout the crystal. Therefore, the crystal structure of any crystalline solid can be described as consisting of identical copies of a physical unit, called a basis, repeated at all the points of a Bravais lattice. The Bravais lattice is a set of points which represent the periodical arrangement of the crystal's constituents and can be defined as follows: A Bravais Lattice consists of all the points which have position vectors \mathbf{R} of the form:

$$\mathbf{R} = n_1\mathbf{a}_1 + n_2\mathbf{a}_2 + n_3\mathbf{a}_3 \quad (2.1)$$

Here \mathbf{a}_1 , \mathbf{a}_2 and \mathbf{a}_3 are any three vectors, not all in the same plane, and n_i represents the integer values required to reach the n^{th} point of the lattice [53]. From this definition of the Bravais lattice it is clear that any point within the lattice can be reached by combining an integer number of the three vectors \mathbf{a}_j . Hence, \mathbf{R} is said to be generated by the vectors \mathbf{a}_j , which are given the name primitive vectors. These primitive vectors also define the unit cell of the crystal. This is the smallest possible choice of repeat unit which reflects the entire symmetry of the crystal and is also known as the conventional unit cell [54]. In three dimensions there are fourteen different Bravais lattices which represent seven crystal systems as shown in Table 2.1.

Table 2.1: Table showing the fourteen Bravais lattices, which crystal system they belong to and the geometric conditions associated with each system [53].

Crystal System	Conditions	Bravais Lattices			
		Primitive	Base-centred	Body-centered	Face-centred
Triclinic	$a_1 \neq a_2 \neq a_3$ $\alpha \neq \beta \neq \gamma$	✓			
Monoclinic	$a_1 \neq a_2 \neq a_3$ $\alpha = \beta = 90^\circ \neq \gamma$	✓	✓		
Orthorhombic	$a_1 \neq a_2 \neq a_3$ $\alpha = \beta = \gamma = 90^\circ$	✓	✓	✓	✓
Tetragonal	$a_1 = a_2 \neq a_3$ $\alpha = \beta = \gamma = 90^\circ$	✓		✓	
Rhombohedral /Trigonal	$a_1 = a_2 = a_3$ $\alpha = \beta = \gamma < 120^\circ \neq 90$	✓			
Hexagonal	$a_1 = a_2 \neq a_3$ $\alpha = \beta = 90^\circ \gamma = 120^\circ$	✓			
Cubic	$a_1 = a_2 = a_3$ $\alpha = \beta = \gamma = 90^\circ$	✓		✓	✓

2.1.1.1: The Reciprocal Lattice

For considering things such as crystal diffraction, which is essentially the study of waves incident on scatterers with a periodicity of the Bravais lattice, it is convenient to use the reciprocal lattice construct. The reciprocal lattice is defined as the set of all wave vectors \mathbf{K} that yield plane waves with the periodicity of a given Bravais lattice [53]. For a plane wave, $e^{i\mathbf{K} \cdot \mathbf{r}}$, to have a periodicity of a Bravais lattice of points, \mathbf{R} , the following relation must be true for all \mathbf{R} no matter the value of \mathbf{r} :

$$e^{i\mathbf{K} \cdot (\mathbf{r} + \mathbf{R})} = e^{i\mathbf{K} \cdot \mathbf{r}} \quad (2.2)$$

Taking $e^{i\mathbf{K} \cdot \mathbf{r}}$ out of the expression the reciprocal lattice can be defined as the set of all wave vectors \mathbf{K} which satisfy the expression:

$$e^{i\mathbf{K} \cdot \mathbf{R}} = 1 \quad (2.3)$$

Note that when referring to the reciprocal lattice the Bravais lattice which defines it is often referred to as its direct lattice. Given that a Bravais lattice has primitive vectors \mathbf{a}_1 , \mathbf{a}_2 and \mathbf{a}_3 , the reciprocal lattices primitive vectors are given by:

$$\mathbf{b}_1 = 2\pi \frac{\mathbf{a}_2 \times \mathbf{a}_3}{a_1(a_2 \times a_3)} \quad (2.4)$$

$$\mathbf{b}_2 = 2\pi \frac{\mathbf{a}_3 \times \mathbf{a}_1}{a_2(a_3 \times a_1)} \quad (2.5)$$

$$\mathbf{b}_3 = 2\pi \frac{\mathbf{a}_1 \times \mathbf{a}_2}{a_3(a_1 \times a_2)} \quad (2.6)$$

From Eulers formula, $e^{i2\pi} = 1$, it can be seen that for $e^{i\mathbf{K} \cdot \mathbf{R}}$ to equal one, $\mathbf{K} \cdot \mathbf{R}$ must be an integer multiple of 2π . Since $\mathbf{K} = k_1\mathbf{b}_1 + k_2\mathbf{b}_2 + k_3\mathbf{b}_3$ and $\mathbf{R} = n_1\mathbf{a}_1 + n_2\mathbf{a}_2 + n_3\mathbf{a}_3$, where k_i and n_j are integer values, one can verify that the reciprocal lattice vectors must take the form of E.q 2.4 – 2.6 in order for Eq. 2.3 to be satisfied i.e. \mathbf{b}_i must satisfy $\mathbf{b}_i \cdot \mathbf{a}_j = 2\pi\delta_{ij}$. Here δ_{ij} is the Kronecker delta function which is equal to 1 for $i = j$ and 0 otherwise.

2.1.1.2: Lattice Planes and Miller Indices

There are many ways in which a Bravais lattice can be separated into planes of points known as lattice planes, shown in Fig. 2.1, with each adjacent plane separated by a distance, d . The term '*family of lattice planes*' is used to describe a set of equally spaced, parallel, lattice planes which intersect all points within a Bravais lattice. The reciprocal lattice can be related to families of lattice planes by the following theorem: "*For any family of lattice planes separated by a distance d , there are reciprocal lattice vectors perpendicular to those planes, the shortest of which has a length $2\pi/d$.*" [53]. An example of a reciprocal lattice vector can also be seen in Fig. 2.1.

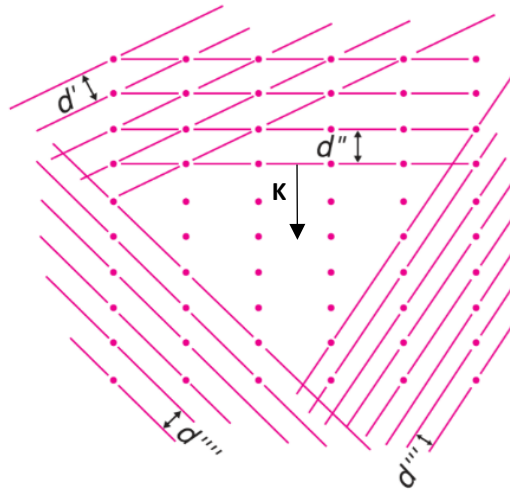


Fig. 2.1: A 2D representation of how a Bravais lattice can be separated into planes of points each with a different d -spacing. The direction of the reciprocal lattice vectors associated to one of the planes have also been included. Edited and reproduced from [55].

Lattice planes are described by three numbers known as Miller Indices. These numbers are the reciprocal values of the fractional lattice plane-unit cell intercepts and are labelled h, k, l . Miller indices can be calculated by finding the intercept of the plane with the unit cell, in units of the lattice vectors. Then by converting these numbers to their reciprocal values and multiplying by the factor which produces the smallest set of integers, one arrives at the Miller indices for that lattice plane. See Fig. 2.2 for an example of the corresponding lattice intercepts and Miller indices.

A plane which is parallel to a unit cell vector never crosses it and thus its Miller index, for the corresponding vector, is given a value of zero. Parentheses, (hkl) , are used to represent a set of Miller indices and a set of braces, $\{hkl\}$, are used to indicate sets of planes that are equivalent due to the symmetry of the crystal. For instance, in a cubic crystal the (100) , (010) , (001) planes are all equivalent and are collectively labelled $\{100\}$, shown in Fig. 2.2 [55].

The separation between any two adjacent lattice planes, d -spacing, for a cubic crystal is given by the following formula:

$$\frac{1}{d^2} = \frac{h^2+k^2+l^2}{a^2} \quad (2.7)$$

It is also worth noting the formula for a Hexagonal crystal, due to its relevance to the material discussed within this thesis:

$$\frac{1}{d^2} = \frac{4}{3} \left(\frac{h^2 + hk + k^2}{a^2} \right) + \frac{l^2}{c^2} \quad (2.8)$$

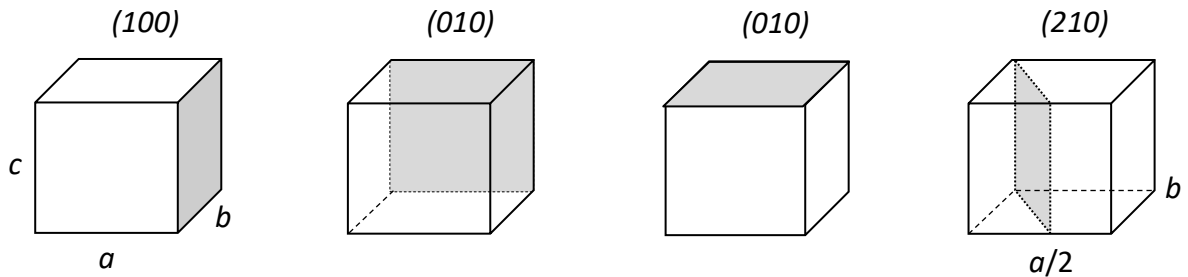


Fig. 2.2: Diagram representing the equivalence of the $\{100\}$ planes and showing an example of the miller indices which correspond to a set of lattice plane-unit cell intercepts. Reproduced from [55].

2.1.2: X-ray Diffraction

Diffraction techniques such as X-ray diffraction are the most commonly used methods for determining the crystal structure of a material. This is made possible using the knowledge of the formulations for the diffraction of X-rays from a crystal, which are discussed in this section. X-rays are a form of electromagnetic (EM) radiation which have a wavelength lying within a range of 10^{-12} and 10^{-8} m. This form of radiation is comprised of photons, a fundamental quantum particle that exhibits both wave and particle like properties [56]. It is also well known from experiments such as the famous Young's double slit experiment that EM waves, as with all waves, can interfere to produce interference patterns. This arises from the fact that when waves which are in phase meet they produce constructive interference; while waves that are out of phase produce destructive interference. Since many scattered rays combining constructively to produce a single beam constitutes a definition of a diffracted beam it is clear that diffraction and interference are one and the same thing [56]. It is due to these properties that X-rays can be diffracted by atoms, which behave as scatterers.

2.1.2.1: The Bragg Formulation

Considering that crystals are made up of parallel lattice planes of atoms: when X-rays are incident on these planes some of the rays are reflected while others pass through the plane and reflect from later planes, shown in Fig. 1.3 [2].

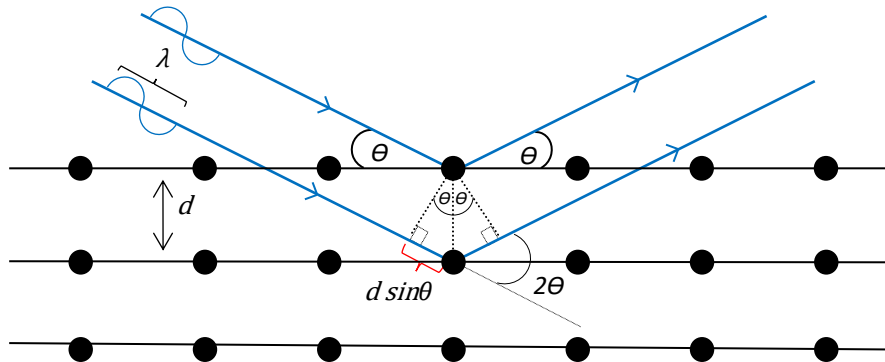


Fig. 2.3: A schematic representation of Bragg diffraction, showing that half the path difference is given by $d \sin\theta$. The blue lines represent X-rays incident on the black lattice planes. [56]

Assuming specular¹ reflection the path difference (PD) between rays reflected from consecutive planes is given by Eq.2.9, where d is the spacing between planes and θ is the angle of incidence.

$$PD = 2d \sin\theta \quad (2.9)$$

If the path difference is an integer number of wave lengths, then the resulting phase difference will be zero and the rays will interfere constructively. This leads to the condition for interference known as the Bragg condition, first put forward by W. H. and W. L. Bragg, Eq. 2.10:

$$n\lambda = 2d \sin\theta \quad (2.10)$$

Here λ is the wavelength of the X-ray photons and n is the order of diffraction, which must take an integer value. For a given wavelength and d only certain θ , known as Bragg angles, will produce a diffracted beam resulting in intense peaks of scattered radiation, known as Bragg peaks. Hence, there can be several angles of incidence

¹In Specular reflection the angle of reflection is equal to the angle of incidence.

which lead to Bragg peaks because n can take any integer value which does not cause $\sin\theta$ to exceed a value of 1 i.e. the condition represented in Eq. 2.11:

$$\frac{n\lambda}{2d} = \sin\theta < 1 \quad (2.11)$$

A corollary of this is that $n\lambda$ must be less than $2d$ and since the smallest value n can take is 1 it follows that the condition for diffraction at any angle is $\lambda < 2d$. In other words, the wavelength of the X-ray radiation used to probe a material must be less than twice the interatomic spacing of the sample.

2.1.2.2: The von Laue Formulation

Crystals are generally three dimensional meaning that equations describing diffraction using vectors are more useful and more generalised than the scalar approach in the Bragg formulation. The von Laue formulation does just this regarding a crystal to be comprised of identical scatterers (atoms) placed at the sites, \mathbf{R} , of a Bravais lattice. In this model each scatterer reradiates incident radiation in all directions. However, sharp peaks in radiation will only be observed in directions and for wavelengths at which the scattered rays coming from all sites interfere constructively [53].

For rays incident on scatterers separated by a displacement vector \mathbf{d} , along a direction $\hat{\mathbf{n}}$, with a wave vector $\mathbf{k} = 2\pi\hat{\mathbf{n}}/\lambda$ and wavelength λ . The scattered² rays will be along a direction $\hat{\mathbf{n}}'$ with a wave vector $\mathbf{k}' = 2\pi\hat{\mathbf{n}}'/\lambda$ and wavelength λ , shown in Fig. 2.4. The path difference can be expressed as shown in Eq. 2.12:

$$PD = d\cos\theta + d\cos\theta' = \mathbf{d} \cdot (\hat{\mathbf{n}} - \hat{\mathbf{n}}') \quad (2.12)$$

²Here it is assumed that the rays are scattered elastically and that no energy is lost; which is a fair assumption as the majority of radiation is scattered in this way. Radiation can also be inelastically scattered and provide information regarding the phonon dispersion, but this will not be introduced here.

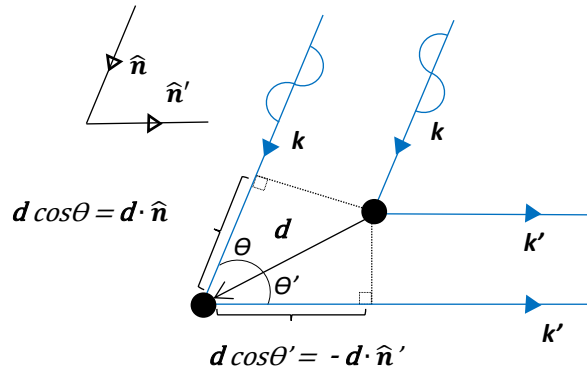


Fig. 2.4: A diagram representing the path difference between rays scattered by two scatterers separated by the vector \mathbf{d} . The rays are incident along a direction $\hat{\mathbf{n}}$ with a wave vector \mathbf{k} and are scattered in a direction $\hat{\mathbf{n}}'$ with a wave vector \mathbf{k}' . [53]

Again, the condition for constructive interference is that the path difference between rays must be an integer number of wavelengths, thus the condition in Eq. 2.13 must be met, where m is an integer.

$$m\lambda = \mathbf{d} \cdot (\hat{\mathbf{n}} - \hat{\mathbf{n}}') \quad (2.13)$$

Multiplying both sides of Eq. 2.13 by $2\pi/\lambda$, to put things in terms of wave vectors, leads to Eq. 2.14:

$$2\pi m = \mathbf{d} \cdot (\mathbf{k} - \mathbf{k}') \quad (2.14)$$

Considering that all sites of a Bravais lattice are displaced from one another by the Bravais lattice vector \mathbf{R} . The condition for rays from all sites to constructively interfere is that Eq. 2.14 holds for all \mathbf{d} equal to \mathbf{R} . Combining this with Euler's relation results in Eq. 2.15:

$$\mathbf{R} \cdot (\mathbf{k} - \mathbf{k}') = 2\pi m \rightarrow e^{i(\mathbf{k}' - \mathbf{k}) \cdot \mathbf{R}} = 1 \quad (2.15)$$

Labeling the change in wave vector, $(\mathbf{k}' - \mathbf{k})$, as \mathbf{K} shows that Eq. 2.15 is the condition, Eq. 2.3, that a set of wave vectors \mathbf{K} must satisfy to define the reciprocal lattice of \mathbf{R} , shown in Fig. 2.5. Hence, one can state that the Laue condition for interference is that the change in wave vector between incident and scattered rays must be a vector of the reciprocal lattice [53]. Note that it is possible to write $(\mathbf{k} - \mathbf{k}') = (\mathbf{k}' - \mathbf{k})$ if

$(\mathbf{k} - \mathbf{k}')$ equals a reciprocal lattice vector due to all points in the reciprocal lattice, which is a Bravais lattice, being equivalent and thus both vectors being a vector of the reciprocal lattice.

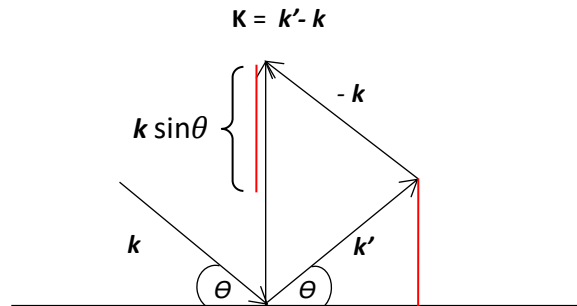


Fig. 2.5: A representation of how diffraction associated with the change in wave vector \mathbf{K} is equivalent to Bragg diffraction from a perpendicular plane [53].

2.1.2.3: Equivalence of the Two Formulations

The Bragg and Laue conditions for X-ray diffraction are in fact equivalent. An equivalence which comes from the relation between families of lattice planes and reciprocal lattice vectors described earlier. Considering this relation their equivalence can be shown as follows: due to the incident and scattered rays, \mathbf{k} and \mathbf{k}' , having equal wavelengths the magnitudes of \mathbf{k} and \mathbf{k}' must also be equal and as such form the same angle with the plane perpendicular to \mathbf{K} , also shown in Fig. 2.5. The scattering from this plane, known as a Bragg plane, is equivalent to a Bragg reflection with the same θ and it can be shown that this reflection satisfies the Bragg condition by firstly considering that \mathbf{K} must be an integer multiple of the shortest reciprocal lattice vector, $\mathbf{K}_0 = 2\pi/d$, leading to Eq. 2.16:

$$\mathbf{K} = \frac{2\pi n}{d} \quad (2.16)$$

As seen in Fig. 2.5 the value of \mathbf{K} must also be equal to $\mathbf{K} = 2\mathbf{k} \sin\theta$; which, when substituted into Eq. 2.16, along with the expression for k of $2\pi/\lambda$ yields the Bragg condition, Eq. 2.10 [53].

2.1.2.4: X-ray Powder Diffraction

The theory of X-ray diffraction shows that only certain planes will diffract X-rays of a certain wavelength if the angle of incidence satisfies the Bragg condition. However, in an approach called X-ray powder diffraction (XRD), also known as the Debye-Scherrer method, this condition can be satisfied without the need to reorient the sample or change the wavelength. As the name suggests this method achieves this using a powdered sample which ensures that, on average, there is always a crystal plane at the correct orientation to produce diffraction. Another result of the individual crystallites being randomly orientated is that diffraction occurs in all directions producing cones of scattered radiation which correspond to a given 2θ , as shown in Fig. 2.6.

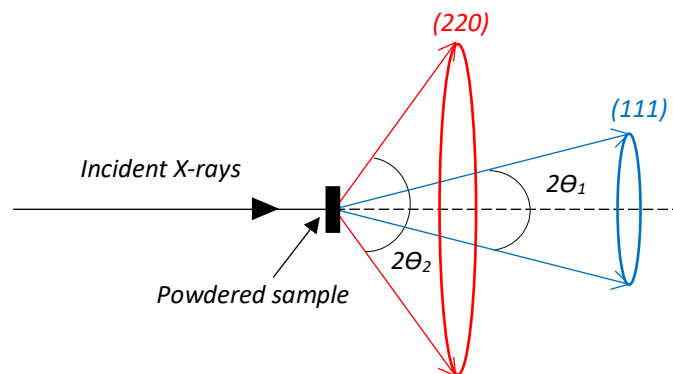


Fig. 2.6: A diagram showing the cones of diffraction produced in powder diffraction, corresponding to a given 2θ . The cones have also been indexed with example values of hkl ; although these are not to scale, they follow the correct trend. [56]

2.1.2.5: Crystal Structure Refinement from a Powder Diffraction Pattern

Recording the intensities of Bragg peaks for a range of 2θ produces a set of data known as a diffraction pattern. These patterns which relate intensity to the angle of observance and therefore d spacing are determined by the crystal structure of the material being studied. The peak position within the diffraction pattern is determined by the unit cell and the intensities of these peaks are determined by the position of all the atoms within the unit cell. Consequently, if a good starting model is available, precise structural information can be obtained from powder diffraction data by

structure refinement methods. Structural refinement is an iterative process, in which a good starting model of the structure is refined to the best matching structure by calculating the corresponding diffraction pattern for the model and comparing this with the observed pattern. The most popular variation of this method is the Rietveld method, which is discussed in section 2.1.4. It is worth mentioning that the term ‘*best matching*’ has been used because many materials have not been completely solved, usually as a result of the difficulty of determining the positions of the atoms from the intensities [56].

Peak positions relation to the unit cell can be understood by considering the different ways in which a crystal comprised of many atoms can be separated into planes of atoms, Fig. 2.1. Each family of planes has a certain hkl and each set of equivalent families of lattice planes have a different value of d , which corresponds to a different value of θ . Take for instance a cubic crystal, where the $\{100\}$ planes are all equivalent with the same value of d and therefore produce Bragg peaks at the same 2θ . Through combining the formulas for d -spacing Eq. 2.7 and Braggs law Eq. 2.10 an equation which describes the relation between a given plane and the Bragg angle, θ , which produces it can be formed [56]:

$$\frac{\sin^2 \theta}{(h^2 + k^2 + l^2)} = \frac{\lambda^2}{4a^2} \quad (2.17)$$

Here Eq. 2.17 gives the relation between the hkl and θ for a cubic crystal; non-cubic crystals have similar relations, which allow for the determination of the lattice planes giving rise to certain peaks. Since the largest d -spacing, corresponding to the largest lattice constant in the unit cell, is given by the smallest value of 2θ it is easy to obtain. For the case of a cubic cell this is a , which has the same value for all lattice constants. As the right-hand side of Eq. 2.17, relating θ to its corresponding plane, is a constant for a given wavelength and spacing. The problem of finding which plane gives which peaks, known as indexing, is reduced to a case of finding the sets of integers, $(h^2 + k^2 + l^2)$, that produce a constant quotient when the corresponding values of θ are substituted into the numerator. Again, lattice constants for other unit cells can be calculated in the same way using the equivalent equations that relate θ and λ .

Similarly, among other factors such as thermal parameters and preferred orientation, the peak intensity corresponding to atom position is a result of the phase differences arising from atoms having different positions within the unit cell. X-rays scattered from different atom positions will have slightly different phases and thus the amplitudes of each scattered X-ray will sum differently. The resultant wave from the summation of all the scattered waves, from one unit cell, can be described by the structure factor, F_{hkl} :

$$F_{hkl} = \sum_1^N f_n e^{2\pi i(hu_n + kv_n + lw_n)} \quad (2.18)$$

Here N is the number of atoms within the unit cell; u_n , v_n and w_n are fractional coordinates and f_n is the atomic scattering factor. The atomic scattering factor is analogous to the structure factor in that it describes how X-rays scattered from different electrons within an atom combine. Note that the atomic scattering factor is related to the number of electrons in an atom and as such different atoms scatter X-rays differently making the problem more complex for heteroatomic molecules, comprised of atoms with different atomic numbers. Finally, the intensity of a scattered X-ray beam is proportional to its amplitude squared i.e. $|F_{hkl}|^2$, which is calculated by multiplying F_{hkl} by its complex conjugate and shows the relationship between atom position and intensity.

Due to the different positions of electrons within an atom's diffuse electron cloud the slight phase difference between rays diffracted from different positions produces partial destructive interference. This interference causes a decrease in intensity of scattered rays with increasing 2θ . Further still, the wavelength of the incident X-rays can increase this effect due to the difference in phase causing a larger amount of cancellation for waves of smaller wavelength. These effects result in the X-ray scattering cross section being proportional to $\frac{\sin\theta}{\lambda}$ [55].

2.1.3: Neutron Diffraction

From a quantum mechanical perspective, due to wave particle duality, a beam of neutrons can be regarded as a beam of radiation analogous to X-rays. This beam has a frequency, $f = \frac{E}{h}$, and a wave vector, $k = \frac{P}{h}$, where E and P are energy and

momentum, respectively. Therefore, all of the diffraction theory discussed above applies to neutrons as well, meaning that neutrons can be used to probe the crystal structure of materials in exactly the same way as X-rays. There are however, several differences between neutron and X-ray diffraction.

The first difference is that, unlike X-rays, neutrons are diffracted by the nucleus of an atom and not the electrons. As a result, the atomic form factor (for X-rays) must be replaced by the scattering length, b , which comes from the quantum mechanical treatment of a neutron interacting with the spatial wave function of the nucleus. Therefore, the scattering amplitude depends on the scattering potential which describes the interaction between a neutron and the nucleus as given by the Fermi pseudo-potential, $V(r)$, a scalar field which is zero unless very close to the nucleus [57].

$$V(r) = \frac{2\pi\hbar^2}{m_n} b \delta^3(r) \quad (2.19)$$

Here m_n represents the mass of a neutron and $\delta(r)$ represents the Dirac delta function.

With this alteration the structure factor for the scattering of a neutron from the unit cell is given by:

$$F_{hkl} = \sum_1^N b_n e^{2\pi i(hu_n + kv_n + lw_n)} \quad (2.20)$$

Where b_n represents the coherence length of the n^{th} atomic nuclei in the unit cell.

The coherence length differs for different atoms and even isotopes of the same atom. However, there is no dependence on atomic number, Z , and strong scattering can still be obtained from low Z atoms, such as oxygen. In addition to this the intensity of the diffracted rays does not decrease with scattering angle, resulting in well-defined diffraction peaks at large 2θ . Another advantage of using neutrons for diffraction is that they have larger penetration making them good for probing bulk samples [58]. Larger penetration also allows for complex sample environments, such as placing a sample within a furnace or cryomagnet to vary the temperature and apply field. Neutron diffraction data is particularly good for structural refinement using the Rietveld method due to all atoms producing significant scattering and the constituents

already being known from the assumed starting structure. It is also worth noting that some atomic nuclei hardly scatter neutrons at all, such as vanadium, making it an ideal container material [55].

2.1.3.1: Magnetic Scattering of Neutrons

Another difference between X-rays and neutrons is that neutrons carry spin and therefore interact with the magnetic moments of unpaired electrons within an atom. When there is long range magnetic order, neutrons are coherently scattered and can be used to determine the magnetic structure of a material in the same way as the atomic structure. In contrast to the atomic structure a form factor known as the magnetic form factor must be used to determine the magnetic structure. This is due to the magnetic scattering being caused by electrons and comes from similar considerations to those discussed in section 2.1.2.5. Similarly, this also causes the magnetic scattering cross section to decrease with $\frac{\sin\theta}{\lambda}$ [59].

2.1.3.2: Neutron Powder Diffraction

Neutron powder diffraction (NPD) gives similar benefits to XRD regarding meeting the Bragg condition. However, the difference in form factors often means that site occupancies and atomic displacement parameters are more accurately determined from NPD data, as well as NPD having greater sensitivity to lighter atoms. This said, NPD also has limitations regarding the determination of magnetic order due to the overlap of symmetric reflections. For instance, in a system with a tetragonal unit cell, atoms with moments in the (100) direction will produce a powder diffraction pattern which is identical to that produced if the moments were in the (110) direction. More precisely, any rotation of the spin arrangement in the *a-b* plane in a tetragonal system will not affect the magnetic intensities of the diffraction pattern [59].

2.1.3.3: Time-of-Flight Neutron Diffraction

One method of neutron diffraction commonly used is time-of-flight neutron diffraction, see Fig. 2.7 for a schematic of the design of a time-of-flight diffractometer. In this method a pulsed polychromatic beam of neutrons is used [60]. As the polychromatic beam provides a large number of different wavelength neutrons it is

possible to use wavelength as the variable that is changed in Bragg's scattering equation, Eq. 2.10. So by keeping the scattering angle constant it is possible to probe lattice planes of different d spacing by using different values of λ . Usually this is done by measuring the time taken for a pulse of neutrons to reach the detector, its time-of-flight, and combining this with the knowledge of the separations between the origin of the pulse of neutrons, the sample and the detector. These quantities can be used to calculate the neutrons velocity and consequently its momentum which in turn can be used to calculate the wavelength of the diffracted neutrons using the de Broglie relation, $\lambda = \frac{h}{p}$, hence making it possible to determine the wavelengths responsible for each Bragg reflection. Pulses, or short bursts, of neutrons are usually produced using a chopper consisting of one or more rotating disks with slits that only allow neutrons through when the apertures align with the beam, Fig. 2.7.

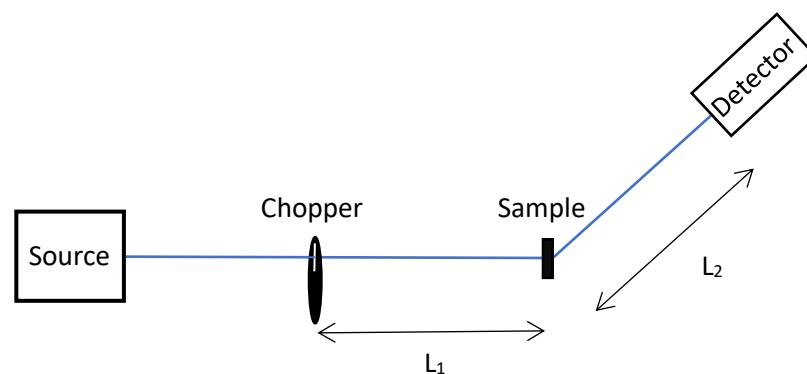


Fig. 2.7: Schematic of a Time of flight diffractometer. The source in the figure is a polychromatic neutron source. The distances represented by L_1 and L_2 are the distances used, along with the time-of-flight from the chopper to the detector to determine neutron velocity and thus wavelength.

2.1.4: Data Analysis, the Rietveld Method

As mentioned earlier powder diffraction patterns are made up of many peaks coming from Bragg reflections. In some cases the diffraction peaks seen are made up of several individual Bragg peaks that overlap. As a result, some methods for structural refinement, such as integrating intensities over a small group of overlapping peaks, leads to a loss of information. In order to overcome this and obtain the maximum amount of information possible a refinement method which is based on profile intensities was developed by H. M. Rietveld, known as the Rietveld method [61].

The Rietveld method can be used for both XRD and NPD data and is capable of refining both the nuclear and magnetic structures seen in the latter. This along with the amount of information extracted from the powder profile makes this method extremely valuable and the preferred method for refining structural information from a powdered sample. As previously stated, this method is an iterative one which takes an initial structural model and gradually refines this to the correct, or best matching, model using least squares refinement; a process which sees the model incrementally altered to provide the smallest difference between the calculated and observed profiles as possible.

To calculate the predicted profile intensity arising from the model being refined all contributions from each individual Bragg peak to the measured profile, y_i , for each 2θ are summed resulting in Eq. 2.21 shown below[10].

$$y_i = \sum_k \left(t j_k L_k \frac{2\sqrt{\ln 2}}{H_k \sqrt{\pi}} e^{\left[-\frac{4\ln 2}{H_k^2} (2\theta_i - 2\theta_k)^2 \right]} \times \left\{ 1 - P(2\theta_i - 2\theta_k)^2 \cdot \frac{s}{\tan \theta} \right\} \right) S_k^2 \quad (2.21)$$

Where:

t = The step width of the counter.

j_k = The multiplicity of the reflexion.

L_k = The Lorentz factor, which accounts for two different geometrical effects [62].

H_k = The full width at half maximum.

P = The asymmetry parameter.

$2\theta_k$ = The calculated position of the Bragg peak corrected for the zero-point shift of the counter.

s = -1, 0 or +1 depending on whether the sign of $2\theta_i - 2\theta_k$ is negative, zero or positive, respectively.

$S_k^2 = F_k^2 + J_k^2$, the structure factor containing both the nuclear and magnetic contributions respectively.

Once the profile intensities have been calculated the least squares refinement can begin. This is a process which aims to minimise the residual function, M , shown in Eq. 2.22 [61],

$$M = \sum_i w_i \left[y_{i,obs} - \frac{1}{c} y_{i,cal} \right]^2 \quad (2.22)$$

by altering the specified parameters a little each cycle until convergence is reached. Within the function M ; $y_{i,obs}$ represents the observed profile intensity, $y_{i,cal}$ the calculated intensity, c is a scaling constant and w_i represents the mathematical expression within the brackets, appearing before the structure factor, in Eq. 2.21, and gives the contribution made by a Bragg peak at $2\theta_k$ to the profile at $2\theta_j$.

To determine when a refinement is complete and whether the model used matches the actual crystal structure producing the diffraction pattern, a set of mathematical quantities known as residual factors or R-factors are used.

R_p shown in Eq. 2.23 [63] is known as the residual factor and describes the difference between the observed and calculated data points.

$$R_p = \frac{\sum |y_{i,obs} - y_{i,cal}|}{\sum y_{i,obs}} \quad (2.23)$$

R_{wp} denotes the weighted profile R-factor, Eq.1.24 [13]:

$$R_{wp} = \sqrt{\frac{\sum_i w_i (y_{i,obs} - y_{i,cal})^2}{\sum_i w_i (y_{i,obs})^2}} \quad (2.24)$$

The latter R-factor is so named because it features the square root of the minimised quantity, Eq. 2.22, normalised by the weighted intensities [64]. Note that in these expressions the scaling factor has been omitted as it can equally be put into the expression for $y_{i,cal}$.

While the R-factors described above compare the calculated and observed data they do not give any information regarding the quality of the data. On the other hand, the expected R-factor, R_{exp}

$$R_{exp} = \sqrt{\frac{N - P + C}{\sum_i w_i (y_{i,obs})^2}} \quad (2.25)$$

evaluates the quality of the data and represents the best fit that can be expected [63]. Within the expression for R_{exp} ; N is the total number of observations, P is the number of parameters refined and C is the number of constraints used.

Comparing this with the R_{wp} leads to another commonly used agreement factor, the Goodness-of-fit parameter, $GOF = \sqrt{\chi^2}$:

$$\chi^2 = \left(\frac{R_{wp}}{R_{exp}} \right)^2 \quad (2.26)$$

From the definition of the GOF, Eq. 2.26 [63], it follows that a value of $GOF = 1$ suggests that the optimal fit has been reached. Hence, the closer to a value of one which is achieved the better the fit. Equally this suggests that the GOF cannot be less than one as this would suggest a fit which is better than can be expected has been achieved. This means that something within the refinement must be incorrect, such as more refinement parameters being used than can realistically be fit to the data or incorrect estimated standard deviations (e.s.ds) in the data points.

2.1.5: X-ray Powder Diffraction Experimental Method

X-ray diffraction measurements were performed using a Panalytical Empyrean X-ray diffractometer, using monochromated $\text{Cu K}\alpha_1$ radiation ($\lambda = 1.5406 \text{ \AA}$) operating at 40 kV and 40 mA. The sample was adhered to a zero background silicon sample holder with a thin layer of Vaseline and a twenty hour scan was taken, measuring 2θ scattering angles between 10 and 90°.

2.1.6: Neutron Powder Diffraction Experimental Method

NPD data was collected at the ISIS Neutron and Muon Source using the WISH diffractometer. The sample was pressed into pucks and stacked within a vanadium can mounted inside the 10 T cryomagnet. The data were collected over a range of temperatures and applied magnetic fields from 1 to 150 K in fields of 0.1, 0.5, 3 and 7 T, respectively. All data were collected using the same sample in sequential runs. Each run was cooled with no applied field to 1 K, then a field was applied and measurements taken as the temperature of the sample was incrementally increased to a maximum of 150 K. The same procedure was followed for each of the fields studied starting with two zero field measurements and then increasing the field for each successive run. Note that the sample was not heated to $T > T_N$ between measurements so, other than the initial run, true ZFC data were not collected.

Likewise, after the zero field cooled (ZFC) 0.1 T measurement was taken, field cooled (FC) measurements in a 0.1 T field were also made between 1 and 80 K to investigate whether field cooling affected the material. Similarly, after all the field measurements had been collected a final set of zero field measurements were taken, this time upon cooling from 150 to 50 K.

The WISH diffractometer is a time-of-flight diffractometer, as described in section 1.3.3, that uses a pulsed neutron beam provided from a spallation source [65]. Neutrons from a spallation source are produced by accelerating protons, using a synchrotron in this case, at a target such as tungsten. When the highly energetic protons interact with the nuclei they disintegrate producing, among other particles, neutrons which can then be extracted, moderated and used in experiment [66]. The WISH detector itself is comprised of 10 banks of detectors covering a scattering angle range of 320°.

2.1.7: Rietveld Analysis Using XRD Data

Rietveld analysis of the diffraction data was performed using the GSAS suite of software to extract information on the crystal and magnetic structures [67, 68]. Refinement using the XRD data was based on the model previously reported by Hiley *et al.* [41], consisting of a hexagonal unit cell ($a = 5.20573 \text{ \AA}$, $b = a$, $c = 5.23453 \text{ \AA}$) and $P\bar{3}1m$ space group. The fractional atom positions (x, y, z) for each atom were as follows; Sr = (0,0,0), Ru = (0.33333, 0.66667, 0.5) and O = (0.37873, 0, 0.2980) [41]. The refinement then followed these basic steps: first the scale factor and background were fitted. The background was fitted using a Shifted Chebyshev function with 12 terms. Following this the background coefficients were held constant while the lattice parameters were refined. After this the Zero point was refined followed by the atom positions. Now it was possible to refine the peak shape by refining the GV, GW and LY, Gaussian and Lorentzian terms. Spherical harmonic terms were added to account for preferred orientation effects arising as a result of the plate like morphology exhibited by the material [61, 69]. Finally, the background was turned back on and all parameters refined once more. Note as more refinement parameters were turned on all previous parameters were still being refined as well, unless otherwise stated such as for the background coefficients. In addition to these common steps the atomic

displacement parameters, U_{iso} s, were fixed at 0.01 \AA^2 as U_{iso} s cannot be determined reliably from XRD data, due to the decreasing form factors with increasing 2θ and potentially too much correlation between background and displacement parameters [70]. In the end the refinement consisted of 32 variables.

2.1.8: Rietveld Analysis Using NPD Data

Rietveld refinement of the NPD data collected on banks 5 and 6 of WISH began by first fitting the peaks that came from nuclear scattering to determine the crystal structure. This was done by following the same basic steps described in the refinement of the XRD data only with a few alterations required for the use of neutrons and not X-rays. For example different peak shape terms, the sigma and gamma terms sig-1, sig-2 and gam-1, were used and refined. Additionally, the zero point was not refined since this data was collected in time-of-flight. Similarly, the same initial model reported by Hiley *et al.* [41] was used and spherical harmonics added to account for the preferred orientation that would come from compressing the powder into a puck [61, 69]. Once this model had been refined to its optimal agreement with the observed data it was clear that something was missing as there were several peaks still unaccounted for and the goodness-of-fit parameters had large values of $\chi^2 = 36.69$, $R_p = 9.2 \%$ and $wR_p = 11.7 \%$. These unaccounted peaks were expected to come from scattering associated with the magnetic phase. To determine the magnetic phase the refinement needed to include a model magnetic structure which accounted for these peaks.

2.1.8.1: Refinement of the Magnetic Structure

Although one magnetic peak was observed at slightly larger d spacing in bank 2 it was accounted for by the model used for banks 5 and 6, so only the data from banks 5 and 6 were used for refinement.

To fit the peaks corresponding to magnetic scattering, which will be referred to as magnetic peaks, a two-phase fit without magnetic symmetry analogous to the one described by J. Cui, Q. Huang and B. H. Toby in reference [59] was used.

Having first refined the crystal structure of SrRu₂O₆ using a nuclear only³ phase, Phase 1, a second magnetic only phase, Phase 2, was added to the GSAS experimental file. This phase was given *P*1 symmetry to allow the manual input of atom locations and symmetry constraints. The unit cell used was the same as that determined from the refinement of the crystal structure in Phase 1 only doubled along the *c*-axis as reported by Hiley *et al.* [41] i.e. it was also hexagonal and had lattice parameters of $a_{p2} = a_{p1}$, $b_{p2} = b_{p1}$, $c_{p2} = 2c_{p1}$. Having defined this unit cell the atom location for each atom had to be input so that atoms in this phase, which would give the magnetic scattering, corresponded to the same location as the corresponding atoms which modelled the nuclear scattering (Phase 1). This second phase only required the Ru atoms to be input as they are the only atoms with a magnetic moment that would give rise to magnetic scattering. Similar to the atomic positions, the U_{iso} 's of the Ru ions were set to the same value as in Phase 1. Lastly in the scaling controls the phase fraction of the magnetic phase (Phase 2) was set to half that of Phase 1, 0.5 and 1 respectively. This was required to ensure an equal phase volume for each was present. These values were then fixed while the overall scale factor was refined.

Now that the phases had been specified constraints had to be added so that all the parameters for corresponding atoms in each phase would change together. To maintain the same U_{iso} s for both phases as well as keep the unit cells of the two phases to remain hexagonal and for the parameters to change at the same rate constraints were used. The *a* and *b* lattice constants were constrained to change at the same rate while the *c* lattice constant of Phase 2 was constrained to change at twice the rate of Phase 1, to account for the magnetic unit cell being doubled along the *c*-axis.

Constraints did not need adding for the atom positions of the Ru atoms in Phase 2 due to the atom positions of the Ru in Phase 1, (1/3, 2/3, 1/2) being a special position in the $P\bar{3}1m$ space group [71]. Consequently, the Ru atom position would not be altered during refinement. Profile constraints were also applied to constrain the profile peak shape of the two phases, 1 and 2, to remain equal whilst refined. Doing so reduces the number of variables being refined and along with it the chances of correlations and

³ Nuclear and Magnetic only phases are GSAS phase editing flags that make the software aware that it should be processing nuclear or magnetic scattering information.

divergence. After defining and constraining the atoms in Phase 2 it was required to input the magnetic information. An initial model based on the magnetic structure described by Hiley *et al.* was used [41]. The moment for each atom had to be specified with the spin up moments, assigned to atoms Ru2 and Ru3, having a value of $1.4 \mu_B$ and the spin down moments, assigned to Ru1 and Ru4, having a value of $-1.4 \mu_B$. Ru⁵⁺ has a different electron distribution to non-oxidised Ru, the atom being used in the model, and consequently the magnetic form factors will be different i.e. the magnetic form factor is dependent on the atom valence [59, 64]. There is no magnetic form factor recorded for Ru⁵⁺ in the international tables for crystallography. However, from a review of the literature a value for the form factor, the origin of which will be discussed later, was found to have $\langle j_0 \rangle$ magnetic form factor coefficients of $A(A1) = 0.441$, $a(B1) = 21.046$, $B(A2) = 1.4775$, $b(B2) = 6.0360$, $C(A3) = 20.9361$, $c(B3) = 4.2473$ and $D(C) = 0.0176$ [72]. Here the brackets represent the names that GSAS uses to denote each term; note that the A4 and B4 coefficients were set to 0.0 and the $\langle j_2 \rangle$ coefficients were unchanged from the values of the Ru form factor, for reasons explained later. Finally, the magnetic moments needed constraining in analogy with the other parameters. Due to the magnetic moment being reported to be along the *c*-axis, the *x* and *y* components, *MX* and *MY*, of the moment were constrained to be zero while the *z* components of the spin up and spin down moments were constrained to change in magnitude at the same rate, using a multiplier of 1 and -1, respectively.

With the magnetic model complete it can be seen that like spin Ru atoms are separated by an inversion centre and thus the magnetic phase can be described using $P\bar{1}$ symmetry. Doing this halved the number of magnetic atoms needing to be input and constrained, *etc.* in subsequent refinements.

2.1.8.2: Origin of the Magnetic Form Factor for Ru⁵⁺

To accurately determine the magnetic form factor knowledge of the coefficients in Eq. 2.27 [72] is required, as $\langle j_0 \rangle$ represents the main contribution to the form factor for transition metals.

$$\langle j_0 \rangle = Ae^{-as^2} + Be^{-bs^2} + Ce^{-cs^2} + D \quad (2.27)$$

A study by Parkinson *et al.* [72], from which the form factor for Ru^{5+} was taken, made comparisons of known magnetic form factors of isoelectronic species. From this they were able to conclude that the magnetic form factor of a species could be obtained from a neighbouring species, i.e. the next ionic state, by using a common scaling factor in the exponents of Eq. 2.2. Doing this they estimated the form factor for Ru^{5+} using Ru^+ and a scale factor of 0.63184, leading to the values stated earlier. No other work, single crystal or otherwise, was found to offer a better estimate of the form factor and hence this value was used. The paper did not mention the $\langle j_2 \rangle$ terms, further to this a tutorial refinement on $\text{YBa}_2\text{Fe}_3\text{O}_8$ [73] specifies that the values for the $\langle j_0 \rangle$ coefficients should be checked and changed while the $\langle j_2 \rangle$ coefficients are left unchanged. Therefore, it was assumed that the same assumption, to leave the $\langle j_2 \rangle$ coefficients unchanged could be made. Similarly, the tutorial states that the A4 and B4 terms in GSAS are not used in international tables and should be given values of zero, hence these values were set to zero in the refinements of the data discussed.

2.1.9: Errors Associated with GSAS

For results determined from refinement, including lattice parameters, bond angle *etc.*, GSAS provides errors associated with each quantity. These are the errors reported within this work unless otherwise stated. The uncertainty in the moment was $\sim 1.3 \times 10^{-2} \mu_B$, this being the modal value, however, some refinements reported larger values with some as large as $1.8 \times 10^{-2} \mu_B$, while others reported no value at all. i.e. n/a and not an error of zero. Hence to estimate an error for all sets of data, those with values and those without, a maximum confidence uncertainty value of $1.8 \times 10^{-2} \mu_B$ was assumed. Moreover, the paper from which the magnetic form factor was taken carried out an investigation which found that imprecise knowledge of the form factor creates an error $\sim 5.0 \times 10^{-2} \mu_B$ [72]. This error is somewhat larger than that given by GSAS, however, still being to the second decimal place it would suggest that the magnetic moment can be calculated to the first decimal place with a good degree of certainty. For the most part during the results section only the errors from GSAS are presented and taken into consideration, unless otherwise stated, as the estimated form factor should provide a more precise value compared to that of the real value than for the values used in determining the uncertainty within the study [72].

2.1.10: The Le Bail Method

Another Full pattern method, known as a whole-powder pattern decomposition, which can be used to refine crystallographic models is the Le Bail method [74]. This pattern decomposition method is slightly different from the Rietveld method using an initial unit cell and space group to determine peak position while the peak intensities are treated as arbitrary unknowns. The unit cell is refined in a similar manner to Rietveld refinement, a least squares fit based on theoretical calculations, while the intensity values are iteratively adjusted to the optimal fit by assigning estimates from distributing data values amongst the contributing peaks [75]. This means that only the unit cell, background function and peak profile parameters can be refined. Usually pattern decomposition methods can be the only way to fit powder patterns from structures which are unknown and is the preferred method for fitting difficult to model experimental artefacts.

2.2: SQUID Magnetometers and Magnetisation Measurements

The magnetisation of a sample and the magnetisation of a sample in a given field, χ , can be measured using a Superconducting Quantum Interference Device (SQUID) magnetometer. How this is done and the physical principles that make it possible are discussed here.

Due to the Meissner effect a ring of superconducting material can trap magnetic flux by applying a flux while in the normal state and then cooling it into the superconducting state. If the applied flux is taken away then a current is induced in the ring which acts to keep the flux within the ring constant, trapping the flux. Due to effectively zero resistance this current can circulate the ring indefinitely and thus the flux remains trapped within the ring while it is in the superconducting state.

Interestingly, the flux can only be trapped in discrete quantities which are a multiple of $2.068 \times 10^{-15} \text{ W}$, one flux quantum ϕ_0 , showing that flux is quantised in units of ϕ_0 [7].

2.2.1: The Josephson Effect

If a superconducting loop contains a normal resistive region such as a section of the loop being replaced by a non-superconducting material⁴ it would be expected that the superconducting current would be destroyed. However, this is not the case as Cooper pairs can tunnel across the resistive region assuming that the coherence length is larger than this region i.e. the wave function of the electrons can penetrate the normal region and is not completely attenuated. This effect was first predicted by Josephson and as such the effect of a superconducting current flowing over a resistive region, called a Josephson junction, is known as the Josephson Effect. For separations between the superconducting regions that are smaller than the coherence length of the superconductor and for currents which do not exceed a critical current I_c which is characteristic of the Josephson junction the current can cross the resistive region with no voltage drop [7].

The Josephson Effect can thus be used to measure variations in flux by coupling flux into a SQUID, a superconducting loop featuring two Josephson junctions, using an inductive input coil. This then causes screening currents to be induced within the loop which will increase or decrease I_c according to the direction of flux. So by applying a bias current, I_b , slightly larger than I_c , results in a voltage drop across the junction; the change in flux coupled into the loop can be measured by measuring the consequent change in voltage, due to the change in I_c caused by the screening currents. This voltage changes in a periodic manner with a periodicity of one flux quantum, ϕ_0 [7].

2.2.2: Design and Operation of a SQUID Magnetometer

A schematic for the design of a SQUID can be seen in Fig. 2.8. Gradiometers are often used as a detection coil as they can discriminate well between magnetic fields from distant noise sources and local sources. Discrimination is achieved because gradiometers feature two or more coils wound in the opposite direction, connected in series and separated by a distance, known as the baseline. For distant sources the flux

⁴ Note that an insulating material can be used although it would have to be very thin in the order of angstroms. Whereas a non-superconducting metal can be much thicker, up to microns.

density is relatively uniform and is detected by both coils equally and thus they cancel each other out. Close sources have far less uniform fields leading to different fluxes being detected at each coil and hence they do not cancel completely [7, 75]. Input coils then convert the current produced by the detected flux into an equivalent amount of flux which can be coupled into the superconducting loop, consisting of two Josephson junctions. In Fig.2.8 shunt resistors are shown connected in parallel with the junctions to stop hysteresis occurring.

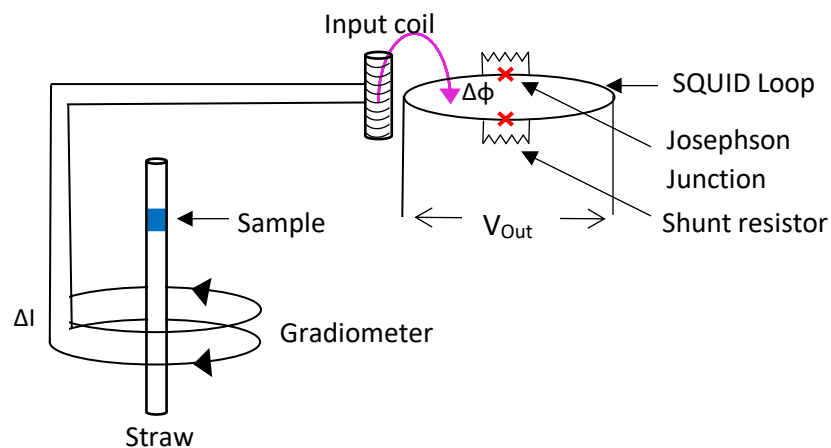


Fig. 2.8: Schematic representation of the basic design of a SQUID magnetometer. Reproduced from [7].

From the theory discussed the basic function of a SQUID can be described as measuring the magnetic flux density of a magnetic sample by moving the sample through a set of detection coils which couple a corresponding amount of flux into the SQUID loop. The change in flux as the sample moves through the coils is then measured by measuring the corresponding voltage drop across the Josephson junctions, produced as a result of Josephson tunnelling, making them essentially flux to voltage transducers [7, 75].

2.2.3: Experimental Method

DC magnetic susceptibility data provided by the supervisory team was previously collected using a Quantum Design Magnetic Property Measurement System MPMS-XL7 and consisted of both field-cooled (FC) and zero-field-cooled (ZFC) measurements. The data were collected over a range of temperatures from 2 to 300 K, in a range of applied magnetic fields from 0.1 to 5 T. In order to mitigate against field effects arising

as a result of not being able to heat the material above T_N between successive runs, each data collection was performed on a new sample loading.

2.3: Scanning Electron Microscopy and Energy dispersive X-ray spectroscopy

To observe the structure of a crystal on the order of angstroms or nanometers a conventional optical microscope cannot be used because the diffraction effects of light cause information at this scale to be corrupted by interference. However, unlike light, when using electrons, diffraction effects only become an issue when resolving to the order of fractions of an angstrom. Hence to obtain high quality images of a crystal at these kinds of length scales electron microscopy must be used [76]. A common form of electron microscopy is Scanning Electron Microscopy, abbreviated to SEM.

2.3.1: Design and Operation of an SEM

The basic design, shown in Fig. 2.9 below, and operation of an SEM is as follows: an electron gun, usually consisting of a tungsten filament, produces energetic electrons. These then pass through a set of electron optics, comprised of magnets and apertures, which provide a beam defined by its current, diameter and divergence. This beam is then scanned across the sample in a stepwise fashion while the levels of the different signals produced by interactions between the electrons and the sample are detected and recorded for each location. The level of these signals which include backscattered electrons (BSE), secondary electrons (SE), absorbed electrons, continuous and characteristic X-rays, can then be used to determine the topology, density *etc.* of the sample [77]. The information from each of the points scanned is then mapped producing an image of the scanned area.

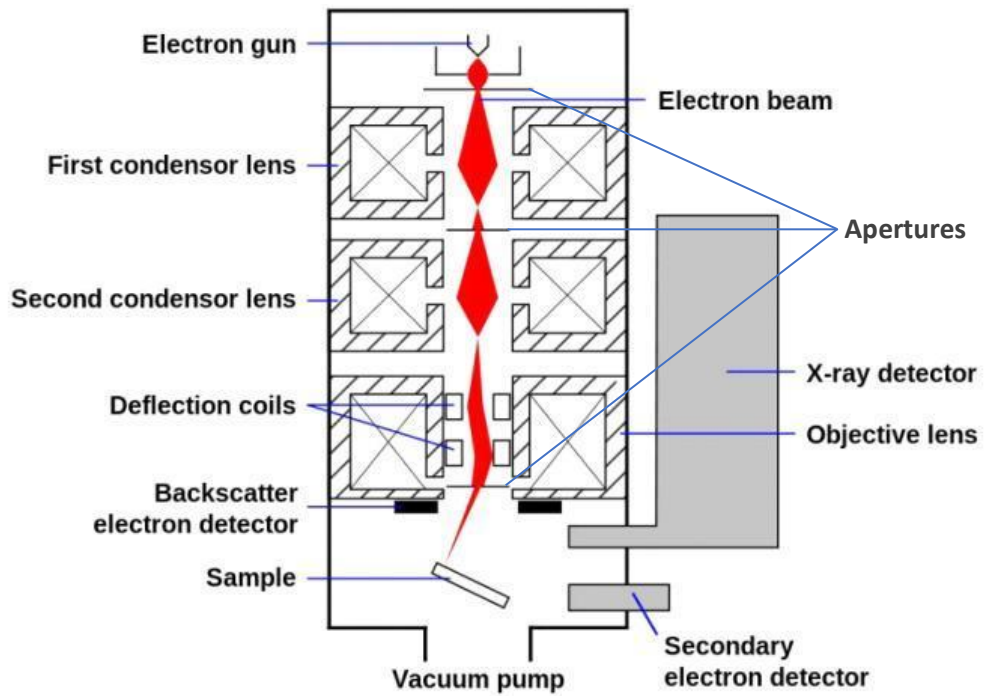


Fig. 2.9: A schematic representation of an SEM. The condenser lenses are made up of magnets represented by the crossed and lined areas. Note the positions of the BSE and SE detectors. Taken and edited from O. P. Choudhary et al. [78].

2.3.2: Electron Beam Interactions

When the electrons are incident on a sample both elastic and inelastic scattering events occur. However, most of the signals measured such as SEs; Auger electrons, X-rays, both characteristic and Bremsstrahlung and longwave length photons up to the infrared region are produced from inelastic events. As well as these a large number of phonons, are also produced.

2.3.2.1: Elastic Scattering Events

In elastic scattering events the direction of the electrons change however, the magnitude of their velocities remain effectively constant and therefore so does the kinetic energies.

This form of scattering comes from collisions with nuclei and so the scattering cross section is described by the Rutherford model, Eq. 2.28⁵ [77]:

$$Q(> \phi_0) = 1.62 \times 10^{-20} \frac{Z^2}{E^2} \cot^2 \frac{\phi_0}{2} \quad (2.28)$$

Here $Q(> \phi_0)$ is the probability of scattering occurring at an angle greater than ϕ_0 ; Z is the atomic number of the scattering atom and E is the electron energy in KeV. This shows that elastic scattering is highly dependent on atomic number and beam energy. While elastic scattering is the source of BSEs it primarily causes electrons to diffuse throughout the sample producing later inelastic events until the energy decreases enough for the electron to be captured.

BSEs are primarily detected by a solid state detector, silicon wafer, mounted directly above the target location of the electron beam. This silicon wafer acts in a similar way to a charge coupled device (CCD). When the BSE hits the silicon wafer a number of electron-hole pairs proportional to the energy of the electron are produced and the resulting current measured. Due to the position of the detector and nature of BSEs, they are good for determining density and atomic number of the sample.

2.3.2.2: Inelastic Scattering Events

During inelastic scattering events the incident electrons lose kinetic energy through interactions with the electrons in the target atom. If the incident electron has a kinetic energy greater than the ionisation energy of the target electron this electron can be ejected from the atom and is known as a secondary electron. When this occurs for an inner shell electron another electron in an outer shell can drop into the inner shell, producing an X-ray photon with a characteristic energy. Although, sometimes the energy from an electron dropping to an inner orbital can be transferred to an outer electron which is in turn ejected from the atom. These electrons, known as Auger electrons, carry a characteristic energy and can be used to determine the atomic composition at the surface in a similar way to characteristic X-rays.

⁵ Q has units of (events/ e^- (atoms/cm²))

For the secondary electrons to be detected the sample environment must be kept under vacuum to allow the lower energy SEs to reach the SE detector. Similarly, the detector used is a somewhat active sensor, not simply waiting for the SEs to interact with it but instead collecting SEs. This is done using an anode to attract the electrons and the resulting current measured. A more popular form of SE detector is the Everhart-Thornley electron detector which consists of a scintillator inside a positively charged Faraday cage. Although these can detect both BSEs and SEs it is placed off to one side meaning that few BSEs will be scattered at a large enough angle to be detected, as shown in Fig. 2.9. For angled surfaces, i.e not normal to the incident beam, the number of SEs produced increases making them good for determining topographic information [77].

2.3.3: Energy Dispersive X-ray Spectroscopy

As the incident electrons are decelerated by interactions with the atoms they produce photons. This leads to a continuous spectrum of X-ray radiation to be produced, known as Bremsstrahlung radiation. This form of X-ray radiation does not carry any useful information, however the characteristic X-rays produced when an SE is ejected are characteristic of the atoms from which they originate and therefore differ between atoms. This means that they can be used to determine the composition of the sample. Energy Dispersive X-ray Spectroscopy (EDS) is the analysis of the X-rays produced by the electron interactions to determine the composition of the sample. To identify characteristic radiation only statistically significant peaks are used, normally defined as peaks that are three times the standard deviation of the background Bremsstrahlung radiation. These peaks are then compared with the location of those expected for certain elements to determine the elemental composition of the sample.

2.3.4: Experimental Method

SEM images were collected on a Hitachi S-3400 SEM with an Oxford Instruments Xmax-80 EDX detector. The powdered sample was mounted on a Carbon stub and placed in the SEM. Once the chamber was evacuated to a high vacuum, several images were collected using an accelerating voltage of 20 kV at a working distance of 10 mm. In addition to this EDS spectra were also collected.

2.4: A Word on Experimental Work

The research project discussed within this thesis primarily focused on the analysis of the NPD and SQUID data provided by the supervisory team. However, the XRD data was collected by the author. The SEM data was collected by Luke Alesbrook, in the presence of the author.

Chapter 3: Results and Discussion

3.1: Determination of Structure and Purity

First to assess the composition, purity and structure of the samples, room temperature powder XRD measurements were performed. Rietveld analysis of the XRD data showed the crystal structure of SrRu_2O_6 to have a hexagonal unit cell, with a space group of $P\bar{3}1m$ and lattice parameters shown in Table 3.1. The fitted XRD data can be seen in Fig. 3.1. Here the fit shows a slight lack of intensity for some of the peaks, which is most likely due to the thermal parameters having not been refined.

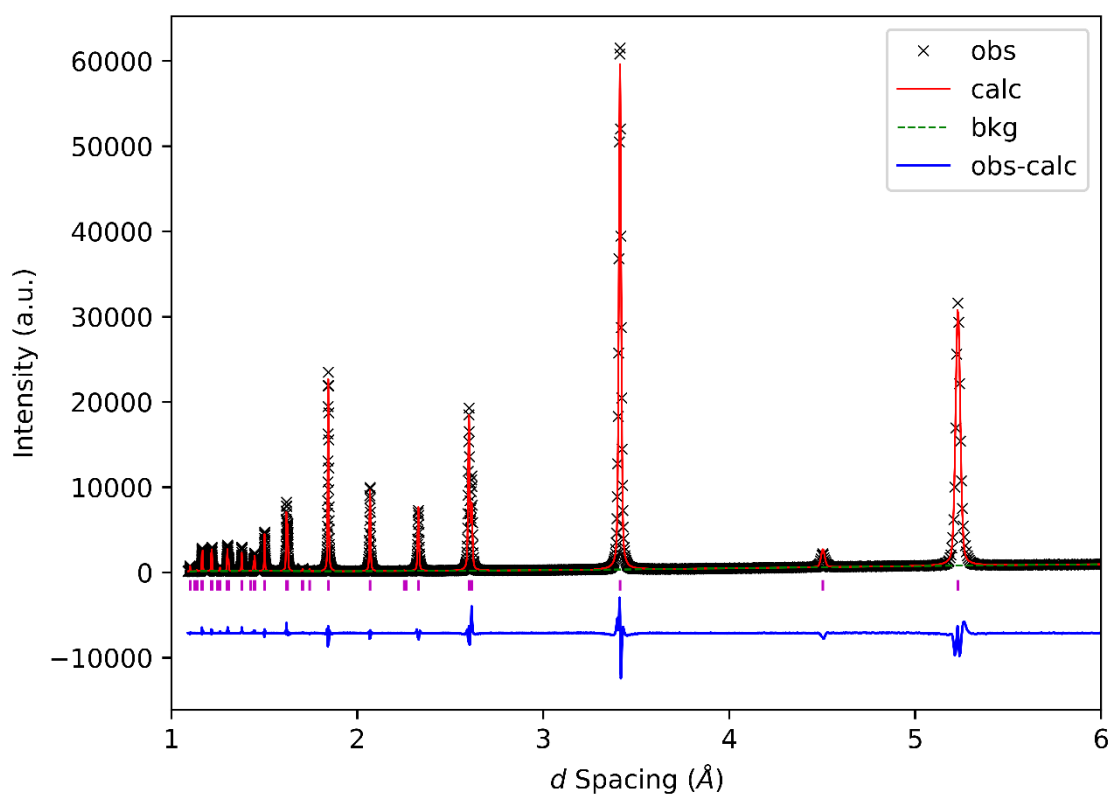


Fig. 3.1: Rietveld refinement of XRD data collected at room temperature, ≈ 293 K, in zero field. Calc = Calculated points; Obs = Observed points, Bkg = Background. The magenta tick marks show the expected positions of Bragg peaks from the model being used within the refinement. The blue curve indicates the difference between the observed and calculated model.

These results are in good agreement with those stated in the literature [41] and correspond to a structure comprised of layers of edge sharing RuO₆ octahedra, separated by layers of interstitial Sr²⁺ ions as shown in Fig. 3.2.

Table 3.1: Rietveld refinement parameters for XRD data collected at ≈ 293 K, corresponding to the refinement shown in Fig. 3.1. The brackets signify atom position within the unit cell, e.g. (1/3, y, z). Where an axis co-ordinate, e.g. x, has been replaced by a value, the value corresponds to the atoms position along that axis.

Refined Parameter	Value	
R_p (%)	7.92	
wR_p (%)	10.40	
χ^2	8.008	
a and b (Å)	5.20090(4)	
c (Å)	5.23039(5)	
Cell volume (Å ³)	122.5242(17)	
Sr - $U_{iso}/U_e \times 100$ (Å ²)	1.0	
Ru - $U_{iso}/U_e \times 100$ (Å ²)	1.0	
O - $U_{iso}/U_e \times 100$ (Å ²)	1.0	
Sr (0, 0, 0)	-	
Ru (1/3, 2/3, 1/2)	-	
O (x, 0, z)	x	0.3770(10)
	z	0.2740(8)

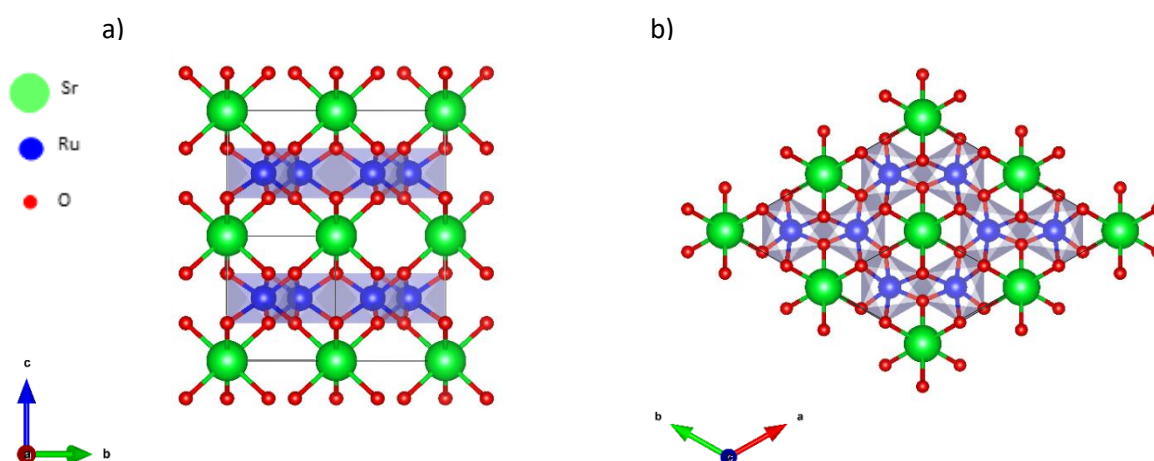


Fig. 3.2: The crystal structure of SrRu₂O₆, produced from .cif files obtained from the Rietveld refinement, viewed parallel to the c-axis and a-b plane in a) and b) respectively. Green represents the Sr, blue the Ru and red the O atoms. The unit cell is represented by the smallest set of enclosed black lines for both a) and b).

Accounting for all of the data with this SrRu_2O_6 model confirms that there are no parasitic substances or phases present in the sample. Similarly, EDS spectra collected from a sample of SrRu_2O_6 , shown in Fig. 3.3, shows the samples to only contain Sr, Ru and O. The carbon peaks seen in the spectra originate from the carbon stub the sample was mounted on.

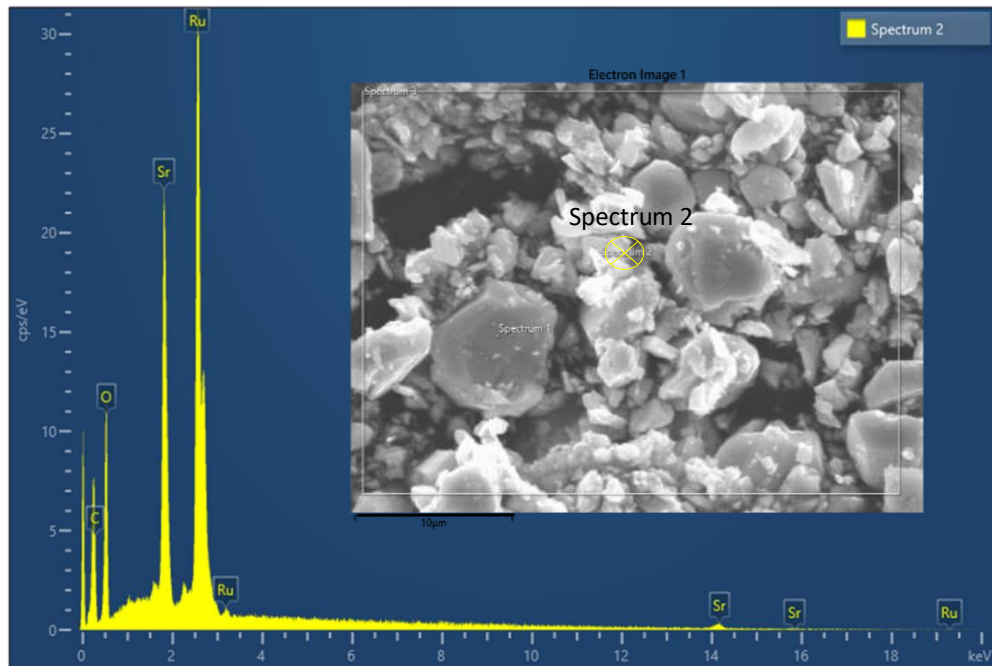


Fig. 3.3 : EDS spectrograph of the SrRu_2O_6 sample. The SEM image insert shows the location from which the spectra was collected. The scale bar, bottom left of the image, represents 10 μm .

3.2: Magnetisation Measurements

The paramagnetic to antiferromagnetic phase transition in SrRu_2O_6 has been reported to occur at 565 K [46]. However, in order to investigate the possibility of a second low temperature magnetic phase transition SQUID magnetometry data were collected at temperatures between 2 and 300 K. The magnetisation measurements collected showed a divergence in χ between field cooled (FC) and zero field cooled (ZFC) data in a low field of 0.1 T below 100 K inconsistent with AFM ordering as shown in Fig. 3.4. This kind of behaviour could be associated with weak ferromagnetic ordering or spin-glass/disordered behaviour [39, 79] possibly arising from magnetic frustration.

Similarly, the loss of divergence seen between the FC and ZFC data in greater field is consistent with glassy behaviour and rules out FM ordering at low temperature. Another reason to suspect spin glass behaviour is due to the covalence between the Ru and O, as reported in the literature [41, 42, 45], leading to the magnetic moments being distributed between sites. In turn, this distribution of the moment can cause frustration and disorder leading to the onset of glassy behaviour, as has been reported for other ruthenate compounds such as SrRuO₃ [22].

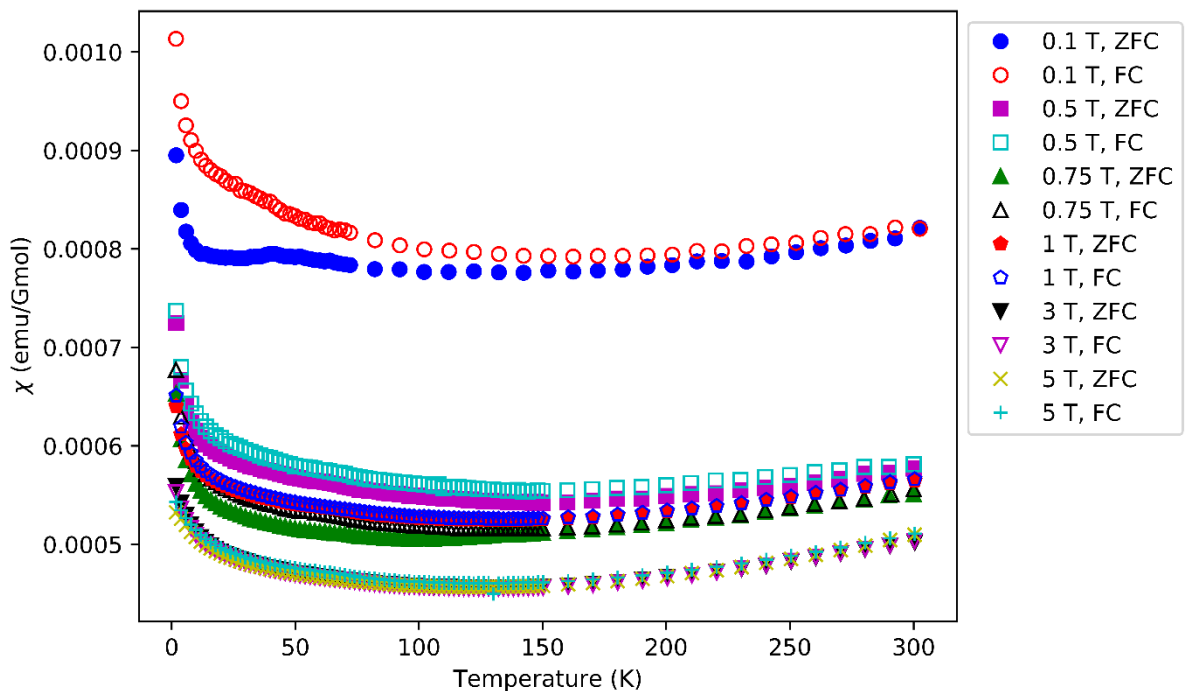


Fig. 3.4: Zero field cooled (ZFC) and field cooled (FC) magnetic susceptibility data collected as a function of temperature for different applied magnetic fields showing the loss of divergence between ZFC and FC data with increasing field strength.

Field dependent SQUID measurements, Fig. 3.5, show that there is no clear hysteresis which is consistent with antiferromagnetic order. This suggests that there is no transition to a ferromagnetic, ferrimagnetic or spin glass ordered state at low temperatures as hysteric behaviour would be expected. The apparent lack of ferromagnetic and spin glass order points towards another form of disorder being responsible for the divergence observed between the ZFC and FC data at low applied magnetic fields.

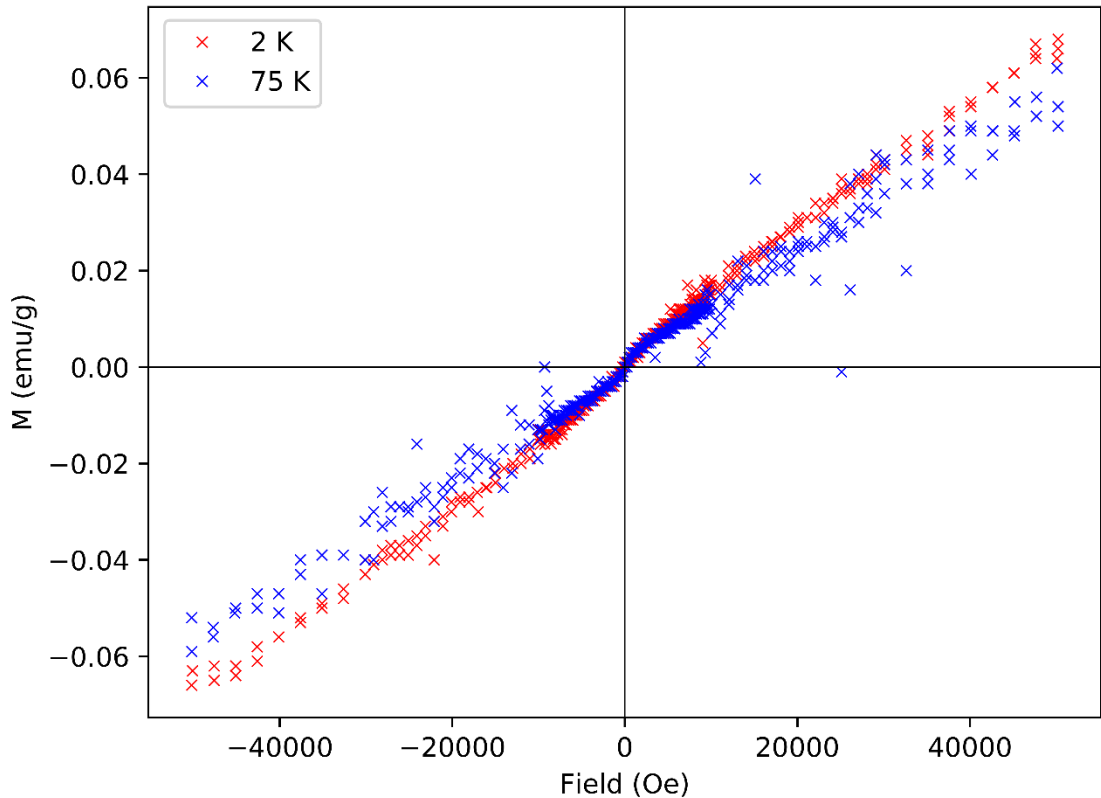


Fig. 3.5: Field dependent Magnetisation measurements of $SrRu_2O_6$ showing no hysteric behaviour consistent with antiferromagnetic order.

3.2.1: Surface-Volume Effects

Previous studies have found that surface-volume effects, arising due to size related effects in nanomaterials, can give rise to uncompensated surface spins which can cause ferromagnetic order to be seen in antiferromagnetic materials or the disorder associated with spin glasses to be observed [6, 80]. Further to this and of more relevance to this work is a study which showed that the morphology of a sample can lead to significant differences in susceptibility measurements [81]. Within this study morphologies with larger surface area to volume ratios, as is the case for nanomaterials, showed greater spin-glass like behaviour [81]. Again, this was attributed to uncompensated surface spins appearing disordered. The concept of uncompensated surface spins refers to spins at the surface which appear to have a different form of order, due to the surrounding spins present in the bulk not being present. For example, an antiferromagnet can seem to be ferromagnetic at the surface if all of the spins at the surface happen to be spin up.

Due to ferromagnetism and spin glass behaviour being ruled out by the results of the hysteresis measurements, the likelihood of uncompensated spins being a possibility was explored. To investigate whether this could be the cause for the divergence between the FC and ZFC magnetisation data SEM images of the SrRu_2O_6 sample were collected as shown in Fig. 3.6.

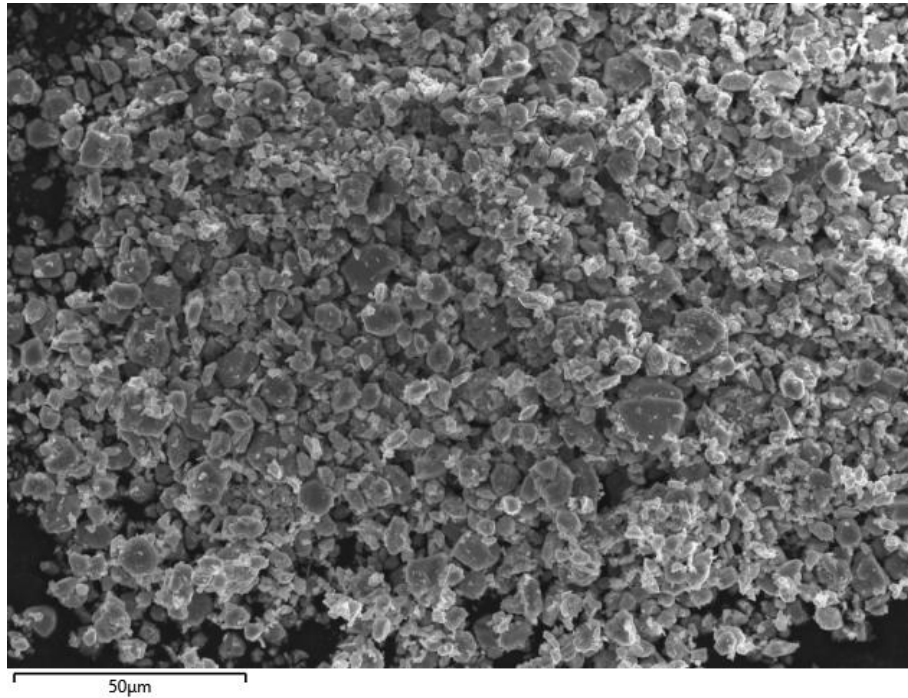


Fig. 3.6 a): SEM image of a powdered sample of SrRu_2O_6 showing its hexagonal plate like morphology. The scale bar represents 50 μm .

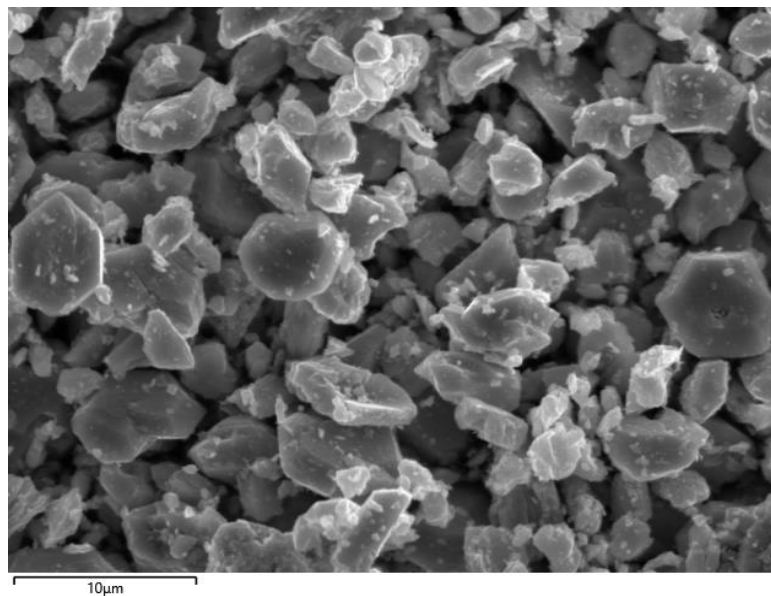


Fig. 3.6 b): SEM image of a powdered sample of SrRu_2O_6 showing its hexagonal plate like morphology. The scale bar represents 10 μm .

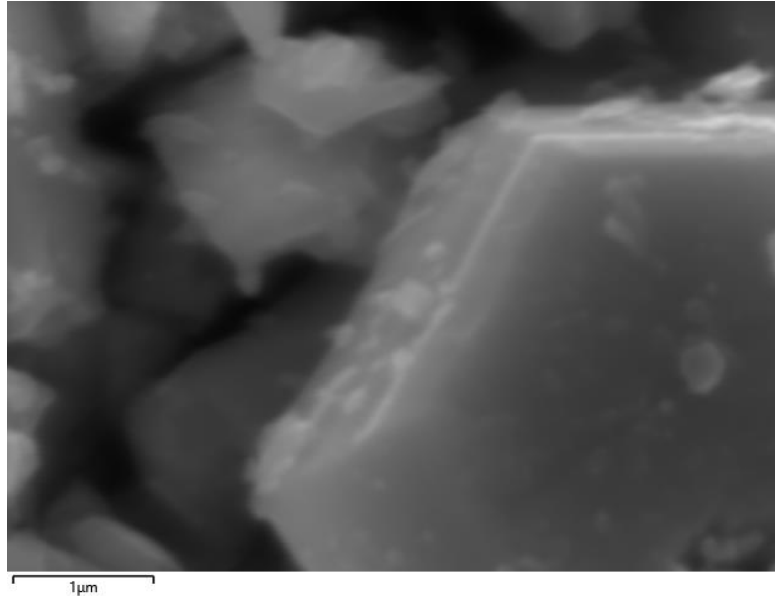


Fig. 3.6 c): SEM image of a powdered sample of SrRu₂O₆ showing its hexagonal plate like morphology. The scales bar represents 1 μm.

From the images in Fig. 3.6 it can be seen that there are a significant number of hexagonal platelets suggesting that SrRu₂O₆ crystallises into hexagonal platelets as reported by Hiley *et al.* [41, 46]. The irregular non-hexagonal shaped crystallites observed most likely arise as a consequence of either grinding of the sample into a powder or incomplete crystal growth. Furthermore, these platelet-like crystallites will have a relatively large surface area to volume ratio and therefore it is likely that there are a significant number of uncompensated spins at the surface. This could lead to an apparent disordering of spins at the surface and result in the divergence seen in the ZFC/FC data collected at low applied fields shown in Fig. 3.4.

3.3: Zero Field Powder Neutron Diffraction Data

To further investigate the structural and magnetic properties of SrRu₂O₆ neutron powder diffraction data in zero field was collected and analysed. Refinement of the neutron powder diffraction data collected at 112 K, in zero applied field, confirmed the crystal structure of SrRu₂O₆ to match the structure determined by XRD, as described in section 3.1 [41]. Furthermore, fitting both the nuclear and magnetic phases to the data collected showed good agreement between the data collected and the refinement models as shown in Fig. 3.7.

However, there were a few peaks that were still unaccounted for within the refinement. The expected magnetic structure fit the diffraction pattern too well for it to be suspected that a slightly different magnetic structure could be the cause of these peaks. However, the constraints on the x and y components of μ were removed in an attempt to see whether a slight alteration or cant in the spins could cause these extra peaks. No stable solution could be found suggesting that this was not the case and so the likelihood of a parasitic phase being present was investigated.

Structures within the sample environment such as vacuum chambers are almost always comprised of aluminium [82]. In addition to this the 10 T magnet used within the study is also known to have aluminium alloy magnet coil supports [83]. Thus, making it very likely that scattering from an aluminium component may contribute to the Bragg peaks observed. Subsequently a model for aluminium (cubic, $Fm\bar{3}m$, $a = b = c = 4.0475 \text{ \AA}$) [84] was added to the refinement as a third phase. Refinement of this model to the values seen in the tables of full refinement parameters in Appendix 1, saw aluminium fit to the data well with lattice constants only changing by approximately 0.25%. It was shown to make contributions to several of the most prominent peaks of the main phase as well as to account for the last few peaks that remained unfit, producing a complete and accurate refinement of the diffraction data as shown in Fig. 3.8.

The aluminium phase followed a similar refinement procedure to that of the nuclear phase (described in Chapter 2) with spherical harmonics being added to account for the preferred orientation associated with a machined material [85]. To account for the uncertainty in how much aluminium was actually present in the path of the neutron beam the phase fraction of the aluminium phases was also refined.

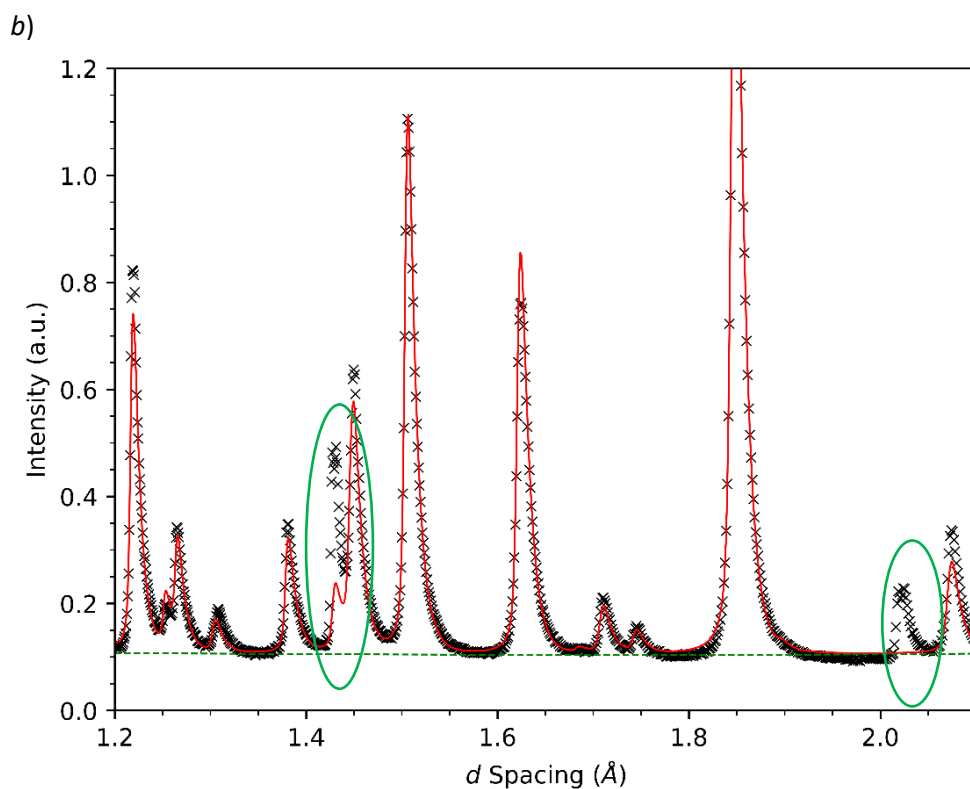
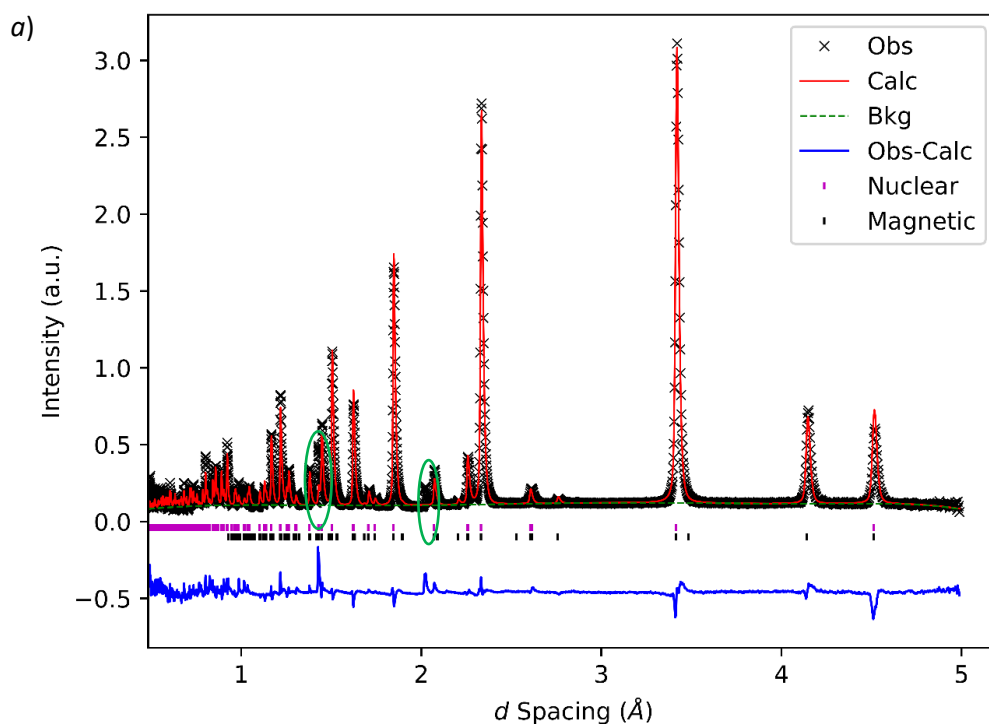


Fig. 3.7: **a)** Refinement of NPD data collected at 112 K in zero field, with fit parameters: $\chi^2 = 27.40$, $R_p = 6.5\%$ and $wRp = 10.1\%$; including nuclear and magnetic scattering models showing that some peaks still remained unfit. Calc = Calculated fit, Obs = Observed points, Bkg = Background. Nuclear tick marks represent peaks produced by nuclear scattering while Magnetic tick marks represent peaks originating from magnetic scattering. The blue curve is the difference curve between the observed and calculated model. **b)** A magnification of a portion of the NPD refinement shown in a), showing the unfit peaks.

Comparing the refinements of the measurements taken in zero field at 20 and 112 K, Fig. 3.8 and Fig. 3.9 respectively, shows that the crystal and magnetic structures are the same at both temperatures suggesting that no structural or magnetic phase changes occurred over this temperature range. Full refinement parameters can be seen in Table 3.2. Within the magnetic phase the moments of the Ru ions were found to be antiferromagnetically ordered both within the Ru layers and between them, with the moments being directed along the c -axis and having magnitudes of $\mu = 1.471$ and $1.465 \pm 0.018 \mu_B$, at 20 and 112 K, respectively. Thus, producing an arrangement equivalent to G-type AFM order within a cubic cell, as seen in Fig. 3.10.

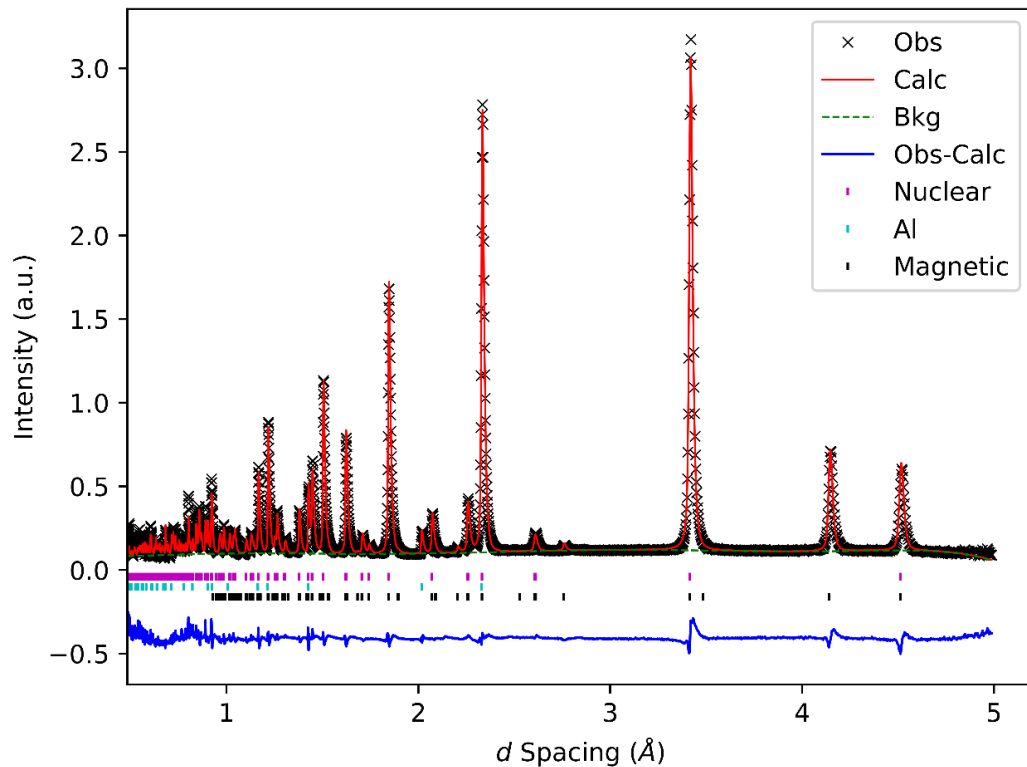


Fig. 3.8: Rietveld refinement of NPD data collected in zero applied field at 20 K. Calc = Calculated fit; Obs = Observed points, Bkg = Background. Nuclear tick marks represent peaks produced by nuclear scattering while magnetic tick marks represent peaks originating from magnetic scattering. The blue curve is the difference curve between the observed and calculated model. Al tick marks indicate peaks due to the aluminium.

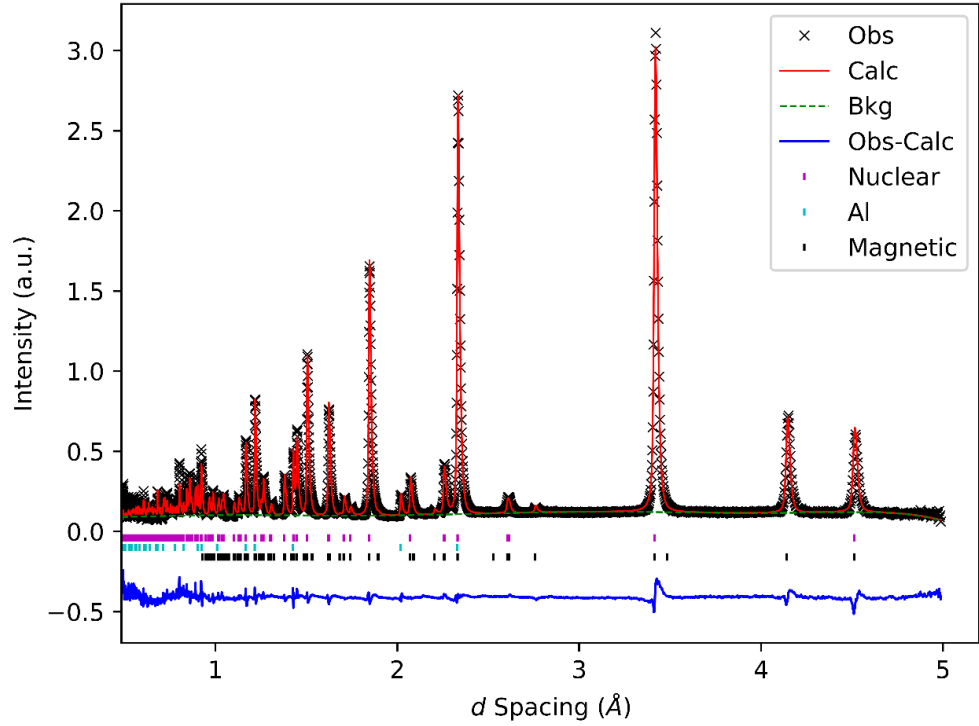


Fig. 3.9: Rietveld refinement of NPD data collected in zero applied field at 112 K. Calc = Calculated fit; Obs = Observed points, Bkg = Background. Nuclear tick marks represent peaks produced by nuclear scattering while magnetic tick marks represent peaks originating from magnetic scattering. The blue curve is the difference curve between the observed and calculated model. Al tick marks indicate peaks due to the aluminium.

Table 3.2: Rietveld refinement parameters for NPD collected at 20 and 112 K in zero field, corresponding to the refinement shown in Fig. 3.8 and 3.9. The brackets signify atom position within the unit cell, e.g. (1/3, y, z). Where an axis coordinate, e.g. x, has been replaced by a value, the value corresponds to the atom's position along that axis.

Refined parameter	T = 20 K	T = 112 K
R_p (%)	5.60	5.35
wR_p (%)	5.53	5.47
χ^2	12.32	8.036
a (Å)	5.21081(4)	5.21007(7)
c (Å)	5.22542(5)	5.2282(15)
Cell volume (Å ³)	122.875(2)	122.907(4)
Sr - $U_{iso}/U_e \times 100$ (Å ²)	1.84(7)	2.05(7)
Ru - $U_{iso}/U_e \times 100$ (Å ²)	0.41(5)	0.60(5)
O - $U_{iso}/U_e \times 100$ (Å ²)	1.37(4)	1.49(5)
Sr (0, 0, 0)	-	-
Ru (1/3, 2/3, 1/2)	-	-
O (x, 0, z)	0.37793(17) 0.3011(4)	0.37803(17) 0.3006(4)

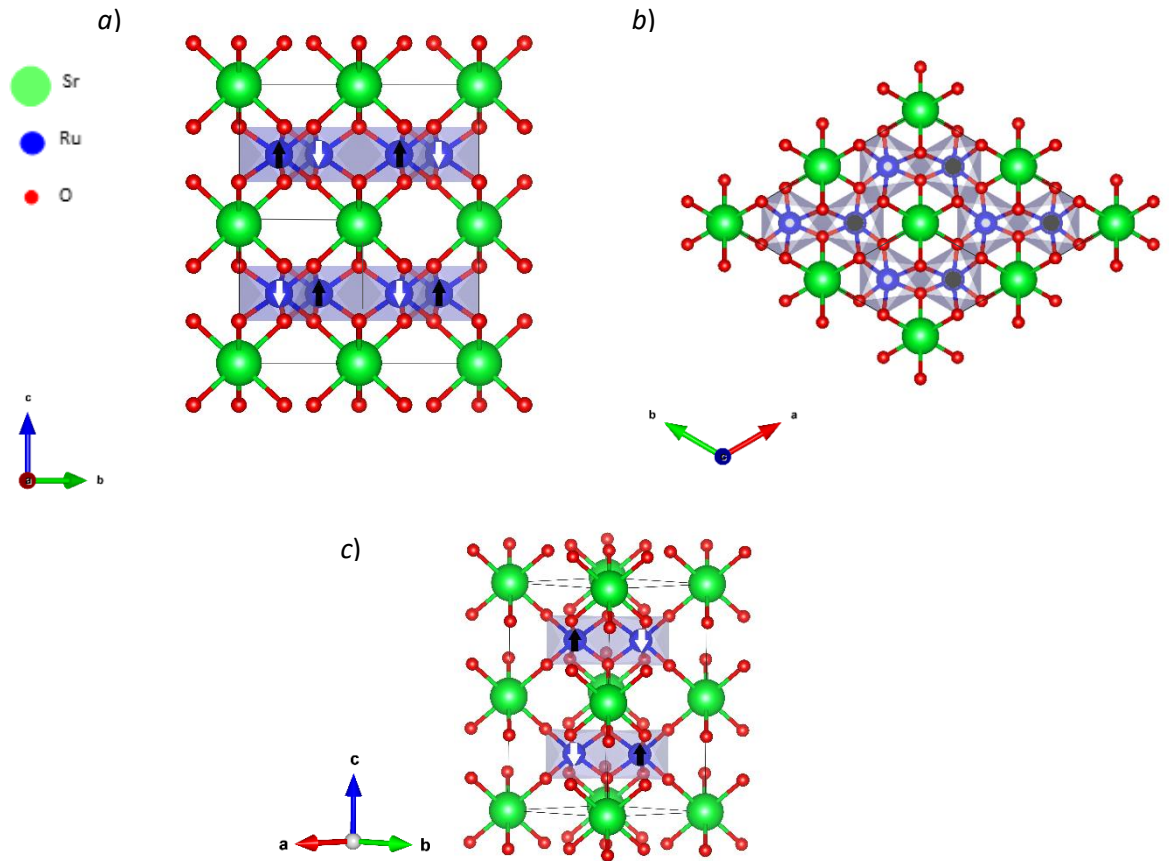


Fig. 3.10 : The crystal and magnetic structure of SrRu_2O_6 . Shown parallel to the c -axis, **a)**, and parallel to the a - b plane, **b)**. Green represents the Sr atoms, blue the Ru atoms and red the oxygen atoms. Black arrows represent spin up moments and white spin down. These representations were produced using *cif* files extracted from the Rietveld refinements at 112 K using the VESTA software. **c)** Representation of the magnetic unit cell, which is equivalent to G-type AFM order for a cubic cell.

To allow a comparison of the measured and expected magnetic moments the theoretically expected moment was calculated by considering the following. Within SrRu_2O_6 the Ru^{5+} atoms have unfilled shells which contain unpaired valence electrons, leading to the ions having a net magnetic moment as predicted by the theory described in section 1.1. Using these equations it is possible to calculate the expected moment for a Ru^{5+} ion as follows.

To calculate the magnetic moment of the ruthenium ions it is first necessary to establish how many unpaired electrons there are in each ion and which quantum states they occupy. So as to find the orbital, L , and spin, S , angular momenta associated with each electron and be able to compute the total angular momentum, J ,

associated with the ion. Firstly, the electron configuration for a Ru atom is $[\text{Kr}] 4d^7 5s^1$ [86], however the Ru ions within SrRu_2O_6 are in a 5+ oxidation state and so five electrons need to be removed to find the electron configuration of Ru^{5+} , resulting in an electron configuration of $[\text{Kr}] 4d^3$. The number of quantum states that can be occupied by electrons in a given orbital is given by $2(2l + 1)$, where l is the orbital angular momentum quantum number of the specified orbital. Here the orbital being filled is a d -orbital, with $l = 2$, and therefore there are ten quantum states available. Note that the magnetic quantum number, m_l , can take values ranging from $-l$ to l in integer steps and due to electrons having a spin of a $\frac{1}{2}$, the spin quantum number, m_s , can only take values of $+\frac{1}{2}$ and $-\frac{1}{2}$.

From Section 1.1 the formula for calculating the magnetic moment of an atom is given by Eq. 1.2 shown again here for convenience as Eq. 3.1:

$$\mu = g_J \mu_B \sqrt{J(J + 1)} \quad (3.1)$$

However to first approximation, no orbital contribution is expected for the ground state of a Ru^{5+} ($^4F_{3/2}$) ion in an octahedral ligand field, hence the spin-only formula, Eq. 3.2, can be used.

$$\mu_S = g_S \mu_B \sqrt{S(S + 1)} \quad (3.2)$$

Following Hund's rules the three electrons in the $4d$ orbital will occupy states with $m_s = +\frac{1}{2}$ leading to $S = \frac{3}{2}$. Substituting this value along with the g -factor for an electron, $g_s = 2$, into Eq. 3.2 gives the expected moment for a Ru^{5+} ion of $\mu_{\text{Ru}^{5+}} = \sqrt{15} \mu_B$, which is $\approx 3.87 \mu_B$.

Within experiment, when measuring the magnetic moment using neutrons it is expected that a maximum spin only value of $1 \mu_B$ per unpaired electron in the system will be seen [87]. This comes from the definition of the Bohr magneton itself, which can also be defined as the value of the intrinsic spin of an electron. This results in the Ru^{5+} moment measured in the neutron diffraction data actually being expected to be $3 \mu_B$.

Considering the error of $\sim 5.0 \times 10^{-2} \mu_B$ reported by Parkinson *et al.* [72] the measured moment can be quoted to $1.5(1) \mu_B$ with confidence; half that of the expected moment of $3 \mu_B$. A corollary of this is that there is a large amount of covalence between the Ru and O atoms causing the magnetic moment to be distributed between the Ru and O sites with $\sim 50\%$ of the moment being associated with the O site. A finding consistent with the results of several studies [41, 42, 45]. This large degree of covalence gives rise to the high energy scales responsible for the magnetic ordering and can explain the high ordering temperature [45], through the large amounts of covalence being favourable for inter-site coupling between moments, particularly through the super exchange interaction.

3.4: Applied Field Powder Neutron Diffraction Data

Similar to the zero field data, all of the NPD data sets collected in applied fields showed the same structure over the range of fields and temperatures. Thus, no structural or magnetic phase transitions were found to occur with temperature, applied field or both. Here, low temperature, 20/30 K, and high temperature, 150/130 K, refinements for 0.1, 3 and 7 T are shown in Fig. 3.11 to 3.13 and the refined lattice parameters for these fields are shown in Tables 3.3 to 3.5, to show the consistency of the structure, while the refinements and refined parameters for the full range of temperatures and fields can be found in Appendix 1.

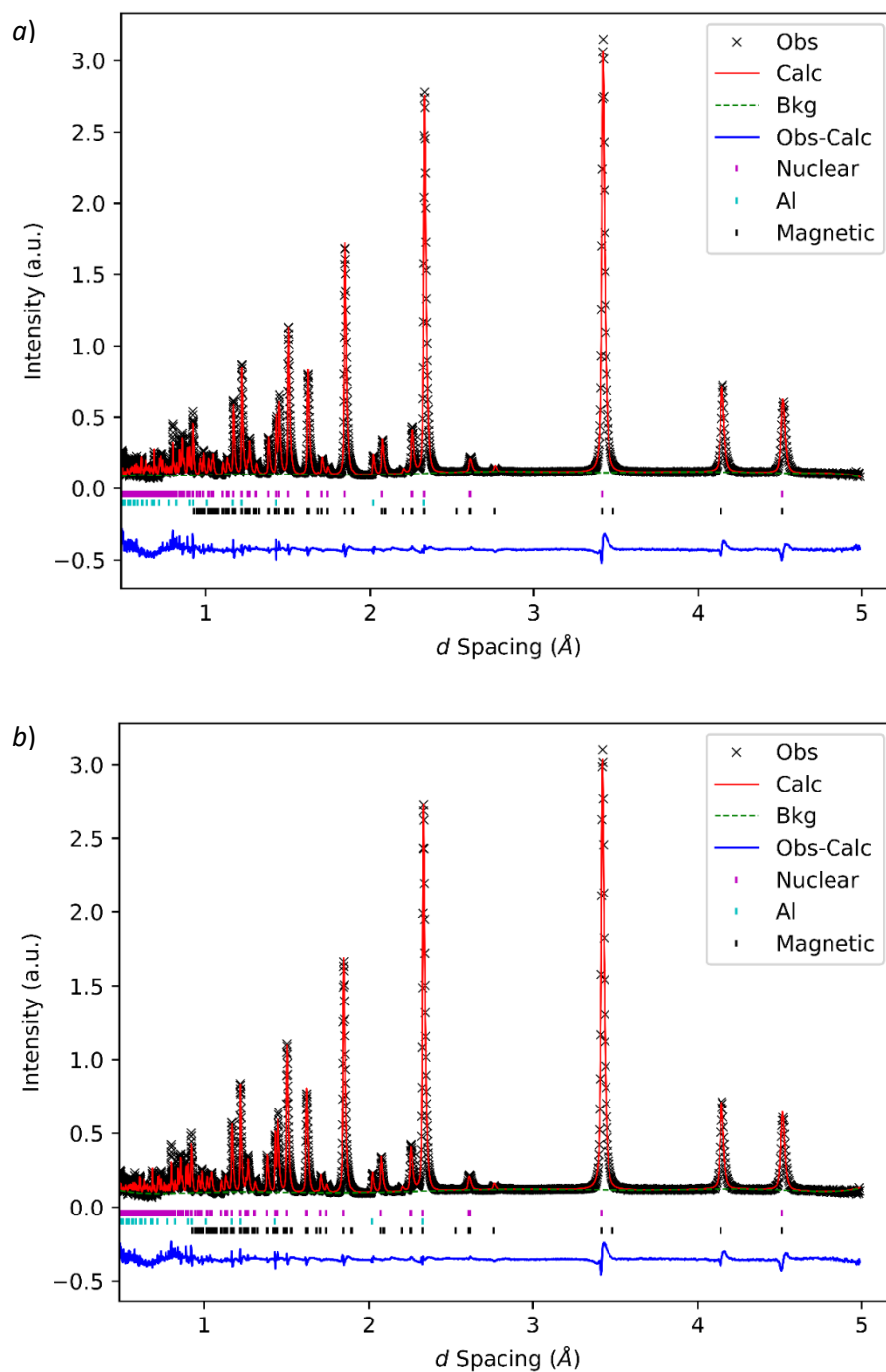


Fig. 3.11 a and b: Rietveld refinement of NPD data collected in an applied field of 0.1 T at 20 K and 150 K, respectively. Calc = Calculated fit; Obs = Observed points, Bkg = Background. Nuclear tick marks represent peaks produced by nuclear scattering while Magnetic tick marks represent peaks originating from magnetic scattering. The blue curve is the difference curve between the observed and calculated model. Al tick marks indicate peaks due to aluminium.

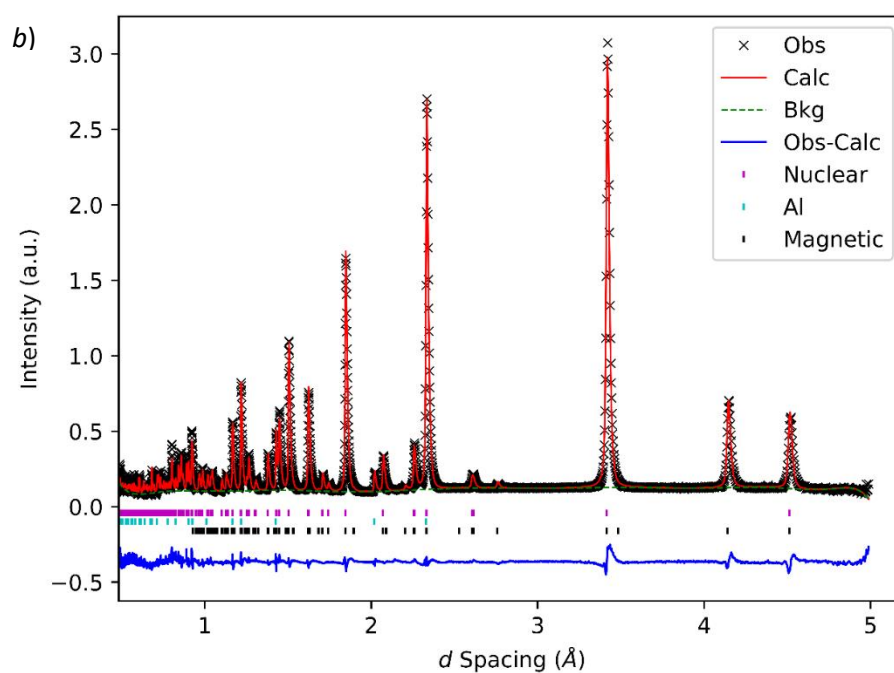
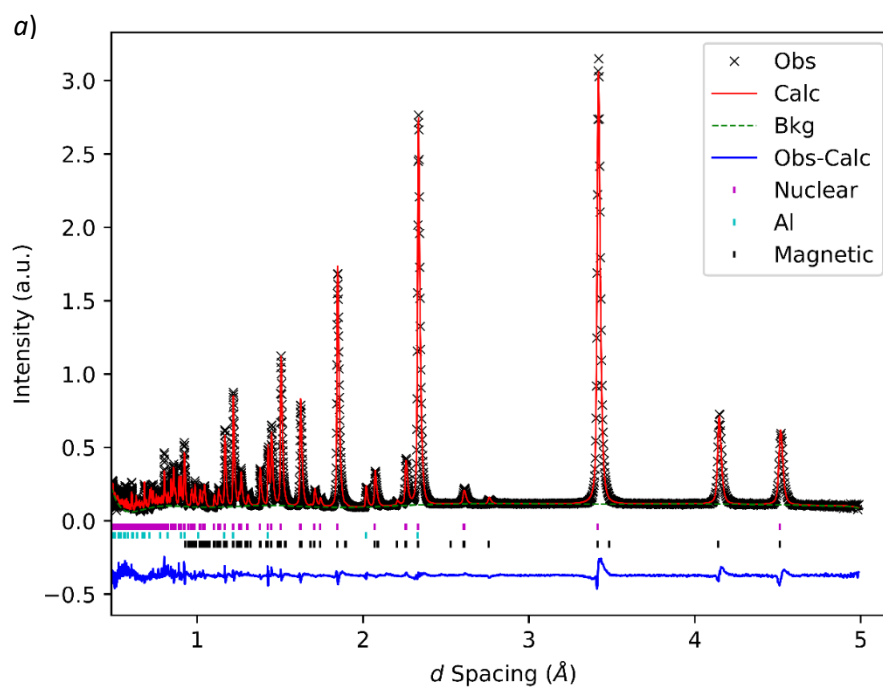


Fig. 3.12 a and b: Rietveld refinement of NPD data collected in an applied field of 3 T at 20 K and 130 K, respectively. Calc = Calculated fit; Obs = Observed points, Bkg = Background. Nuclear tick marks represent peaks produced by nuclear scattering while Magnetic tick marks represent peaks originating from magnetic scattering. The blue curve is the difference curve between the observed and calculated model. Al tick marks indicate peaks due to aluminium.

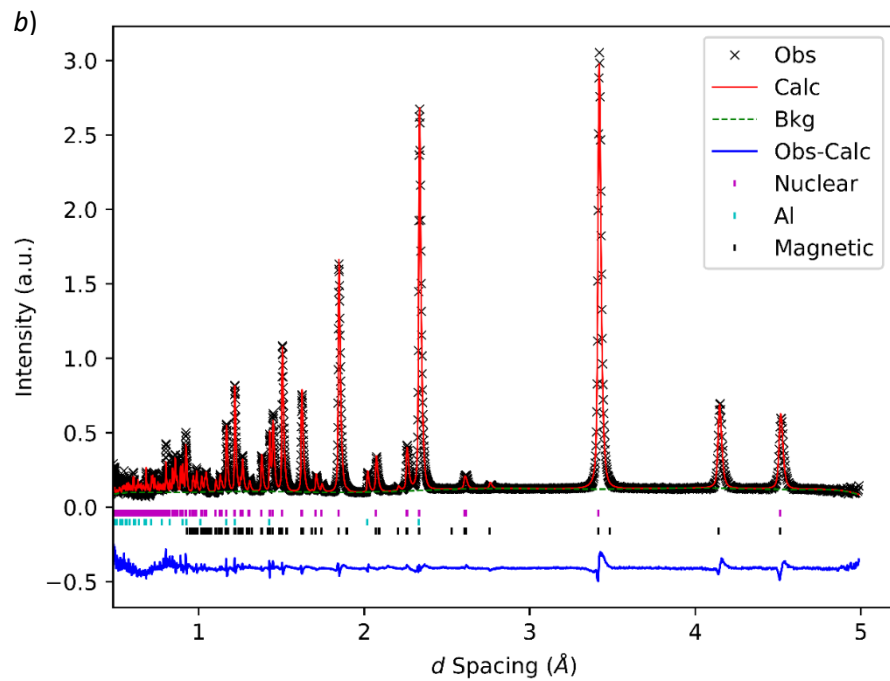
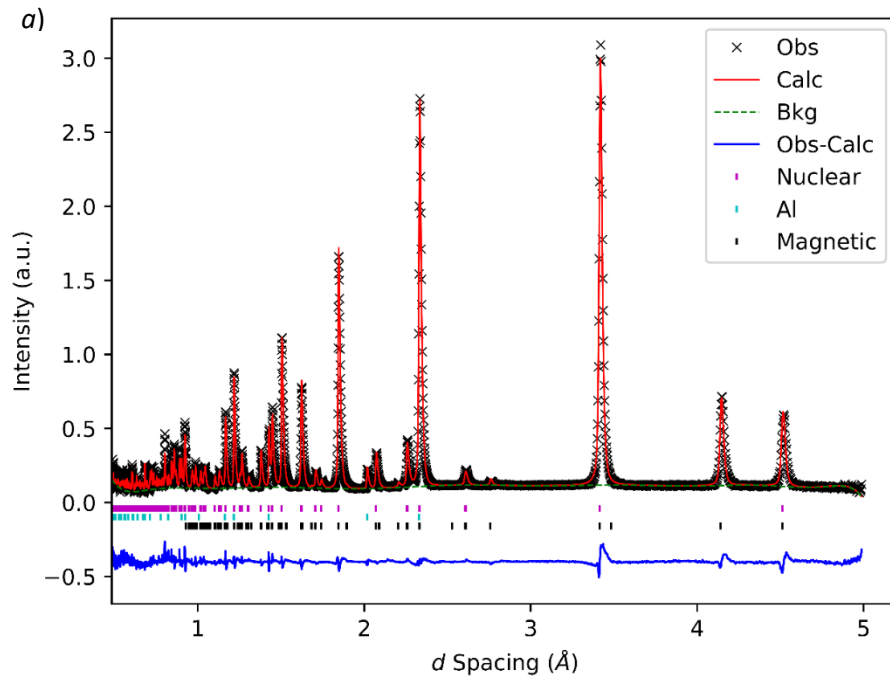


Fig. 3.13 a and b: Rietveld refinement of NPD data collected in an applied field of 7 T at 30 K and 150 K, respectively. Calc = Calculated fit; Obs = Observed points, Bkg = Background. Nuclear tick marks represent peaks produced by nuclear scattering while Magnetic tick marks represent peaks originating from magnetic scattering. The blue curve is the difference curve between the observed and calculated model. Al tick marks indicate peaks due to aluminium.

Table 3.3: Refined lattice parameters for the 0.5 T NPD data.

T (K)	a and b (Å)	c (Å)	Cell Vol. (Å ³)	Rp (%)	wRp (%)	χ ²
1.00	5.21091(7)	5.22544(13)	122.880(4)	4.96	5.12	8.583
10.00	5.21087(7)	5.22544(13)	122.878(4)	4.92	5.13	8.629
20.00	5.21084(6)	5.22549(13)	122.878(4)	4.57	4.93	7.965
30.00	5.21085(6)	5.22547(13)	122.878(4)	4.55	4.89	7.825
40.00	5.21080(6)	5.22549(13)	122.876(4)	4.58	4.91	7.910
50.00	5.21080(7)	5.22566(15)	122.880(4)	5.06	5.70	10.74
60.00	5.21071(6)	5.22578(13)	122.879(4)	4.52	4.84	7.747
80.00	5.21046(6)	5.22594(12)	122.870(4)	4.33	4.55	6.867
94.00	5.21044(7)	5.22697(14)	122.894(4)	4.99	5.26	9.243
129.20	5.21011(6)	5.22864(13)	122.918(4)	4.70	4.81	7.715

Table 3.4: refined lattice parameters for the 3 T NPD data.

T (K)	a and b (Å)	c (Å)	Cell Vol. (Å ³)	Rp (%)	wRp (%)	χ ²
1.70	5.21084(11)	5.22522(21)	122.871(6)	5.01	5.34	14.03
10.00	5.21069(7)	5.22539(14)	122.868(4)	5.02	5.43	14.51
20.11	5.21081(7)	5.22535(14)	122.873(4)	4.89	5.33	13.99
30.00	5.21079(7)	5.22543(14)	122.874(4)	4.98	5.39	14.28
40.00	5.21078(7)	5.22540(14)	122.872(4)	5.05	5.42	14.42
49.75	5.21067(7)	5.22556(14)	122.872(4)	4.97	5.32	13.90
60.00	5.21063(7)	5.22575(15)	122.874(4)	4.98	5.37	14.15
80.00	5.21052(8)	5.22588(15)	122.872(4)	4.92	5.27	13.6
100.00	5.21034(7)	5.22637(15)	122.875(4)	4.88	5.30	13.85
150.00	5.21005(7)	5.22777(15)	122.894(4)	4.78	5.17	13.21

Table 3.5: refined lattice parameters for the 7 T NPD data.

T (K)	a and b (Å)	c (Å)	Cell Vol. (Å ³)	Rp (%)	wRp (%)	χ ²
1.00	5.21096(7)	5.22545(14)	122.882(4)	5.03	5.46	9.729
10.00	5.21097(7)	5.22558(14)	122.886(4)	5.04	5.27	9.033
30.00	5.21088(7)	5.22558(14)	122.881(4)	5.02	5.19	8.775
50.00	5.21083(8)	5.22574(16)	122.883(5)	5.79	6.12	12.35
80.00	5.21072(34)	5.22613(5)	122.8872(16)	4.89	5.14	8.707
100.00	5.21049(7)	5.22693(14)	122.895(4)	4.85	5.10	8.633
150.00	5.21010(7)	5.22885(14)	122.922(4)	4.91	5.26	9.135

3.5: Temperature Dependence of the Nuclear and Magnetic Structures

Comparing the lattice parameters shown in Tables 3.3 to 3.6 a change in lattice parameters due to the increase in temperature is observed in all applied magnetic fields. Normally when the temperature of a crystal is increased it is expected that the crystal will expand due to the increase in kinetic energy of the constituent atoms, associated with the increase in the internal energy. This can be seen to occur for SrRu_2O_6 as the cell volume increases with temperature by an average of $0.032(2) \text{ \AA}^3$ over the 149 K increase, see Fig. 3.14.

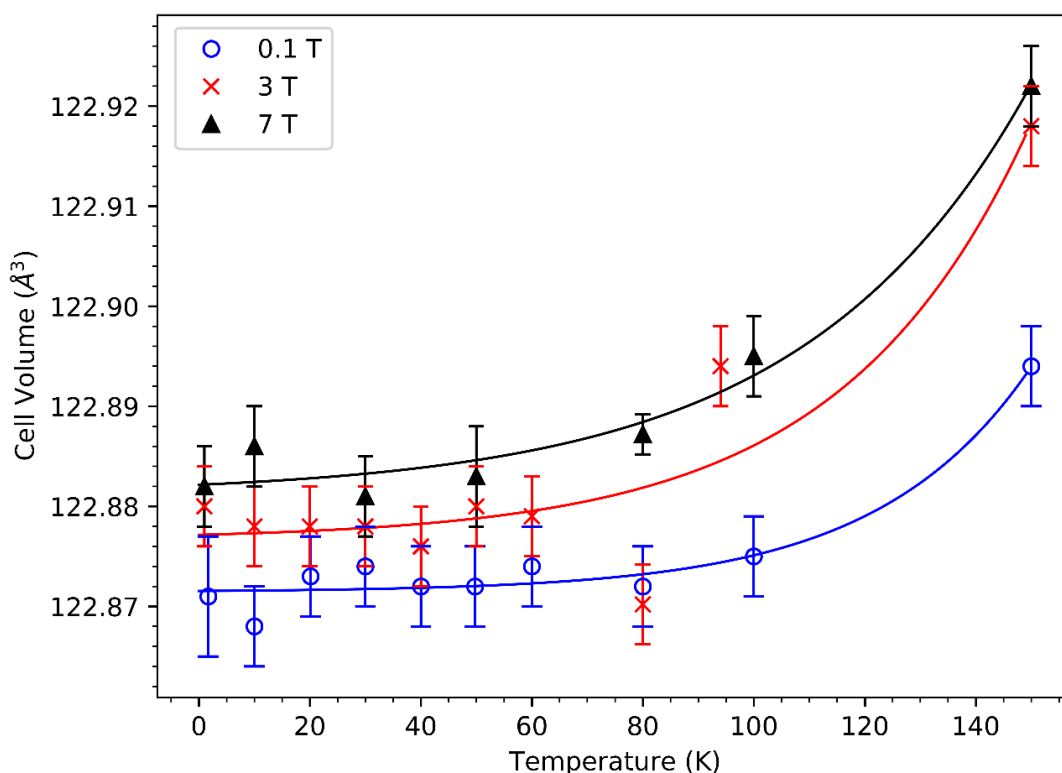


Fig. 3.14: Plot showing the cell volume of SrRu_2O_6 plotted as a function of temperature at various fields. The lines of best fit were made using exponential functions, which were fitted using a least squares fit.

However, this volume expansion is somewhat unconventional because it is anisotropic; being produced by a relatively large expansion along only the c -axis, of on average $2 \times 10^{-5} \text{ \AA K}^{-1}$, and a contraction along the a and b axes, of approximately $5 \times 10^{-6} \text{ \AA K}^{-1}$, over the studied temperature range. This anisotropic thermal expansion is consistent with previous work [61]. See Fig. 3.15 and 3.16 for plots of the lattice parameters as a function of both temperature and applied magnetic field.

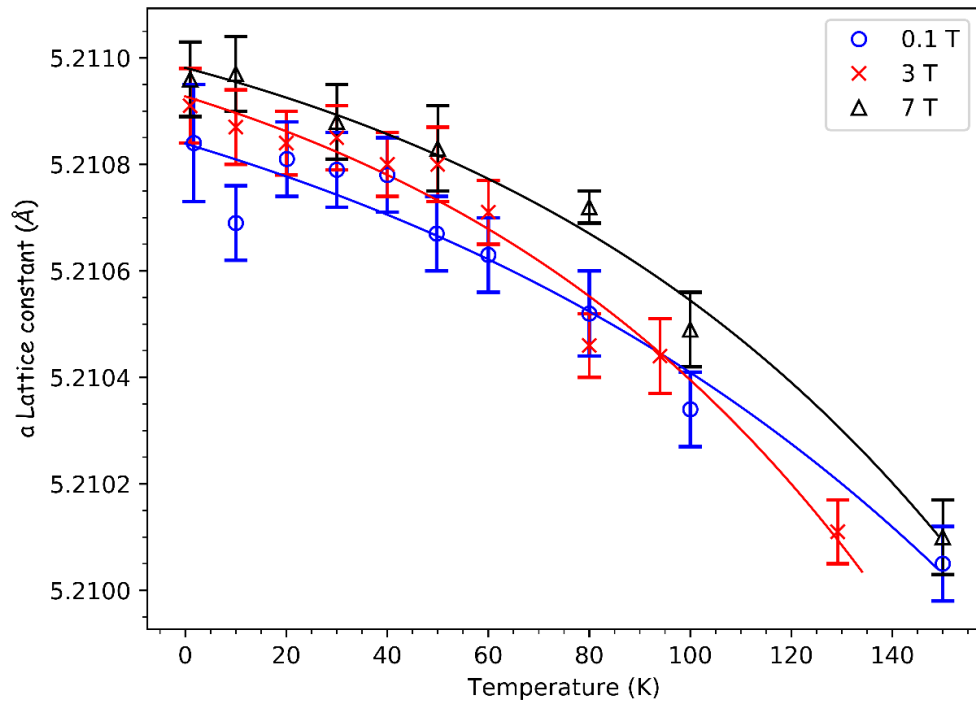


Fig. 3.15: A plot showing the change in the a lattice parameter of SrRu_2O_6 as a function of temperature in a range of applied fields. Note that the b lattice constant is equal to the lattice a constant. The lines of best fit were made using exponential functions, which were fitted using a least squares fit.

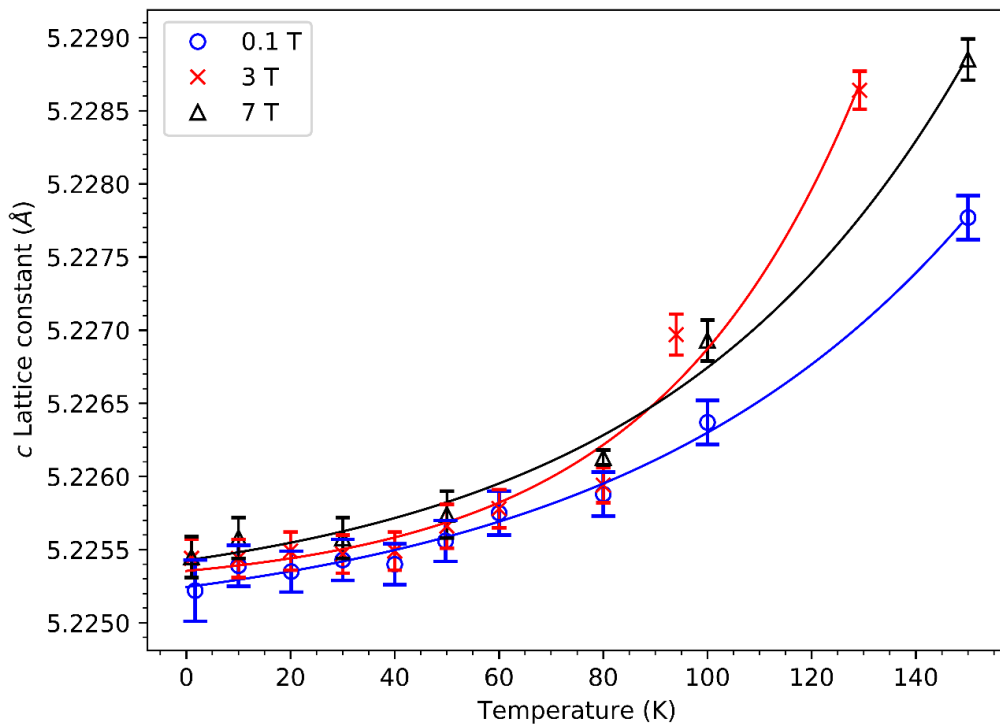


Fig. 3.16: A plot showing the change in the c lattice parameter of SrRu_2O_6 as a function of temperature in a range of applied fields. The lines of best fit were made using exponential functions, which were fitted using a least squares fit.

From consideration of the exchange integrals of antiferromagnetic exchange and the dipole-dipole interaction being dependent on distance, the spin configuration of an antiferromagnetic crystal can be related to ionic displacement [88, 89]. The negative thermal expansion within the a - b plane is likely to be caused by magnetoelastic (ME) coupling between intralayer, in-plane, Ru atoms [89], as the Ru ions will try to lower their energy by ordering their moments through remaining close enough to one another to allow antiferromagnetic exchange to occur. This hypothesis is supported by the fact that the in-plane Ru-Ru atomic separation is only found to decrease with temperature as shown in Fig. 3.17; meaning that the strength of the exchange interactions which cause the ME coupling will stay constant or increase.

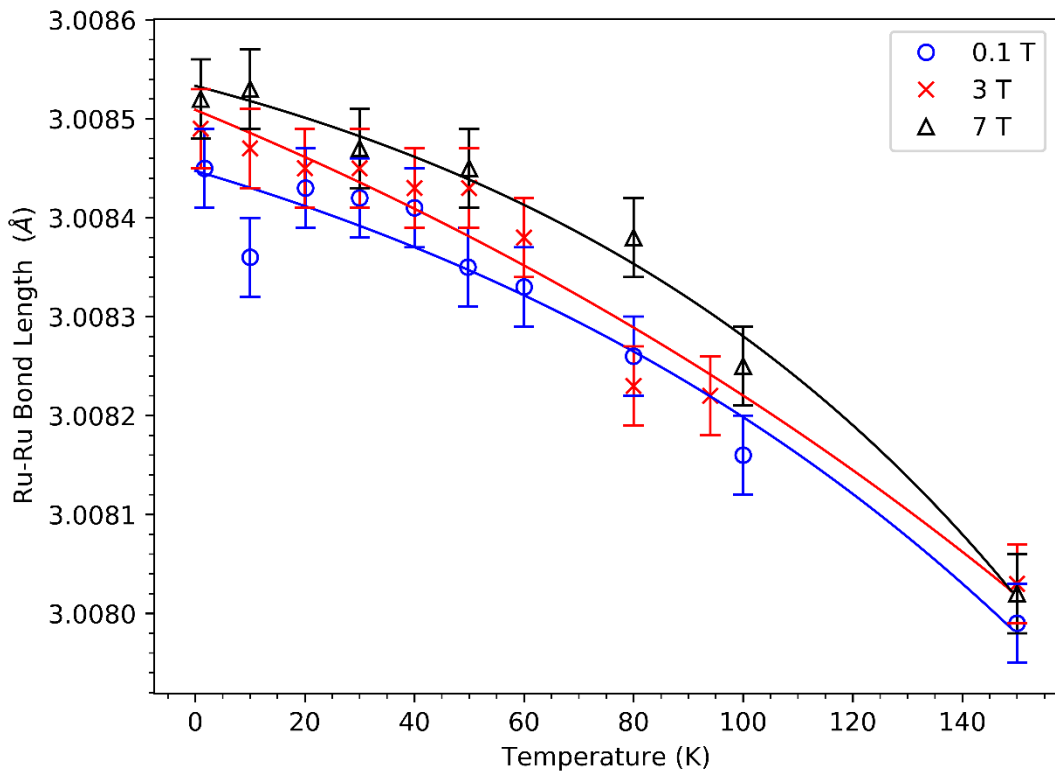


Fig. 3.17: Ru-Ru bond length plotted as a function of temperature, in fields of 0.1, 3 and 7 T. The lines of best fit were made using exponential functions, which were fitted using a least squares fit.

The magnitude of the refined Ru⁵⁺ moment, for each temperature and field, can be seen tabulated in Table 3.6.

Table 3.6: Table showing the refined magnetic moment for each set of data collected in a given temperature and field. Temperature increasing down the columns and field increasing along the rows. Temperatures in brackets indicate the temperature at which the data was collected in cases where the temperature was not quite 100 and 150 K. The average was calculated over the first 100 K not including the 150 K data and the uncertainties were calculated using statistical analysis.

Temperature (K)	Applied Field (T)			
	0.1	0.5	3	7
	Refined Moment ($\pm 0.02 \mu_B$)			
1.00	1.47	1.46	1.47	1.47
10.00	1.47	1.46	1.47	1.48
20.00	1.46	1.47	1.47	-
30.00	1.45	1.46	1.47	1.47
40.00	1.46	1.47	1.47	-
50.00	1.46	1.47	1.47	1.47
60.00	1.46	1.47	1.47	-
80.00	1.45	1.47	1.47	1.47
100.00	1.46	1.46	1.47 (@94 K)	1.46
150.00	1.46	1.46	1.46 (@130 K)	1.45

Considering the values in Table 3.6 and more specifically the moments at the lowest temperature, the Ru moment was found to have a value of $\mu_{Ru^{5+}} = 1.47(2) \mu_B$. Again, considering the possible error associated with an inaccurate form factor, the moment can be quoted to $1.5(1) \mu_B$ with a good degree of confidence.

3.6: Magnetoelastic and Magnetostrictive Effects

Magnetoelastic (ME) coupling describes the coupling between atoms that comes from magnetic exchange interactions. The strength of these interactions are governed by, among other factors, the separation between atoms. Thus by virtue of the definition of strain, the change in length of a material divided by its original length, these interactions therefore also have a strain dependence and so ME coupling can equally

be considered as the coupling between magnetic electrons, or magnetic energy, and strains in the lattice [90].

Most general models for ME coupling, such as that presented in reference [89], are described by a Hamiltonian which is dependent on intrinsic energies which do not depend on magnetic order; \mathcal{H}_{PM} which describes the energy of the system in its paramagnetic state. In addition there are terms which describe the magnetic order and thus have a spin dependence, \mathcal{H}_{Spin} . Consequently the full Hamiltonian is given by Eq. 3.3

$$\mathcal{H} = \mathcal{H}_{PM} + \mathcal{H}_{Spin} \quad (3.3)$$

where \mathcal{H}_{Spin} is made up of Heisenberg symmetric exchange interactions, shown to first order in Eq. 3.4

$$\mathcal{H}_{Spin} = \mathcal{H}_0 + \sum_{i,i'} \frac{\partial J_{ii'}}{\partial u_m} \mathbf{S}_i \cdot \mathbf{S}_{i'} u_m + \sum_{i,i'} \frac{\partial J_{ii'}}{\partial \eta_j} \mathbf{S}_i \cdot \mathbf{S}_{i'} \eta_j \quad (3.4)$$

as well as antisymmetric Dzyaloshinskii-Moriya interactions and single ion anisotropies, which are not shown. In Eq. 3.4, \mathcal{H}_0 is the zero-order term for which the atomic displacement from a reference structure, u_m , and the strain in Voigt notation, η_j , are zero, while $J_{ii'}$ is the exchange parameter between the spins \mathbf{S}_i and $\mathbf{S}_{i'}$.

Being able to describe ME coupling i.e. compute lattice changes from this model explicitly, shows the relation between the spin configuration and lattice strains, which defines ME coupling.

ME coupling can also give rise to a change in lattice dimensions when a magnetic field is applied. This is known as magnetostriction, λ , and describes the change in a materials dimensions due to the change in magnetisation and energy associated with a magnetic field being applied [89]. Magnetostriction is experimentally observed to increase with the applied field strength until it reaches a constant saturation value, λ_{sat} [91]. There are two main mechanisms for magnetostriction, the crystal field mechanism and the exchange striction model [92].

Exchange striction receives its name from the fact that this type of ME strain comes from two ion interactions, which are usually dominated by exchange terms from Heisenberg and RKKY (Ruderman–Kittel–Kasuya–Yosida) type interactions. When there is no distribution deformation, i.e. the distribution is spherically symmetric, such as for the 4f distribution when $L = 0$, the application of a field can reverse the spontaneous exchange striction coming from the antiferromagnetic order, shown in Fig. 3.18 d-f [92].

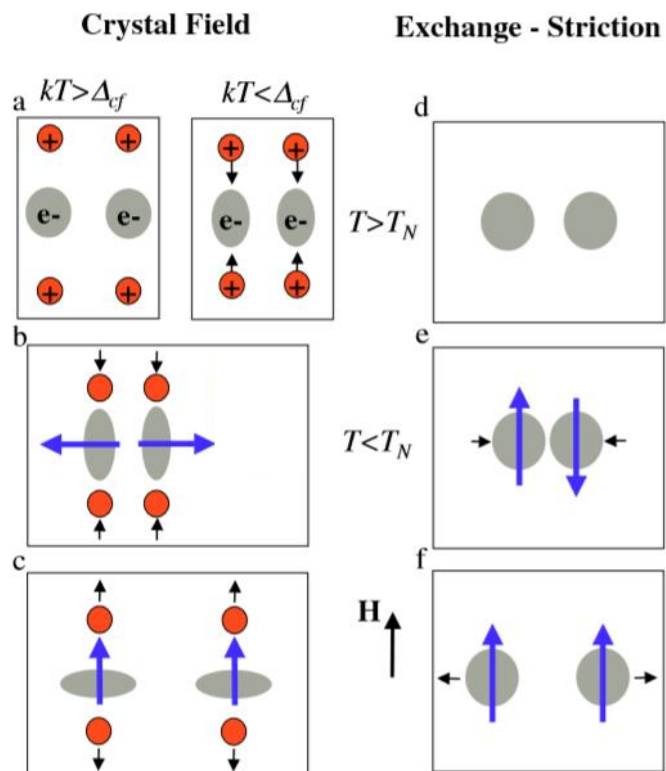


Fig. 3.18: Schematic representation of magnetostriction. a-c) Crystal field mechanism d-f) exchange striction. a) The strain induced due to the positive charges within the crystal field and the charge distribution of the magnetic ion. b) Demonstration of how the charge distribution is coupled to the moment of a magnetic ion. c) The reversal of a charge distribution due to an applied field. d) Two neighbouring ions in the paramagnetic state, in zero field. e) Spontaneous exchange striction. f) The reversal of spontaneous exchange striction by an applied magnetic field. Taken from [92].

Looking at the change in cell volume shown in Fig. 3.14 in section 3.5, it can be seen that there is an increase in cell volume with applied field i.e a positive magnetostriction. This positive magnetostriction is most likely to be caused by the ME coupling between the intralayer Ru ions; which is thought to be responsible for the anisotropic thermal expansion discussed earlier. Magnetostriction can be considered as the strain induced by an applied field, Eq. 3.5,

$$\lambda = \frac{\Delta l}{l} \quad (3.5)$$

and the primary magnetostrictive effects are: The Joule effect, a contraction or expansion of the material in a certain direction. The volume effect, usually a weak volume expansion, and the Wiedemann effect, which produces a shearing effect or shear strain [91]. The volume magnetostrictive effect will be denoted here as λ_V and can be calculated using Eq. 3.6:

$$\lambda_V = \frac{\Delta V}{V} \quad (3.6)$$

In this equation ΔV is defined as the volume of the sample in a larger field minus the volume of the sample in a smaller field at the same given temperature. This leads to a positive value of λ representing an expansion and a negative value representing a contraction. Due to only having two measurements at zero field the 0.1 T data was used as the base measurement for calculation of λ , See Eq. 3.7 for clarification.

$$\lambda_{V_{3T}} = \frac{V_3 - V_{0.1}}{V_{0.1}} \quad (3.7)$$

Calculated values for λ_V can be found in the appendices, Table.App.2.1. Uncertainties were calculated using the standard error propagation equation Eq. 3.8

$$\delta Z^2 = \left(\frac{\partial Z}{\partial x_1} \cdot \delta x_1 \right)^2 + \left(\frac{\partial Z}{\partial x_2} \cdot \delta x_2 \right)^2 \cdots \left(\frac{\partial Z}{\partial x_n} \cdot \delta x_n \right)^2 \quad (3.8)$$

where Z is the quantity in question, in this case λ_V , and x_a represents each variable used in the calculation, e.g. V_3 and $V_{0.1}$. An uncertainty of 5×10^{-5} , on the same order as the values for λ_V themselves, was returned suggesting overall the most reliable information that can be concluded from this is that the size of the magnetostriction is

$\sim 5 \times 10^{-5}$. The cell volume vs temperature plot, Fig. 3.14, shows an increase in λ_V with field, as expected [91], and also an increase in λ_V with temperature. One possible explanation for the increase in λ_V with temperature maybe that as the magnetostriction produces a larger atomic separation, the interatomic forces and correlation effects which depend on separation are weaker allowing thermal effects to have a larger impact causing more expansion in the lattice.

In systems where $4f$ ions have zero orbital angular momentum $\mathbf{L} = 0$, the crystal field strain is zero. Resulting from the spherically symmetric charge distribution of the ion causing no strain in the crystal. Assuming the same is true for $4d$ ions with $\mathbf{L} = 0$, which the Ru in SrRu_2O_6 are, then the crystal field mechanism can be neglected and only the stronger exchange striction considered. This should be the case as their will be no spin orbit coupling for an $\mathbf{L} = 0$ system and hence no deformation of the charge distribution leading to any crystal field striction. Even if this were not the case for $4d$ elements, it is reasonable to expect the stronger exchange striction to dominate the magnetostriction in the case of SrRu_2O_6 . This could be expected as it is likely that there will be a large exchange striction coming from the direct overlap between half filled, Ru, t_{2g} orbitals and super exchange coupling between the O p_2 and Ru d_{zx} and d_{yz} orbitals of neighbouring atoms [42].

The large amounts of covalence between the Ru and O ions, suggested by the greatly reduced moment, would suggest that the superexchange between in plane Ru, mediated by O, dominates the exchange interaction. Considering the Goodenough-Kanamori rule [47, 93] which states that the superexchange interactions, J , are inversely proportional to the Hubbard repulsion and directly proportional to the effective orbital hopping squared, $\frac{t^2}{U}$. With the knowledge that the hopping term increases with a decreasing bond length and an increase in the bond angle between the magnetic and non-magnetic ions [89] makes it apparent that the strength of the superexchange interaction depends on these parameters. The Hubbard repulsion, which decreases with an increase in bond length, represents the Coulomb repulsion associated with pairs of electrons occupying the same site, also known as an onsite repulsion [2].

Applying this to the evolution of the Ru-O-Ru bond angle and Ru-O bond lengths, in Fig. 3.19a and b, determined from the refinements, could suggest that the superexchange interaction does dominate the exchange interaction. As both the bond angle and bond length remain constant within error, over the studied range. Suggesting that the most energetically favourable configuration for superexchange is maintained, even while the Ru-Ru inter atomic distance increases due to the magnetostriction. This result is further supported by the Monte Carlo simulations and theoretical calculations made by Tian *et al.* [42] which also found superexchange to dominate the exchange interaction.

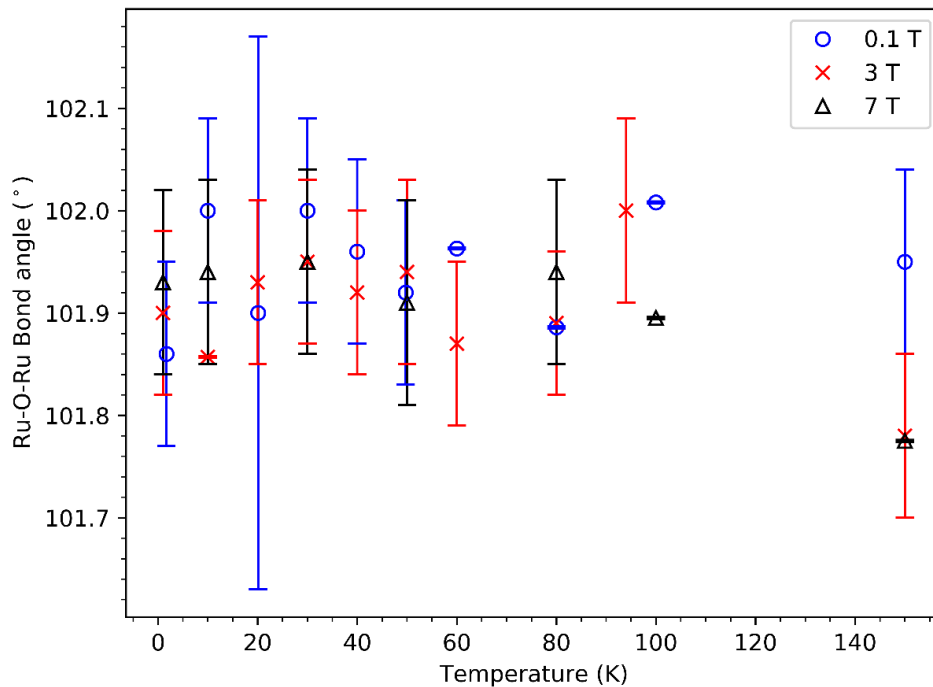


Fig. 3.19a: Plot showing the Ru-O-Ru bond angle as a function of temperature in different applied magnetic fields.

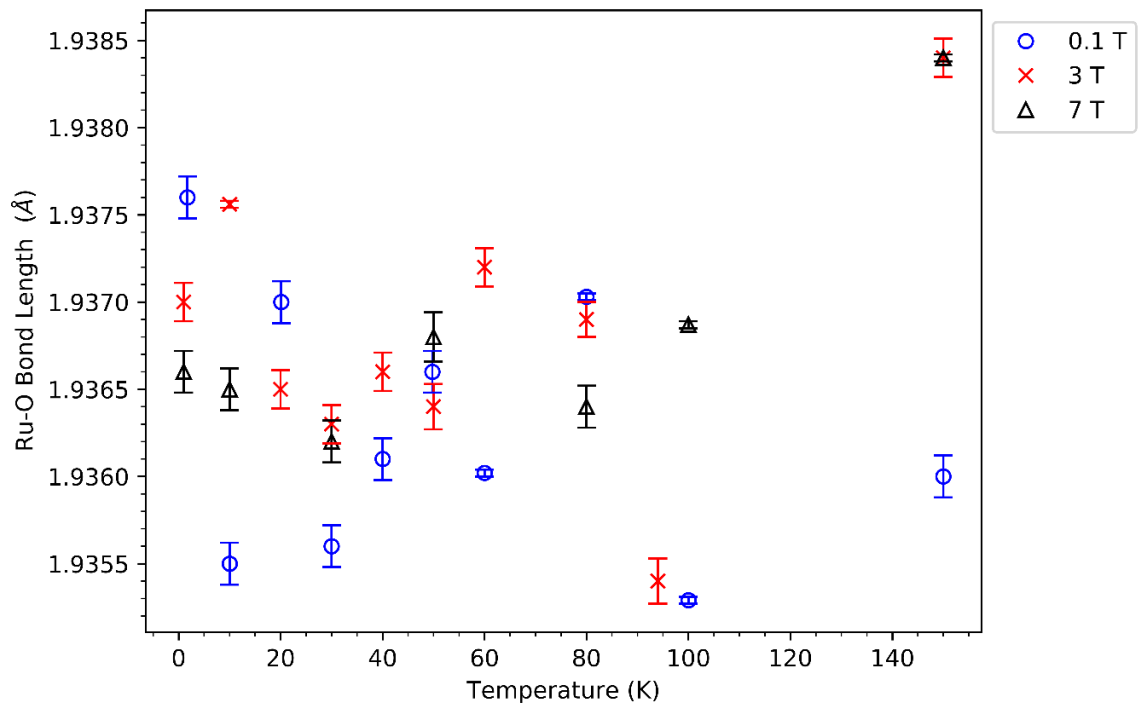


Fig. 3.19b: Plot showing the Ru-O bond length as a function of temperature in different applied magnetic fields. Although the uncertainty in each quantity is small the overall spread of the data would suggest that the Ru–O bond length remains relatively constant within this deviation.

The fact that there is a volumetric expansion can be attributed to the ME coupling between the in plane Ru ions; such that the coupling causes the change in separation of the Ru ions within the a - b plane and out of necessity, to keep the crystal symmetry, changing the c lattice parameter as well. In addition to this superexchange dominating the exchange interaction further supports ME coupling between intralayer Ru ions causing the expansion in the c dimension as well as for the a dimension, as not only does the c parameter have to change in order to maintain the symmetry of the lattice but it would also have to change in response to the increase in the a - b plane to maintain the most favourable bond lengths and angles between the Ru and O ions, as previously discussed.

Another effect that could be contributing to the observed magnetostriction may come from the magneto-volume effects associated with moments in the itinerant electrons within the conduction band or the d orbital electrons in general [33, 92]. Previous susceptibility measurements in the literature [41, 42] have suggested the coexistence of itinerant and localised electrons. In addition to theoretical studies which suggest

molecular orbitals in the electronic structure lead to electrons being localised to a given Ru₆ hexagon but delocalised over the corresponding six sites [49]; supported by the results of a recent Raman spectroscopy study [51]. This volume change originates from magnetic ordering within itinerant electrons producing an increase in kinetic energy which in turn causes an expansion effect. A model derived from the Stoner model for itinerant magnetism can express the change in volume associated with the increase in kinetic energy using Eq. 3.9 [92]:

$$\frac{\Delta V}{V} = \frac{Vk}{2D\mu_B^2} \frac{\partial \ln D}{\partial \ln V} M^2 \quad (3.9)$$

Here k is the isothermal compressibility, D the electronic density of states at the Fermi energy and M is the magnetisation density.

Normally the density of states increases with an increase in volume, i.e. the derivative is positive and hence as the magnetisation increases so will the volume showing that magnetic order increases volume.

Measurements collected in zero field as the sample was cooled, after the application of a 7 T field were also collected. These data were consistent with all data discussed above. Fig. 3.20 shows the cell volume as a function of temperature in various fields including the zero field measurements collected on final cooling. Here the zero field measurements are found to show equal or greater magnetostriction than for the 7 T data. This suggests that the sample remained magnetised, as would be expected from the sample never returning to a non-magnetically ordered state, i.e. it was never heated up to its Néel temperature, $T_N = 565\text{K}$.

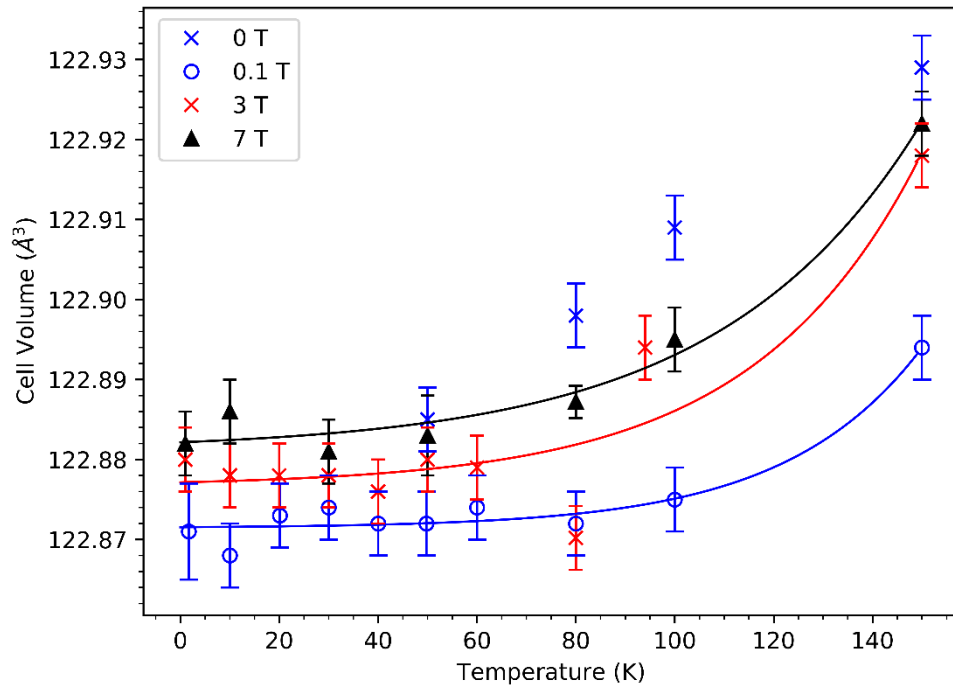


Fig. 3.20: A plot showing the cell volume of SrRu_2O_6 in various fields, including zero field measurements collected as the sample was cooled after all fields had been applied to the sample. The lines of best fit were made using exponential functions, which were fitted using a least squares fit.

To explain some of the zero field measurements having larger cell parameters than for the data collected in 7 T of field, see the measurements at 80 and 100 K in Fig.3.20. It is proposed that this is due to the measurements being collected upon cooling (rather than on heating as was the case for the rest of the data collected) as such the cell volume was already at its largest value due to thermal effects and magnetostriction and so as it then cooled the cell volume lagged behind the change in thermal energy which caused the contraction, i.e. showing hysteresis effects.

3.7 Nitrogen Contamination

Although the data discussed shows no phase transitions to have occurred over the temperatures and fields studied there were a further three peaks that were unexplained by either the magnetic or crystal structures. These peaks only appeared in a narrow temperature range from 50 K to somewhere between 60 and 80 K; as demonstrated by the 3 T data in Fig. 3.21, and only in an applied field. Furthermore, the peaks seemed to increase in intensity and split with an increase in field strength as shown in Fig. 3.22.

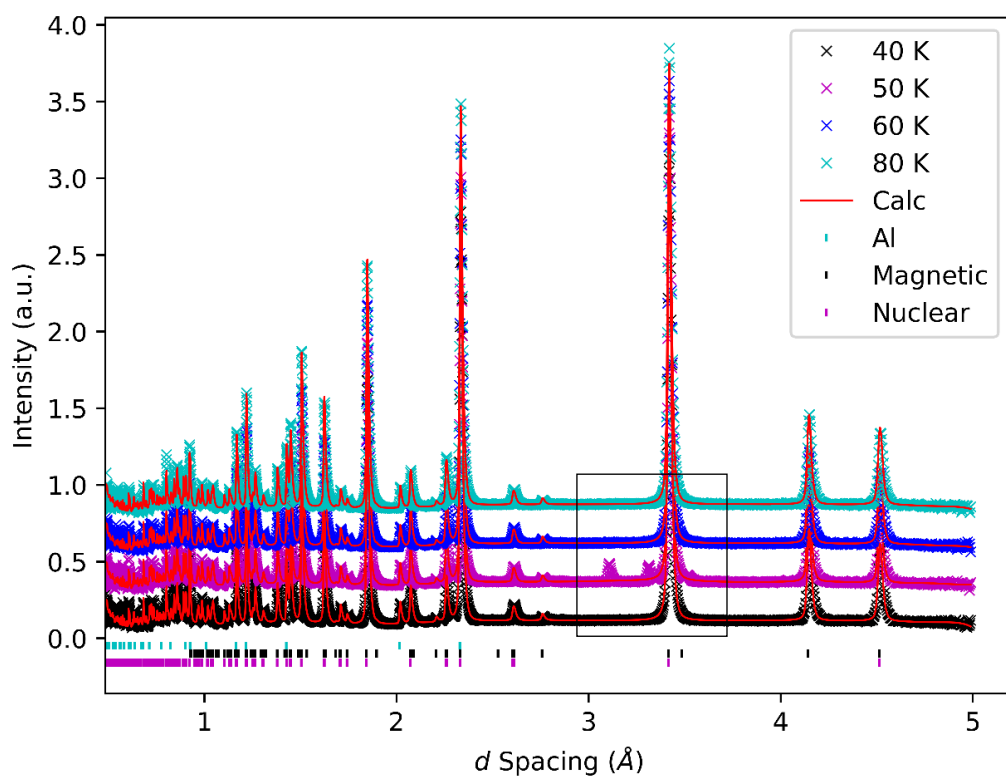


Fig. 3.21a: Waterfall plot showing the extra peaks that appear in the diffraction patterns collected between 40 and 80 K in a field of 3 T. Here increasing temperature data is plotted higher in the figure. The rectangle represents the area shown in Fig. 3.21b.

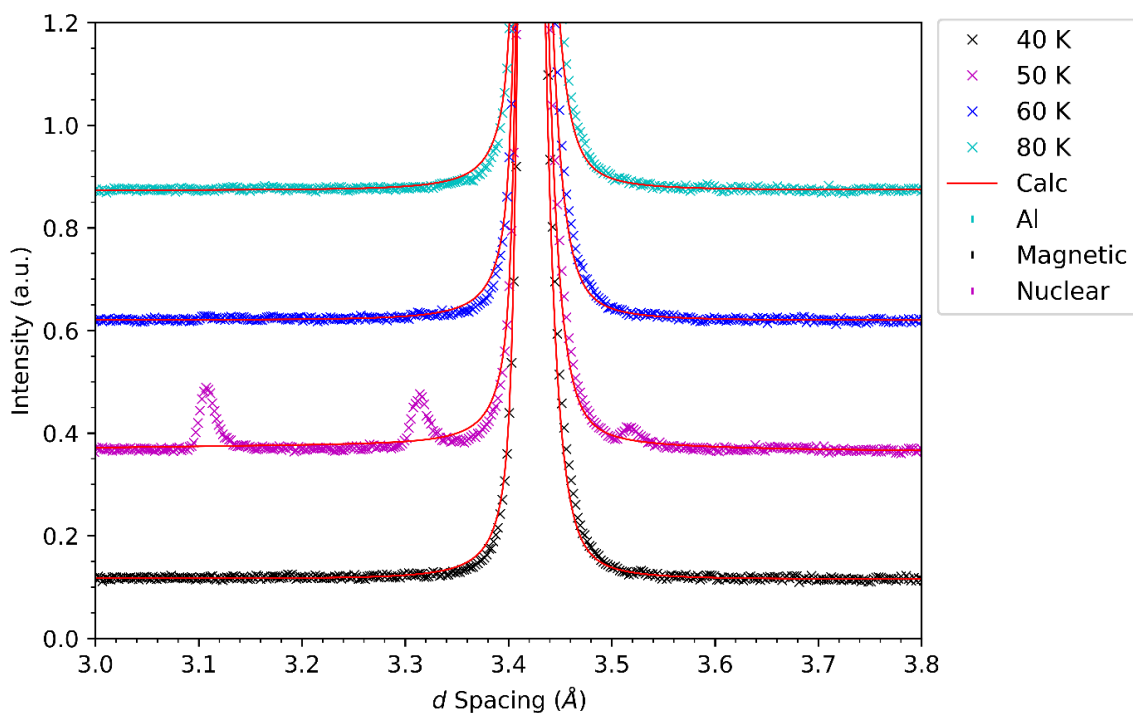


Fig. 3.21b: A magnification of the area highlighted by the rectangle in Fig. 3.21a, of a waterfall plot of the diffraction patterns collected in 3 T over a range of 40 – 80 K.

Data collected in a field of 0.1 T showed no extra peaks while the data collected in 0.5 T showed small peaks at 50 K, shown in Fig. 3.22, with peaks of slightly increased intensity appearing at 60 K (all data is given in appendix 2). For data collected at 3 T the peaks were again found at d -spacings of ≈ 3.107 , 3.312 and 3.518 Å. The evolution of the 3 T data with temperature can be seen in Fig. 3.21 and in contrast to the 0.5 T data the peaks were larger in intensity and had effectively gone by 60 K. Finally the data collected in a 7 T field shows similar behaviour, although no data was collected at 60 K for this field, by 80 K the peaks had gone, Fig.App.2.2 in appendix 2. Again the intensity of the peaks were different for the 7 and 3 T data with what at first seemed to be splitting of the peaks with a further increase in field, as shown in Fig. 3.22.

Due to the same crystal and magnetic structures fitting all of the other peaks for diffraction patterns collected at higher and lower temperatures it was suspected that this was not due to a change in either the crystal or magnetic structures. Nevertheless, to check the possibility of these peaks coming from a slight change in the magnetic structure refinements were carried out with no constraints on the x and y components of μ . Having done this GSAS was unable to find a stable solution and convergence was not achieved suggesting that a slight cant in the spins was not responsible. Similarly

the likelihood of a second magnetic phase containing ferromagnetic order was tested and was found not to give rise to these peaks. This order was found to give peaks at the same locations as the antiferromagnetic order only with increased intensity relating to certain d -spacing. Suspecting that there was never a change in the magnetic phase and being unable to refine the data with a different magnetic structure led the search for the origin of these peaks by investigating the likelihood of some form of contamination being responsible.

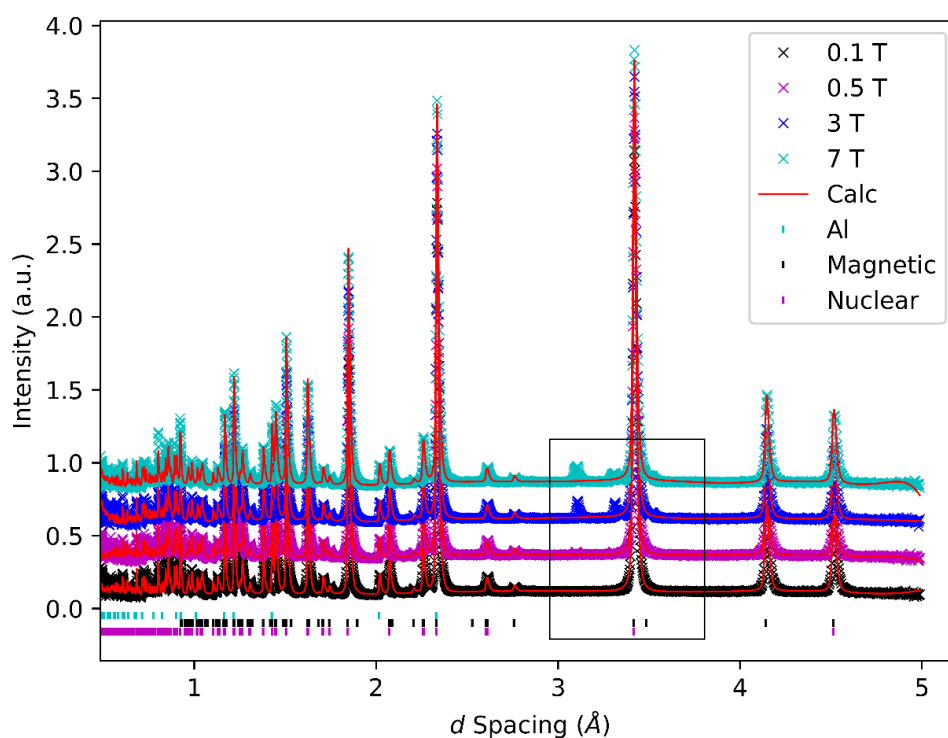


Fig. 3.22a: A Waterfall plot showing data collected at 50 K in all fields investigated, with the field increasing for data plotted higher in the figure. The rectangle represents the area shown in Fig. 22b).

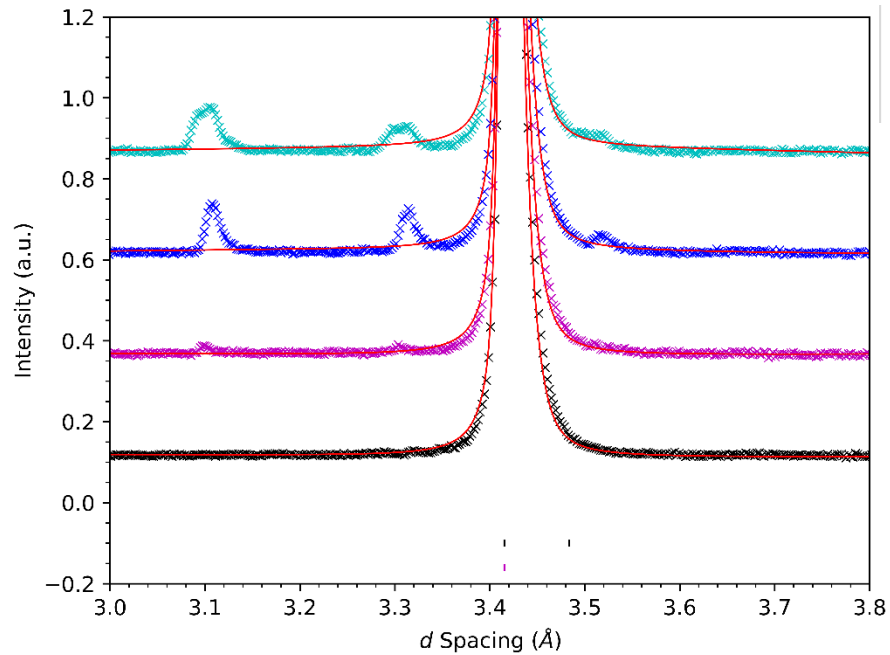


Fig. 3.22b: A magnification of the area outlined in Fig. 22a of a waterfall plot showing data collected at 50 K in all fields investigated, with the field increasing for data plotted higher in the figure.

In some cases the exchange gas being used within the sample environment can become an unwanted source of neutron scattering. Typically helium is used as an exchange gas, as it was for the experiments discussed here, due to it having a small neutron scattering cross section. However, contamination of the exchange gas with diatomic nitrogen, N_2 , can occur from air trapped in the delivery system, a small air leak in the sample environment or perhaps insufficiently pure helium in the helium reservoir [94]. Nitrogen scatters significantly more strongly than helium with solid nitrogen producing diffraction peaks comparable in size to magnetic peaks.

Additionally, the melting and boiling points of nitrogen in atmospheric pressure are 63 and 77 K, respectively and nitrogen in its solid state undergoes a phase transition from its alpha (α) phase, below, to its beta (β) phase, above, at approximately 36 K [95].

A study on the effects of nitrogen contamination in elastic neutron scattering was carried out by Chi *et al.* [94]. In this study they found that the peaks originating from nitrogen scattering only appeared when the sample was heated and not cooled, which is consistent with the experimental procedure carried out in our experiments on $SrRu_2O_6$. Peaks were found to start appearing around 30 K when the sample was

heated at a rate of 0.2 K every 20 s and at 40 K when the heating rate was increased to 0.5 K every 20 s. As the melting point was reached at ≈ 60 K the peaks were found to disappear. They also found the scattering to have a strong time dependence believed to come from the $\alpha - \beta$ phase transition taking as long as 10 h to stabilise. Hence if the warming rate is too fast the sample will not reach an equilibrium phase explaining the time dependence and why the onset temperature of the β phases increased with the rate of temperature increase.

The results reported by Chi *et al.* [94] would suggest that the onset of peaks at temperatures between 40 and 50 K is consistent with β -N₂ even though the transition temperature would suggest they should be present at 40 K. Similarly the peaks increasing with applied field could be explained by either the nitrogen present in the sample environment being redistributed due to localised heating within the cryostat as the field is increased, with more nitrogen being deposited on the sample can as the field was increased. On the other hand, and more likely, it could be explained due to a small leak which as the experiment progressed would lead to more nitrogen entering the sample environment and thus condensing on the sample can [96]. Again, this is consistent with the way the experiment was performed i.e. the data for increasing field was collected at a later time.

To further confirm whether these peaks could be due to contamination from nitrogen a fourth phase containing nitrogen was added to the refinement of the 3 T data collected at 50 K. The model used was that reported for β -N₂, at 50 K, by Streib *et al.* [97] with a hexagonal unit cell ($a = 4.036$, $b = a$, $c = 6.630$) and $P6_3/mmc$ space group.

This model was then fit to the data using a Le Bail fit, shown in Fig. 3.23, and achieved goodness-of-fit parameters of $\chi^2 = 6.209$, $R_p = 4.01\%$, and $wR_p = 4.34\%$ compared to those prior to the nitrogen being added of $\chi^2 = 10.74$, $R_p = 5.06\%$, $wR_p = 5.70\%$. During the refinement the a and c lattice parameters only changed by 0.5 and 0.2 % respectively, suggesting that nitrogen is very likely to be responsible for these peaks.

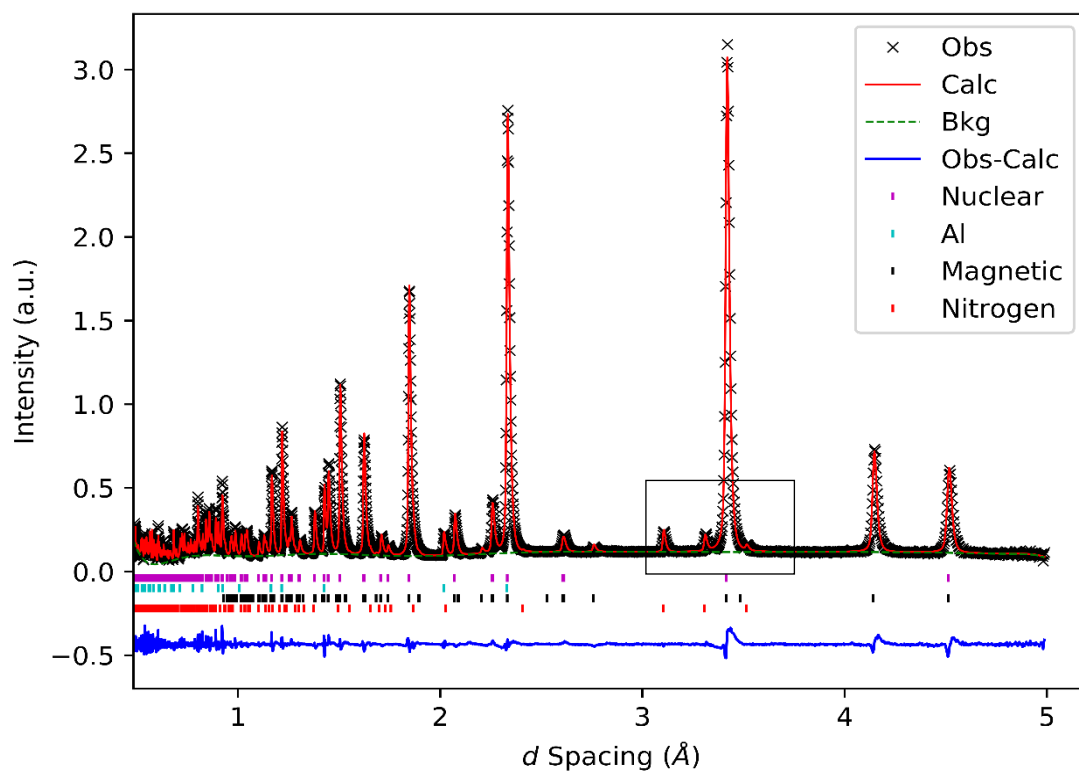


Fig. 3.23a: *Le Bail* refinement of the data collected in a field of 3 T at 50 K with a nitrogen phase added. $\chi^2 = 6.209$, $R_p = 4.01\%$, and $wR_p = 4.34\%$.

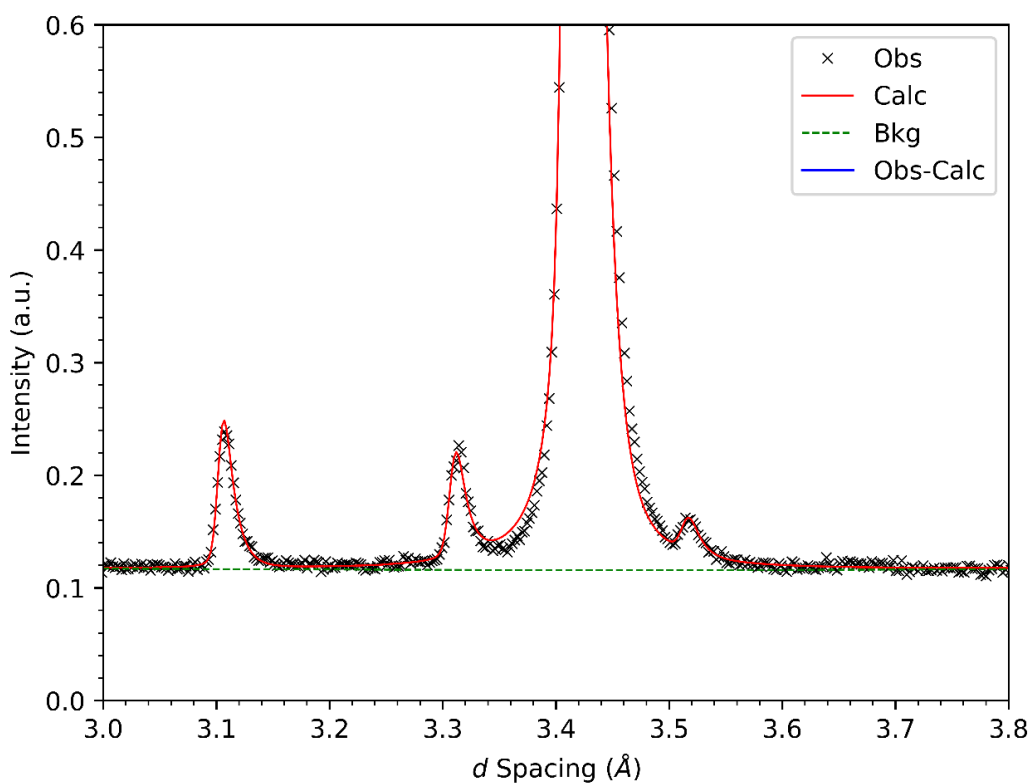


Fig. 3.23b: The region of the *Le Bail* refinement of the data collected in a field of 3 T at 50 K containing the unfit peaks, outlined in Fig. 3.23a, fitted with a nitrogen phase.

The same model and procedure was applied to the 0.5 T data with the first peak being fit, Fig. 3.24, by the nitrogen model with lattice parameters only differing by 0.01 and 0.4 %. However, there was some difficulty fitting the second smaller peak.

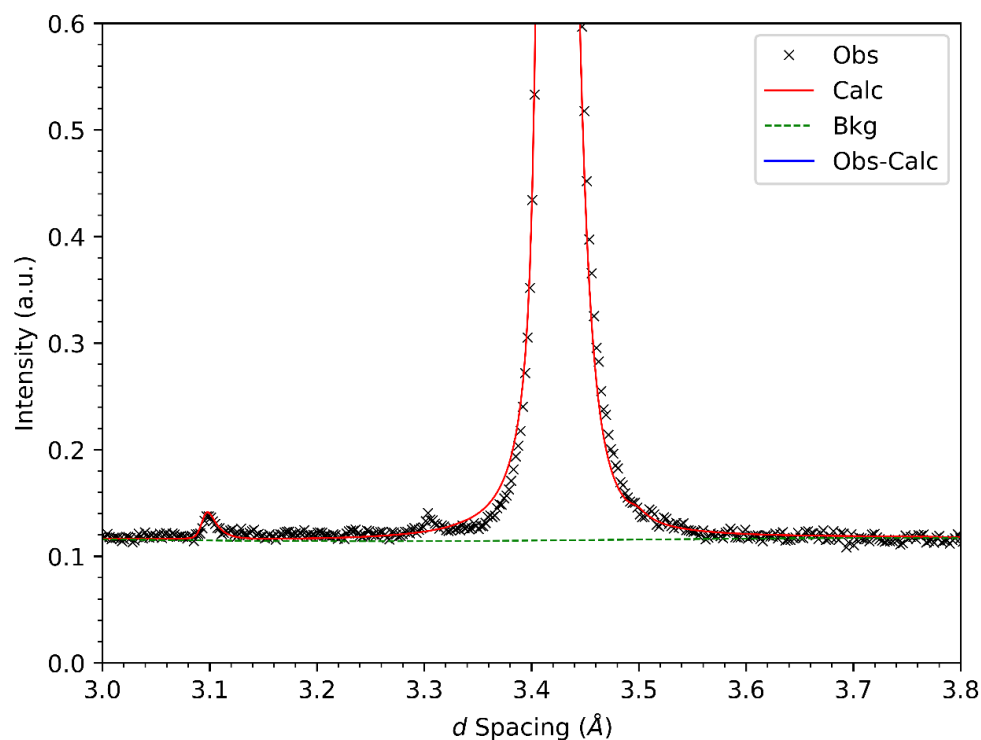


Fig. 3.24: The region of the refinement of the data collected in a field of 0.5 T at 50 K, containing the unfit peaks, fitted with a nitrogen phase. The overall goodness-of-fit parameters are: $\chi^2 = 6.811$, $R_p = 4.48\%$ and $wR_p = 4.57\%$. The full fit can be found in the appendiceis in Fig.App.2.1.

On the other, hand the 7 T data was not so easily fit. Refinement of a single phase could not explain the split peak. However, aplying a second nitrogen phase, i.e. a fith phase, also using a Le Bail fit it was possible to fit the data as shown in Fig. 3.25. Clearly this is not a perfect fit, perhaps partly due to their being too much correlation between the two nitrogen phases and peaks causing issues with the refinement process, such as not being able to succefully refine the peak shape. However, an even more likely explanation is that if the nitrogen condensed in a thin film then it is unlikely that it would produce a powder-like polycrystalline phase [96] leading to slightly different relative intensities between peaks and hence an imperfect fit, as seen in Fig. 3.25.

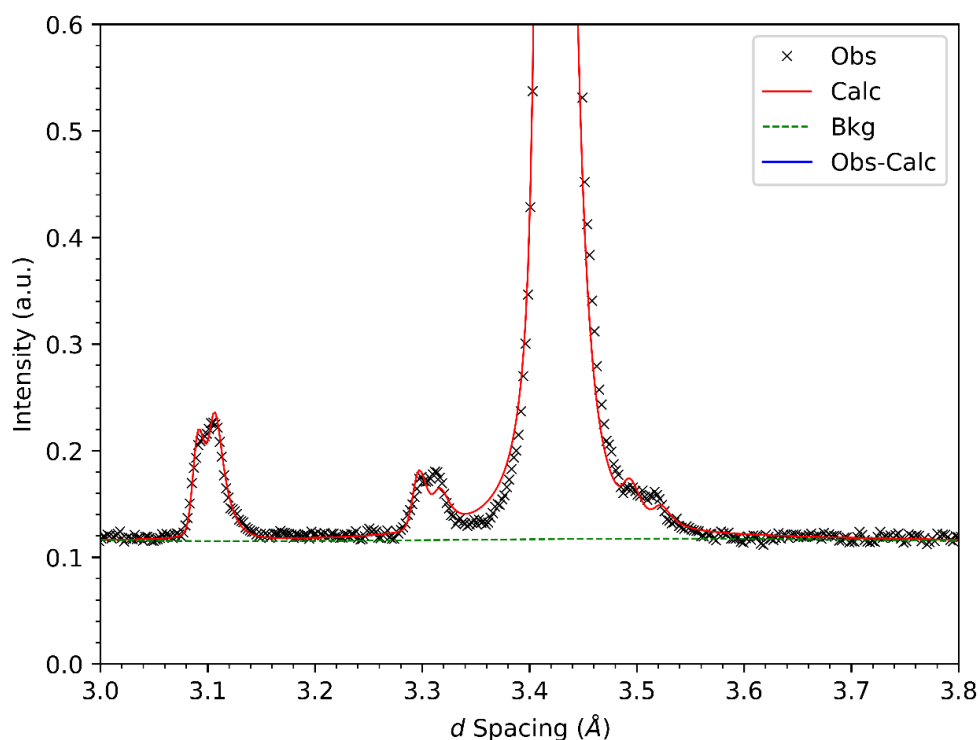


Fig. 3.25: The region of the refinement of the data, collected in a field of 7 T at 50 K, containing the unfit peaks, fitted with two nitrogen phase. The overall goodness-of-fit parameters are: $\chi^2 = 6.487$, $R_p = 4.17\%$, and $wR_p = 4.44\%$. The full fit can be found in the appendiceis in Fig.App.2.2.

Although not a perfect fit Fig. 3.25 shows how two nitrogen phases with slightly different parameters, differing from the original model by 0.14 and 0.04 % and 0.7 and 0.7 %, could explain the splitting of the peaks. It is not suggested that there were two phases of nitrogen with different lattice parameters, although this could be a possibility, but instead that there were two contaminant layers or volumes of solid nitrogen in different positions relative to the sample. There could be, for example, one condensed on the sample can and one condensed on the inner vacuum chamber wall. Therefore the instrument parameters, zero, difc, difa etc. would not strictly apply to the nitrogen phase that is off-centre relative to the sample position determined by the calibration (which provides the instrument parameters) resulting in the differences in peak position. Thus the need for different lattice parameters could be due to the difference between the calibrated instrument parameters and the true parameters for these off-centre phases. This splitting of peaks due to two layers of a material in significantly different positions is a well known phenomena [96]. See Appendix 2 for plots showing the full profiles of each refinement.

Chapter 4: Conclusions

The incredibly high antiferromagnetic ordering temperature of SrRu_2O_6 , $T_N = 565$ K, makes it very interesting as the strong correlations that give rise to this large ordering temperature may lead to further interesting properties. Similarly, fluctuations near the AFM boundary, believed to mediate Cooper pairing in cuprate superconductors, [43, 44] furthers the interest in SrRu_2O_6 for its potential to be a possible unconventional superconductor [43].

A magnetic field dependent neutron powder diffraction study was carried out along with complementary magnetic susceptibility, X-ray diffraction, and scanning electron microscopy combined with Energy Dispersive X-ray Spectroscopy measurements to investigate the crystal structure and magnetic properties of SrRu_2O_6 in an applied magnetic field.

Susceptibility measurements show a divergence between the ZFC and FC data collected in a field of 0.1 T, characteristic of either weak ferromagnetic ordering or spin glass-like behaviour [39, 79]. Hysteresis measurements did not show any clear hysteresis suggesting that there is no ferromagnetic ordering and similarly that it is unlikely that there is spin glass order. A possible explanation for the observed divergence comes from the plate like morphology of the SrRu_2O_6 crystallites. It is likely that due to the large surface area to volume ratio of the platelets, there will be a significant number of uncompensated surface spins, which can appear as disordered i.e. glass-like [6, 80, 81]

Neutron powder diffraction and powder X-ray diffraction experiments confirm the crystal structure of SrRu_2O_6 to have a hexagonal unit cell, with a space group of $P\bar{3}1m$ ($a = b = 5.20142(5)$ Å and $c = 5.23124(7)$ Å, at room temperature in zero field). No structural transitions were found to occur over the entire range of temperatures and fields studied. However, an anisotropic thermal expansion was observed in which the c lattice parameter increased while the a lattice parameter decreased. This is most likely due to magnetoelastic (ME) coupling between the intralayer Ru ions [46].

Further to this, the magnetic structure also did not change over the temperature and fields studied and was found to comprise of Ru ions with magnetic moments of $1.47(2) \mu_B$ directed along the c axis and antiferromagnetically ordered both within and among the planes of Ru ions; an order equivalent to G-type for a cubic cell. This moment is under half the value one would expect to measure of $3 \mu_B$ suggesting that there is a large amount of covalence between the Ru and O ions causing a distribution of the moment.

In addition to the thermal expansion a positive magnetostriction in the order of $\lambda \sim 10^{-5}$ was found to occur with all lattice parameters increasing with an increase in applied magnetic field. This provides further evidence for there being strong ME coupling between the intralayer Ru ions coming from exchange striction and a potential contribution from itinerant electrons. It is also thought that the exchange interactions that give rise to the exchange striction are dominated by super exchange interactions between Ru ions mediated by the O ions due to the large amounts of covalence observed. In further support of this is the fact that the Ru-O-Ru bond angle and Ru-O bond length were found to remain relatively constant, within error, as the temperature and field were increased. This is because superexchange, as the dominant interaction, would cause the Ru and O ions to maintain the most favourable separation and angle for the super exchange interaction.

4.1: Future Research

Future work could include AC susceptibility measurements to further unequivocally confirm whether there is or is not any glassy-behaviour causing the divergence between the ZFC and FC DC susceptibility data at low field. This would further confirm whether or not the surface area-volume effects of uncompensated surface spins are responsible. Potentially, further investigation into whether doping the material, perhaps with another transition metal ion such as Ir, could lead to further interesting properties to emerge [12] could also be performed. It is well known that doping effects the magnetism of a sample as well as having been found to induce superconductivity in cuprates [42, 43, 98].

Bibliography:

1. G. Cao and L. E. DeLong, *Frontiers of 4d and 5d Transition Metal Oxides*, (World Scientific Publishing Co. Pte. Ltd., Singapore, 2013).
2. S. Blundell, *Magnetism in condensed matter*, (Oxford University Press Inc., New York, 2001).
3. B. Normand, *Contemporary Physics* **50**, 533 (2009).
4. A. Lauchli, F. Mila, and K. Penc, *Phys. Rev. Lett.* **97**, 087205 (2006).
5. J. A. Mydosh, *Rep. Prog. Phys.* **78**, 052501 (2015).
6. K. Binder and A. P. Young, *Rev. Mod. Phys.* **58**, 802 (1986).
7. R. L. Fagaly, *Rev. Sci. Instrum.* **77**, 101101 (2006).
8. A. P. Mackenzie and Y. Maeno, *Rev. Mod. Phys.* **75**, 657 (2003).
9. K. Maki, T. Tsuneto, *Prog. Theor. Exp. Phys.* **31**, 945 (1964).
10. A. Nag, S. Bhowal, M. Moretti Sala, A. Efimenko, I. Dasgupta and Sugata Ray, *Phys. Rev. Lett.* **123**, 017201 (2019).
11. A. Nag, S. Bhowal, F. Bert, A. D. Hillier, M. Itoh, I. Carlomagno, C. Meneghini, T. Sarkar, R. Mathieu, I. Dasgupta, and S. Ray, *Phys. Rev. B* **97**, 064408 (2018).
12. A. Paramekanti, D. J. Singh, Bo Yuan, D. Casa, Y.-J. Kim and A. D. Christianso, *Phys. Rev. B* **97**, 235119 (2018).
13. S. Yonezawa, Y. Muraoka, Y. Matsushita and Z. Hiroi, *J. Phys. Conds. Matt.* **16**, 9 (2004).
14. Z. Hiroi, S. Yonezawa and Y. Muraoka, *J. Phys. Soc. Jpn.* **73**, 1651 (2004).
15. A. Koda, W. Higemoto, K. Ohishi, S. R. Saha, R. Kadono, S. Yonezawa, Y. Muraoka and Z. Hiroi, *J. Phys. Soc. Jpn.* **74**, 1678 (2005).
16. R. Prozorov and V. G. Kogan, *Rep. Prog. Phys.* **74**, 124505 (2011).
17. Vladimir P. Mineev and Vincent P. Michal, *J. Phys. Soc. Jpn.* **81**, 093701 (2012).
18. T. McConville and B. Serin, *Phys. Rev.* **140**, A1169 (1965).
19. Y. Maeno, H. Hashimoto, K. Yoshida, S. Nishizaki, T. Fujita, J. G. Bednorz, F. Lichtenberg, *Nature* **372**, 532 (1994).
20. Y. Maeno, *Superconductivity of Layered Perovskite Sr₂RuO₄* in H. Hayakawa and Y. Enomoto (eds) *Advances in Superconductivity VIII*, (Springer Japan, Tokyo, 1996).

21. Q. Huang, J. W. Lynn, R. W. Erwin, J. Jarupatrakorn and R. J. Cava, *Phys. Rev. B* 58, 8515 (1998).
22. S. Reich, Y. Tsabba and G. Cao, *J. Magn. Magn. Mater.* 202, 119 (1999).
23. K. Ishida, H. Mukuda, Y. Kitaoka, K. Asayama, Z. Q. Mao, Y. Mori and Y. Maeno, *Nature* 396, 658 (1998).
24. P. W. Anderson, *Phys. Rev. Lett.* 3, 325 (1959).
25. A. A. Abrikosov and L. P. Gor'kov, *Sov. Phys. JETP* 12, 1243 (1960).
26. H. Shaked, J. D. Jorgensen, O. Chmaissem, S. Ikeda and Y. Maeno, *J. Solid State Chem.* 154, 361 (2000).
27. I. Hase and Y. Nishihara, *J. Phys. Soc. Jpn.* 66, 3517 (1997).
28. S. Ikeda, Y. Maeno and T. Fujita, *Phys. Rev. B* 57, 978 (1998).
29. S. A. Grigera, S. R. Perry, A. J. Schofield, M. Chiao, S. R. Julian, G. G. Lonzarich, S. I. Ikeda, Y. Maeno, A. J. Millis, A. P. Mackenzie, *Science* 294, 329 (2001).
30. A. Tamai, M. P. Allan, J. F. Mercure, W. Meevasana, R. Dunkel, D. H. Lu, R. S. Perry, A. P. Mackenzie, D. J. Singh, Z.-X. Shen, and F. Baumberger, *Phys. Rev. Lett.* 101, 026407 (2008).
31. C. Lester, S. Ramos, R. S. Perry, T. P. Croft, R. I. Bewley, T. Guidi, P. Manuel, D. D. Khalyavin, E. M. Forgan, S. M. Hayden, *Nature Materials* 14, 373 (2015).
32. E. Stryjewski and N. Giordano, *Adv. Phys.* 26, 487 (1977).
33. M. Shimizu, *J. Phys* 43, 155 (1982).
34. A. P. Mackenzie, J. A. N. Bruin, R. A. Borzi, A. W. Rost and S. A. Grigera, *Physica C* 481, 207 (2012).
35. S. A. Grigera, *Science* 306, 1154 (2004).
36. D. Hüser, L. E. Wenger, A. J. van Duynveldt and J. A. Mydosh, *Phys. Rev. B* 27, 3100 (1983).
37. J. M. Longo, P. M. Raccah, and J. B. Goodenough, *J. Appl. Phys.* 39, 1327 (1968).
38. L. J. Vera Stimpson, J. M. Powell, G. B. G. Stenning, M. Jura, and D. C. Arnold, *Phys. Rev. B* 98, 174429 (2018).
39. S. Lin, D. F. Shao, J. C. Lin, L. Zu, X. C. Kan, B. S. Wang, Y. N. Huang, W. H. Song, W. J. Lu, P. Tong and Y. P. Sun, *J. Mater. Chem. C* 3, 5683 (2015).
40. A. M. Larson, P. Moetakef, K. Gaskell, C. M. Brown, G. King, and E. E. Rodriguez, *Chem. Mater.* 27, 515 (2015).

41. C. I. Hiley, M. R. Lees, J. M. Fisher, D. Thompsett, S. Agrestini, R. I. Smith, and R. I. Walton, *Angew. Chem. Int. Ed.* 53, 4423 (2014).
42. W. Tian, C. Svoboda, M. Ochi, M. Matsuda, H. B. Cao, J.-G. Cheng, B. C. Sales, D. G. Mandrus, R. Arita, N. Trivedi, and J.-Q. Yan, *Phys. Rev. B* 92, 100404 (2015).
43. D. Wang, W.-S. Wang and Q.-H. Wang, *Phys. Rev. B* 92, 075112 (2015).
44. J. M. Santiago, C-L Huang and E. Morosan, *J. Phys. Condens. Matter* 29, 373002 (2017).
45. D. J. Singh, *Phys. Rev. B* 91, 214420 (2015).
46. C. I. Hiley, D. O. Scanlon, A. A. Sokol, S. M. Woodley, A. M. Ganose, S. Sangiao, J. M. De Teresa, P. Manuel, D. D. Khalyavin, M. Walker, M. R. Lees, and R. I. Walton, *Phys. Rev. B* 92, 104413 (2015).
47. J. B. Goodenough, *Magnetism and the Chemical Bond*, (John Wiley and Sons, New York, 1963).
48. Q. Si, R. Yu and E. Abrahams, *Nature Rev. Mater.* 1, 16017 (2016).
49. S. Streltsov, I.I. Mazin and K. Fogevtsova, *Pyhs. Rev. B* 92, 134408 (2015).
50. S. Okamoto, M. Ochi, R. Arita, J. Yan , N. Trivdei, *Sci. Rep.* 7, 11742 (2017).
51. Yu. S. Ponosov, E. V. Komleva, D. A. Zamyatin, R. I. Walton and S. V. Streltsov, *Phys. Rev. B* 99, 085103 (2019).
52. H. Suzuki, H. Gretarsson, H. Ishikawa, K. Ueda, Z. Yang, H. Liu, H. Kim, D. Kukusta, A. Yaresko, M. Minola, J. A. Sears, S. Francoual, H.-C. Wille, J. Nuss, H. Takagi, B. J. Kim, G. Khaliullin, H. Yavaş & B. Keimer, *Nature Materials* 18, 563 (2019).
53. N. W. Ashcroft, N. D. Mermin, *Solid State Physics, International Edition*, (Holt, Rinehart and Watson, New York, 1976).
54. J. R. Hook, H. E. Hall, *Solid State Physics, 2nd edition*, (wiley and sons, Sussex England, 1991).
55. A. R. West, *Solid State Chemistry and its Applications, 2nd student edition*, (John Wiley and Sons Ltd, Hoboken, 2014).
56. B. D. Cullity, S. R. Stock, *Elements of X-ray Diffraction, Third Edition*. (Prentice Hall, New Jersey, 2001).

57. N. Qureshi, Neutron Diffraction [Online], 2015,
<https://www.oxfordneutronschool.org/2015/Lectures/Qureshi-Neutron%20Diffraction.pdf> [May 2019].
58. D. Fruchart in Encyclopedia of Materials: Science and Technology: Permanent Magnet Materials: Neutron Experiments, (Elsevier Ltd., unknown, 2001).
59. J. Cui, Q. Huang and B. H. Toby, Powder Diffr. **21**, 71 (2006).
60. J. M. A. Reichelt and A. L. Rodgers, Nucl. Instrum. Methods **45**, 245 (1966).
61. H. M. Rietveld, J. Appl. Cryst. **2**, 65 (1969).
62. V. K. Pecharsky and P. Y. Zavalij, Fundamentals of Powder Diffraction and Structural Characterization of Materials (Springer Science + Business Media Inc, New York, 2003), Chapter 7.
63. R. A. Young. The Rietveld Method, (Oxford University Press, New York, 1993).
64. B. H. Toby, Powder Diffr. **21**, 67 (2006).
65. D. Duxbury, D. Khalyavin, P. Manuel, D. Raspino, N. Rhodes, E. Schooneveld and E. Spilla, J. Inst. 9, C12008 (2014).
66. S. N. Ahmed in Physics and Engineering of Radiation Detection (Second Edition), Properties and sources of radiation, (Elsevier Inc., unknown, 2015).
67. A.C. Larson and R.B. Von Dreele, General Structure Analysis System (GSAS), Los Alamos National Laboratory Report LAUR, 86 (2004).
68. B. H. Toby, J. Appl. Cryst. **34**, 210 (2001).
69. S. A. Speakman, Basics of X-Ray Powder Diffraction, [Online], Unknown,
<http://prism.mit.edu/xray/Basics%20of%20X-Ray%20Powder%20Diffraction.pdf>, [Jul. 2019].
70. B. H. Toby, GSAS Parameters & Controls What to Refine when? (Refinement Recipes) [online], Unknown, <https://www.aps.anl.gov/sites/default/files/APS-Uploads/XSD/Powder-Diffraction-Crystallography/5ParametersRecipes.pdf>, [Jul. 2019].
71. Th. Hahn, International Tables for Crystallography volume A Space Group Symmetry, 5th edition, (Springer, The Netherlands, 2005).
72. N. G. Parkinson, P. D. Hatton, J. A. K. Howard, C Ritter, F. Z. Chien and M.-K. Wu, J. Mater. Chem. **13**, 1468 (2003).

73. J. Cui, Q. Huang and B. H. Toby, Fitting Nuclear and Magnetic Scattering in GSAS with a Pmmm Nuclear Phase and a P1 Magnetic Phase, [Online], 2006, <https://www.ncnr.nist.gov/xtal/software/magtut/pmmm-p1.html>, [Jul. 2019].
74. A. Le Bail, Powder Diffr. **20**, 316 (2005).
75. V. K. Peterson, Powder Diffr. **20**, 14 (2005).
76. P. R. Thornton, Scanning Electron Microscopy Applications to materials and Device Science, (Chapman and Hall Ltd, London, 1968).
77. J. I. Goldstein, D. E. Newbury, P. Echlin, D. C. Joy, C. Fiori, E. Lifshin, Scanning Electron Microscopy and X-Ray Microanalysis A Text for Biologists, Materials Scientists, and Geologists, (Plenum Press, New York, 1981).
78. O. P. Choudhary and P. Malik, Int. J. Curr, Microbiol. App. Sci. **6**, 1877 (2017).
79. H. Sato, M. Soma, J. Magn. Mater. **310**, 1517 (2007).
80. D. C. Arnold, O. Kazakova, G. Audoit, J. M. Tobin, J. S. Kulkarni, S. Nikitenko, M. A. Morris and J. D. Holmes, ChemPhysChem **8**, 1694 (2007).
81. L. J. Vera Stimpson, S. Ramos, G. B. G. Stenning, M. Jura, S. Parry, G. Cibin and D. C. Arnold, Dalton Trans. **46**, 14130 (2017).
82. I. F. Bailey, Z. Kristallogr. **218**, 84 (2003).
83. Unknown, 10 T Magnet, [Online], Unknown, <https://www.isis.stfc.ac.uk/Pages/10T-Magnet.aspx>, [Feb. 2019].
84. B. Predel and K. Huelse, Zeitschrift fuer Metallkunde **69**, 690 (1978).
85. A. Tabei and S. Y. Liang in Applied Mechanics, Mechatronics and intelligent Systems, Effects of Machining on the Microstructure of Aluminum Alloy 7075, Edited by Shihong Qin and Xiaolong Li, (World Scientific Publishing Co. Pte. Ltd., Singapore, 2016).
86. B. N. Figgis and J. Lewis in Progresses in Inorganic Chemistry, Volume 6: The Magnetic Properties of Transition Metal Complexes, Edited by F. Albert Cotton, (John Wiley and Sons Inc., unknown, 1964).
87. Fabio Orlandi (Private Communication) (2019).
88. E. R. Callen and H. B. Callen, Phys. Rev. **129**, 578 (1963).
89. X. Z. Lu, Xifan Wu and H. J. Xiang, Phys. Rev. B **91**, 100405 (2015).
90. A. B. Shick, D. L. Novikov, and A. J. Freeman, J. Appl. Phys. **83**, 7258 (1998).

91. N. B. Ekreem, A. G. Olabi, T. Prescott, A. Rafferty, M. S. J. Hashmi, *Journal of Materials Processing Technology* **191**, 96 (2007).
92. M. Doerr , M. Rotter and A. Lindbaum, *Adv. Phys.* **54**, 1 (2005).
93. J. Kanamori, *J. Phys. Chem. Solids* **10**, 87 (1959).
94. Songxue Chi et al 2011 *Meas. Sci. Technol.* **22**, 047001 (2011).
95. T. A. Scott, *Phys. Rep.* **27** 89 (1972).
96. Alexandra Gibbs (Private communication) (2019).
97. W. E. Streib, T. H. Jordan, and W. N. Lipscomb, *J. Chem. Phys.* **37**, 2962 (1962).
98. P. Dai, J. Hu and E. Dagotto, *Nature Physics* **8**, 709 (2012).

Appendices

Appendix 1:	100
-------------------	-----

This appendix contains plotted refinements for all the sets of NPD data, which were not included in the results section. These are followed by tables containing full refinement parameters as well as tables containing the bond lengths and angles for the SrRu₂O₆ phase. Refinements and tables are ordered by the fields and temperatures in which the data was collected. Note that the refinement parameters for the nitrogen phases are in a separate table.

Plotted Refinements	100
----------------------------------	-----

0.1 T, ZFC	100
------------------	-----

1 – 30 K	100
----------------	-----

40 – 60 K	101
-----------------	-----

80 - 100 K	102
------------------	-----

0.1 T, FC	103
-----------------	-----

1 – 20 K	103
----------------	-----

30 – 50 K	104
-----------------	-----

60 - 80 K	105
-----------------	-----

0.5 T, ZFC	106
------------------	-----

1 – 20 K	106
----------------	-----

30 – 50 K	107
-----------------	-----

60 - 100 K	108
------------------	-----

150 K	109
-------------	-----

3 T, ZFC	110
----------------	-----

1 – 30 K	110
----------------	-----

40 – 60 K	111
-----------------	-----

80 - 94 K	112
-----------------	-----

7 T, ZFC	113
----------------	-----

1 – 50 K	113
80 – 100 K	114
0 T, data collected as cooled	115
150 - 80K.....	115
50 K	116
Refinement Parameters	117
0.1 T, ZFC	117
0.1 T, FC.....	118
0.5 T, ZFC	119
3 T, ZFC.....	120
7 T, ZFC.....	121
0 T, data collected as cooled	122
Bond Lengths and Angles:	123
0.1 T, ZFC and 0.1 T, FC	123
0.5 T, ZFC and 3 T, ZFC	124
7 T, ZFC and 0 T, data collected as cooled	125
Parameters for the nitrogen phases	126
Appendix 2:	127
<p>This appendix contains the calculated values for magnetostriction, for each field and temperature. In addition to this, full detailed, plots showing the temperature evolution of the nitrogen peaks in the 0.5 and 7 T data are also included.</p>	
Table of values for magnetostriction	127
Nitrogen peaks in 0.5 T	128
Nitrogen peaks in 7 T	129

Appendix 1

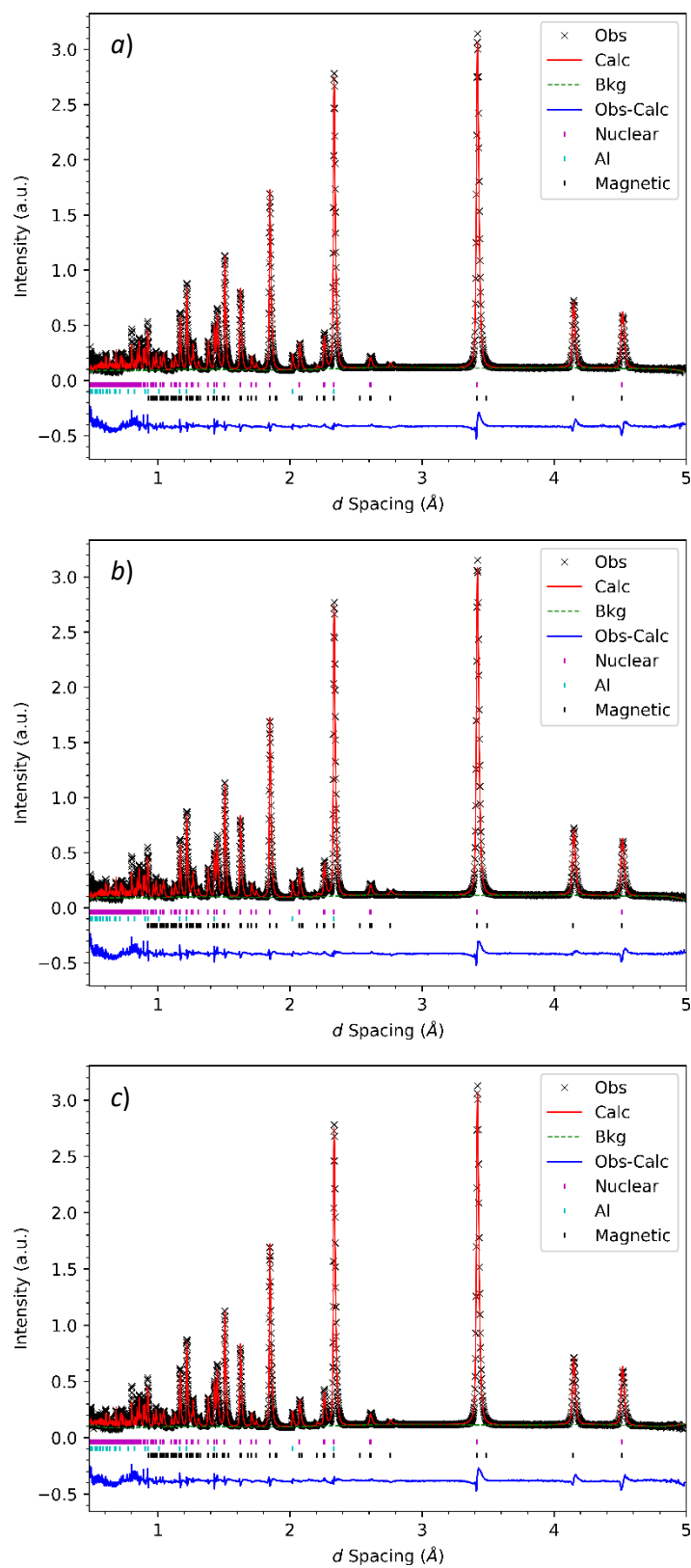


Fig.App.1.1: Rietveld refinements of neutron powder diffraction data collected in an applied magnetic field of 0.1 T, in zero field cooled conditions at: a) 1 K, b) 10 K, c) 30 K.

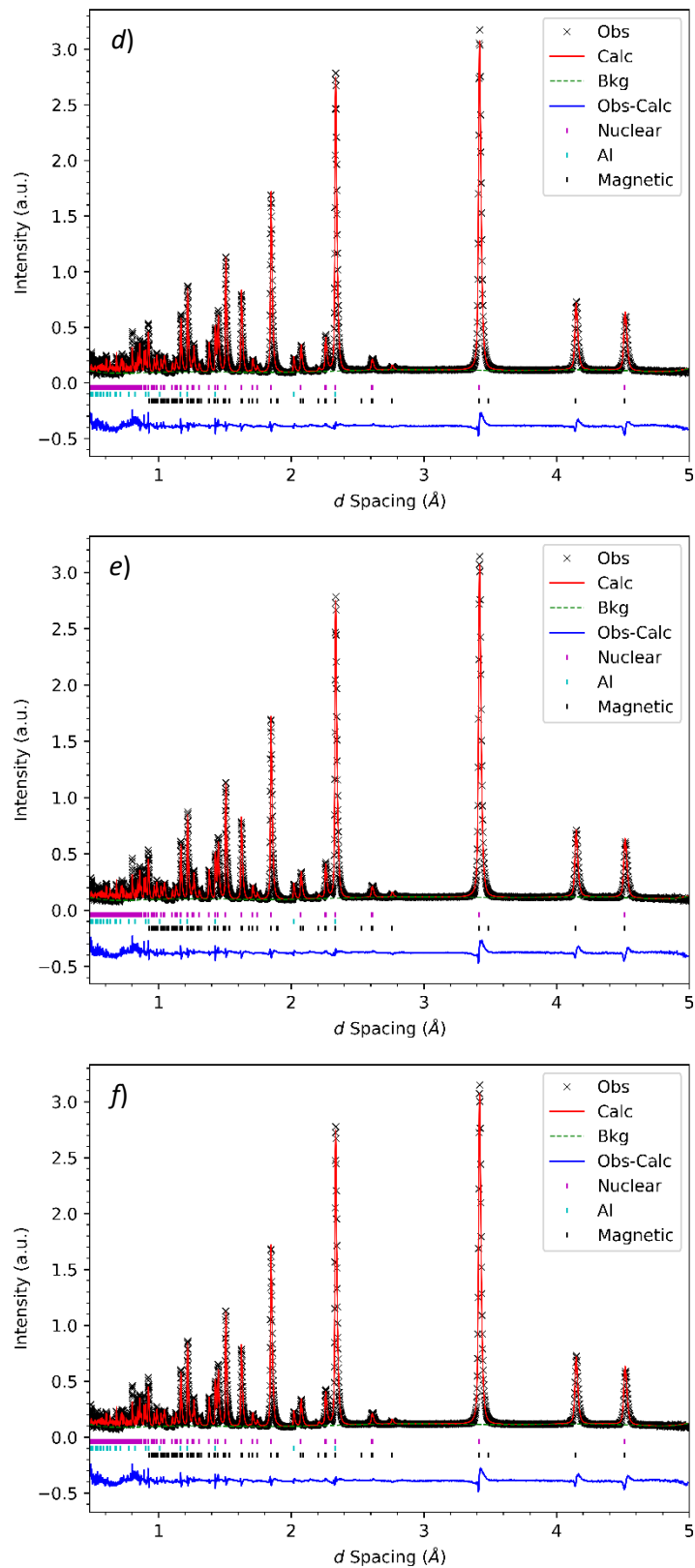


Fig.App.1.1: Rietveld refinements of neutron powder diffraction data collected in an applied magnetic field of 0.1 T, in zero field cooled conditions at: d) 40 K, e) 50 K, f) 60 K.

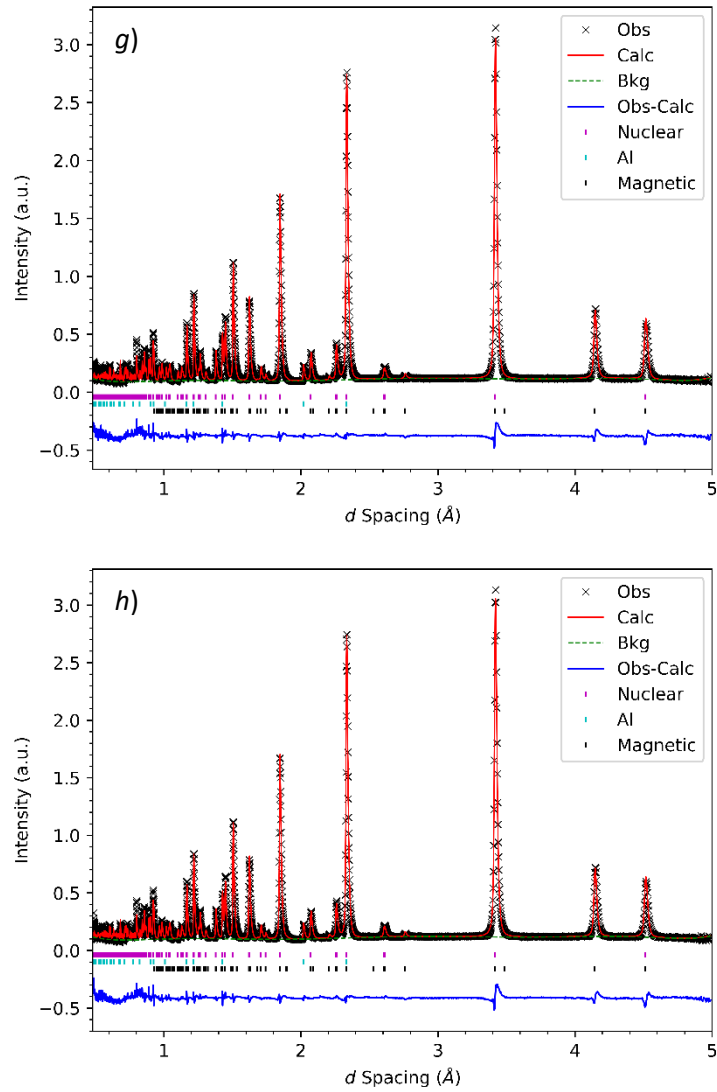


Fig.App.1.1: Rietveld refinements of neutron powder diffraction data collected in an applied magnetic field of 0.1 T, in zero field cooled conditions at: g) 80 K, h) 100 K.

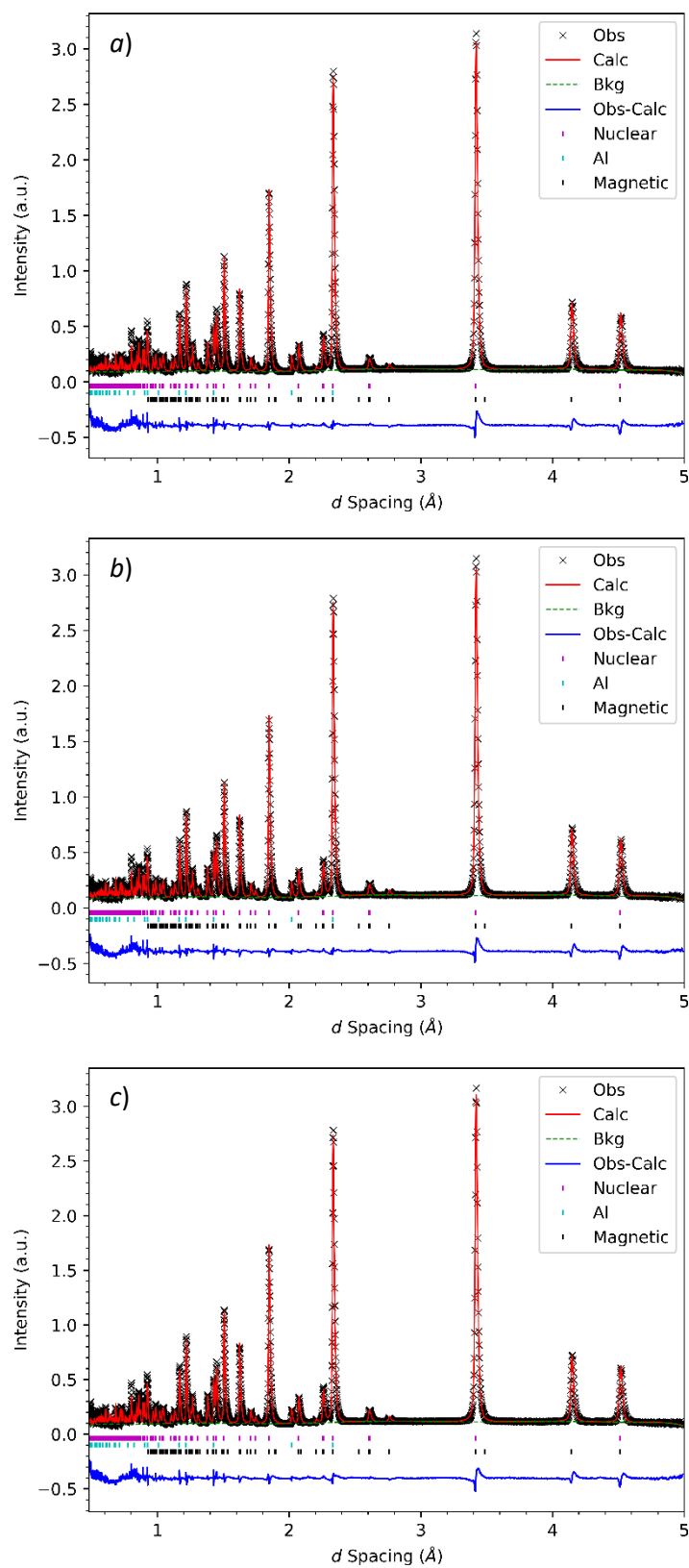


Fig.App.1.2: Rietveld refinements of neutron powder diffraction data collected in an applied magnetic field of 0.1 T, in field cooled conditions at: a) 1 K, b) 10 K, c) 20 K.

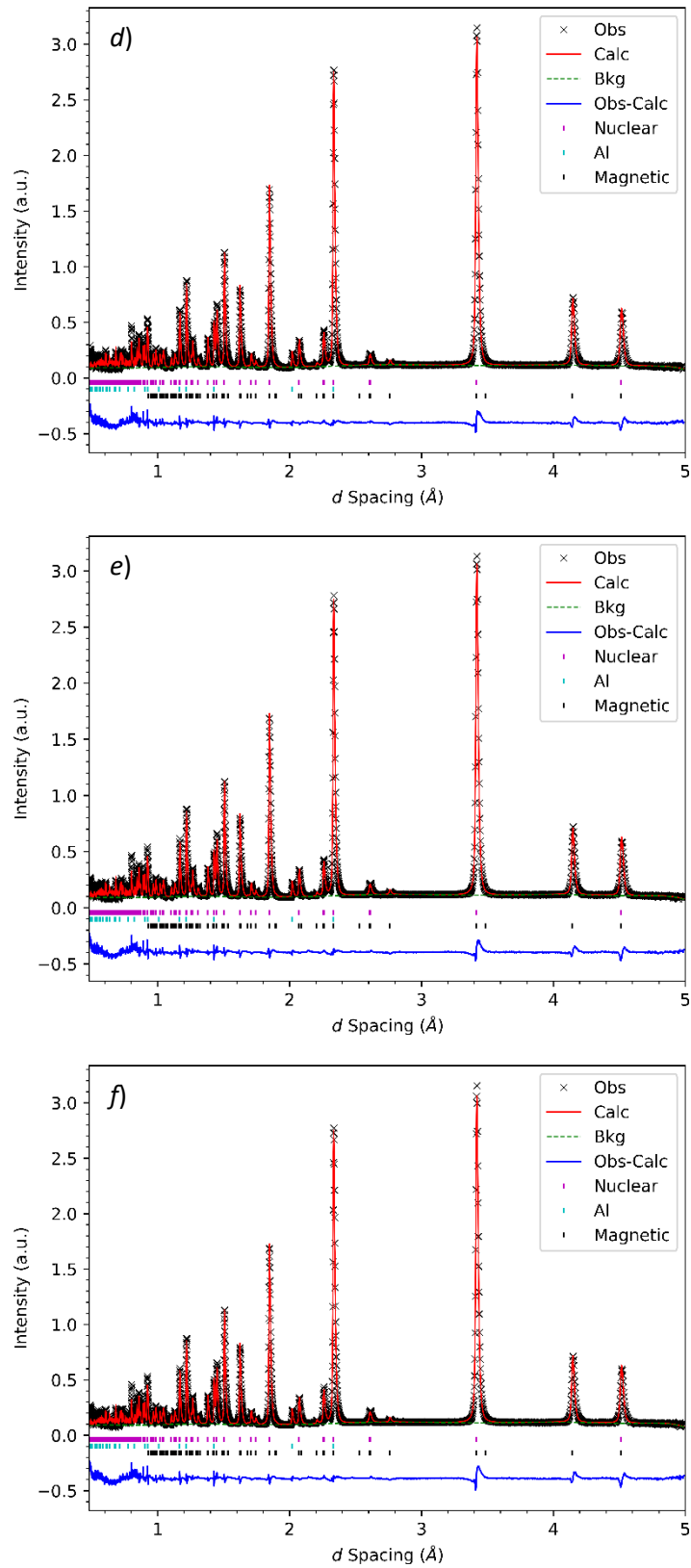


Fig.App.1.2: Rietveld refinements of neutron powder diffraction data collected in an applied magnetic field of 0.1 T, in field cooled conditions at: d) 30 K, e) 40 K, f) 50 K.

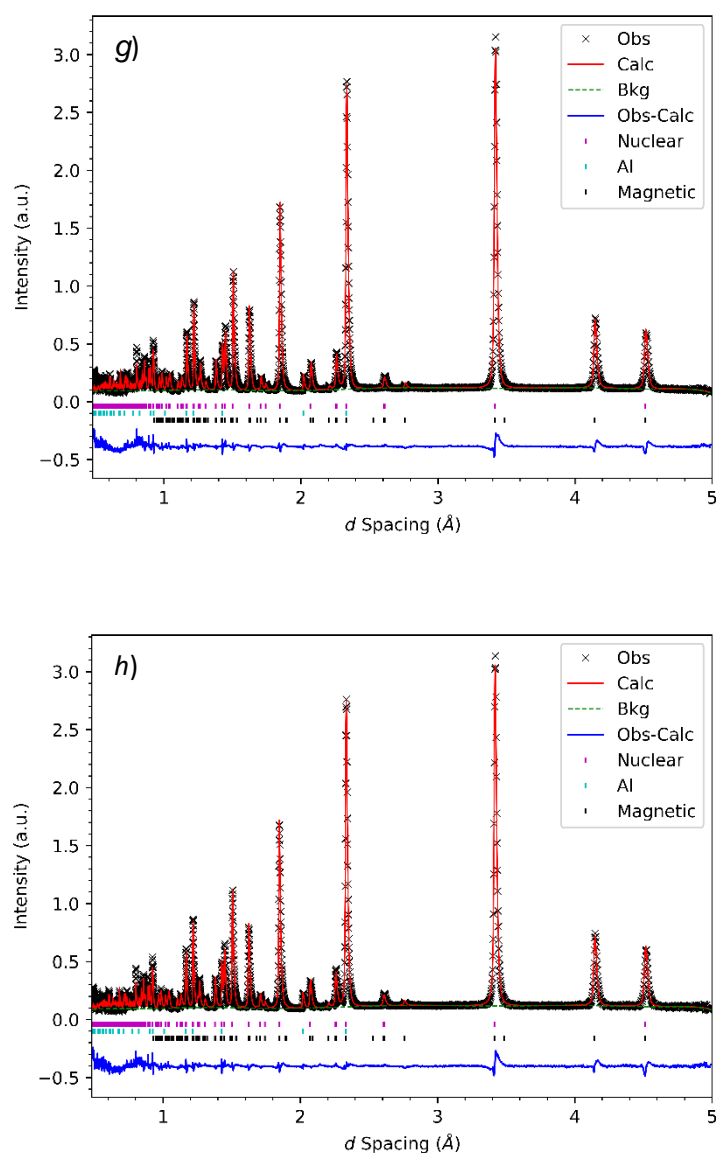


Fig.App.1.2: Rietveld refinements of neutron powder diffraction data collected in an applied magnetic field of 0.1 T, in field cooled conditions at: g) 60 K, h) 80 K.

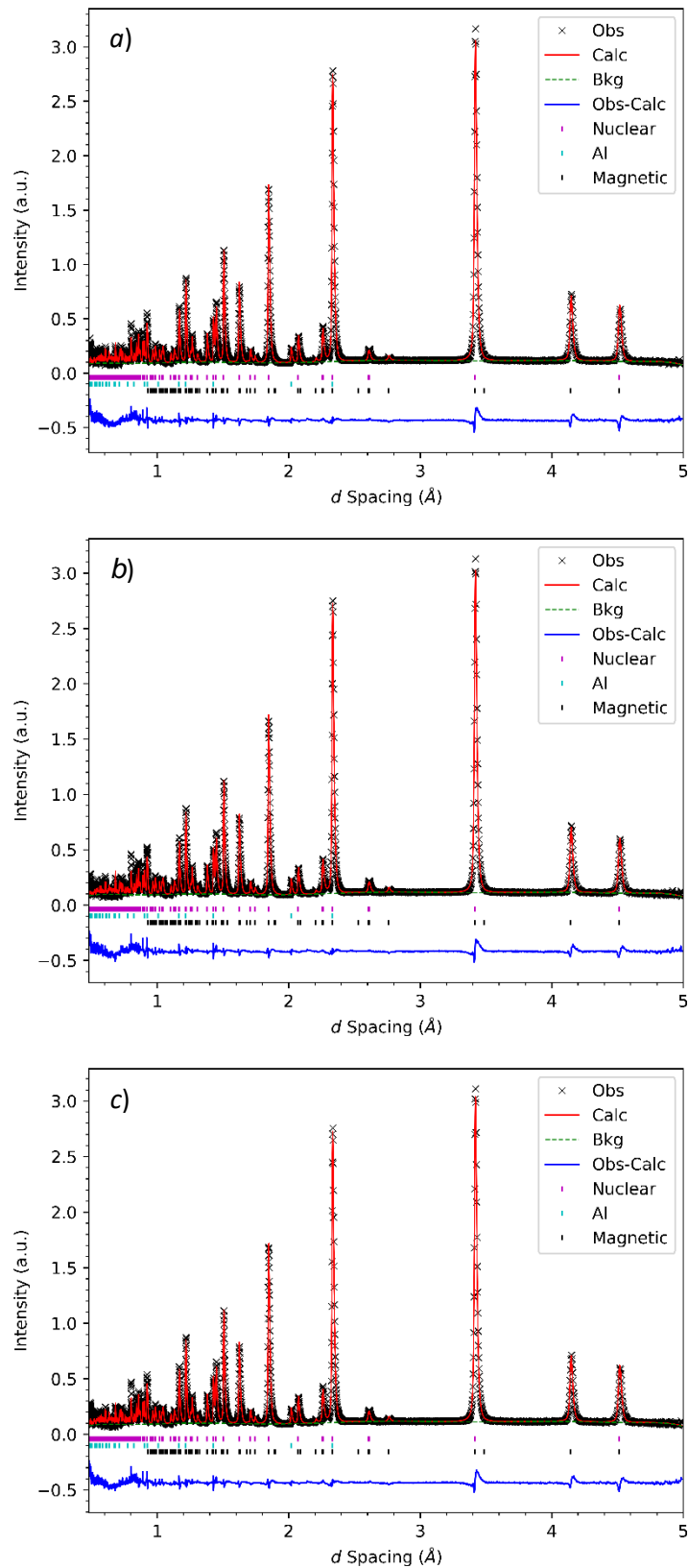


Fig.App.1.3: Rietveld refinements of neutron powder diffraction data collected in an applied magnetic field of 0.5 T, in zero field cooled conditions at: a) 1 K, b) 10 K, c) 20 K.

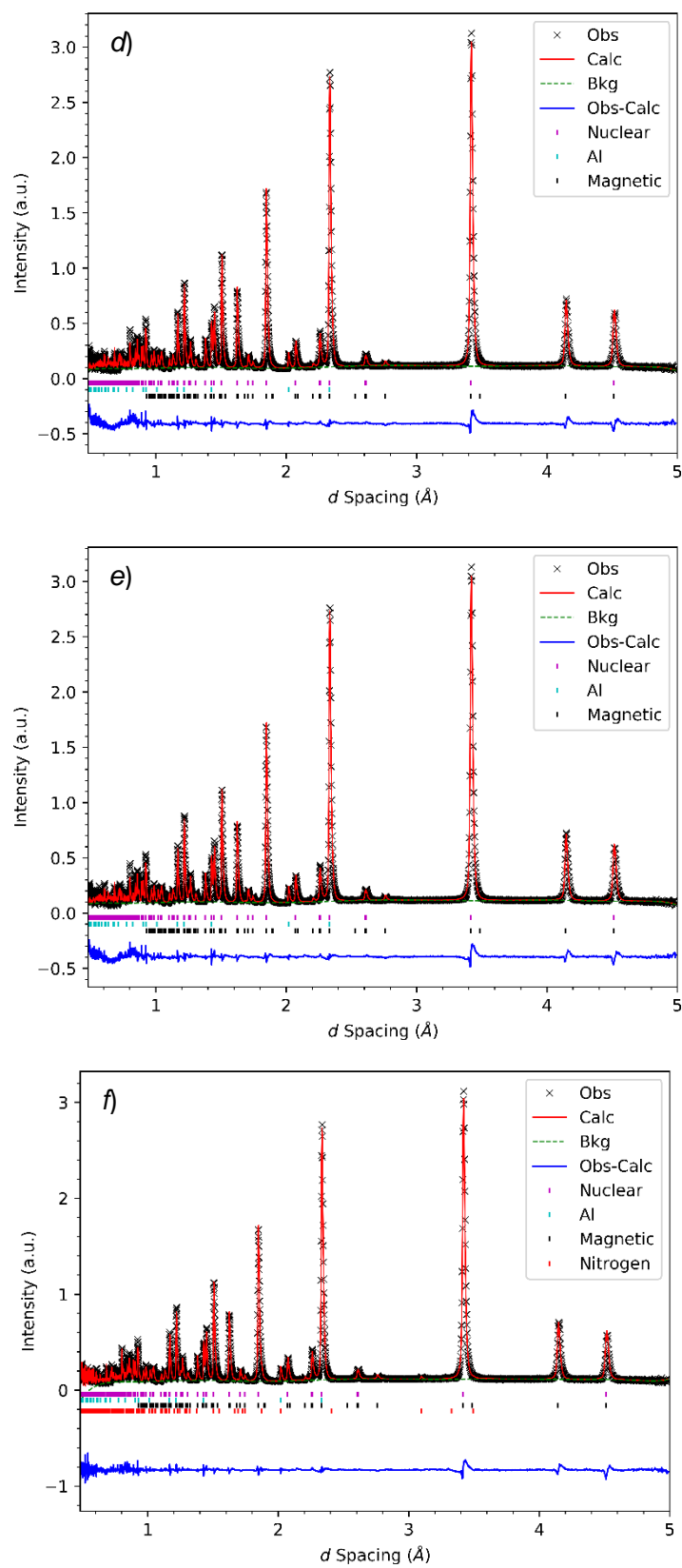


Fig.App.1.3: Rietveld refinements of neutron powder diffraction data collected in an applied magnetic field of 0.5 T, in zero field cooled conditions at: d) 30 K, e) 40 K, f) 50 K.

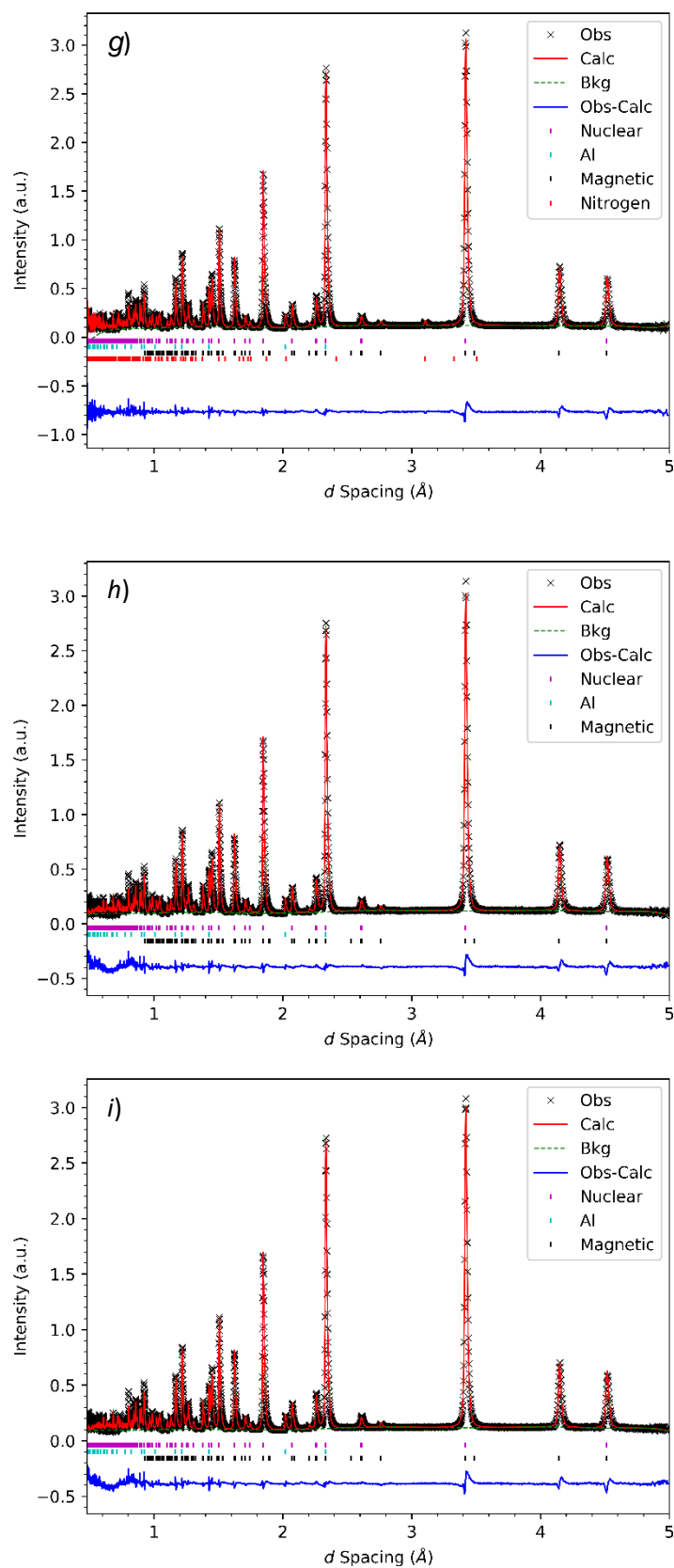


Fig.App.1.3: Rietveld refinements of neutron powder diffraction data collected in an applied magnetic field of 0.5 T, in zero field cooled conditions at: g) 60 K, h) 80 K, i) 100 K.

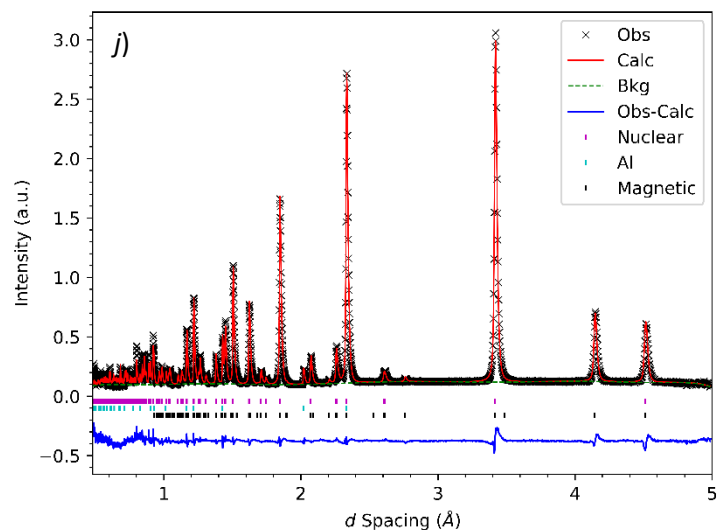


Fig.App.1.3 j): Rietveld refinements of neutron powder diffraction data collected in an applied magnetic field of 0.5 T, in zero field cooled conditions at 150 K.

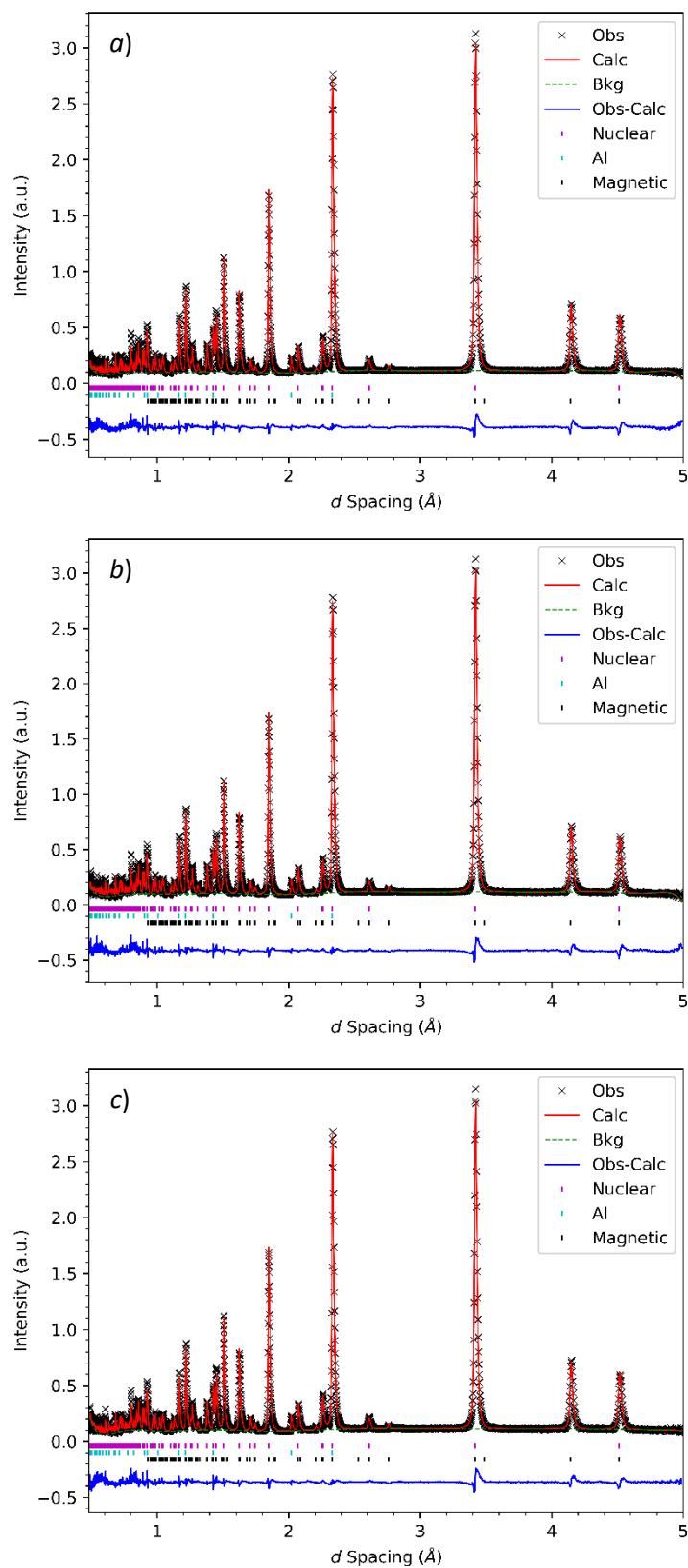


Fig.App.1.4: Rietveld refinements of neutron powder diffraction data collected in an applied magnetic field of 3 T, in zero field cooled conditions at: a) 1 K, b) 10 K, c) 30K.

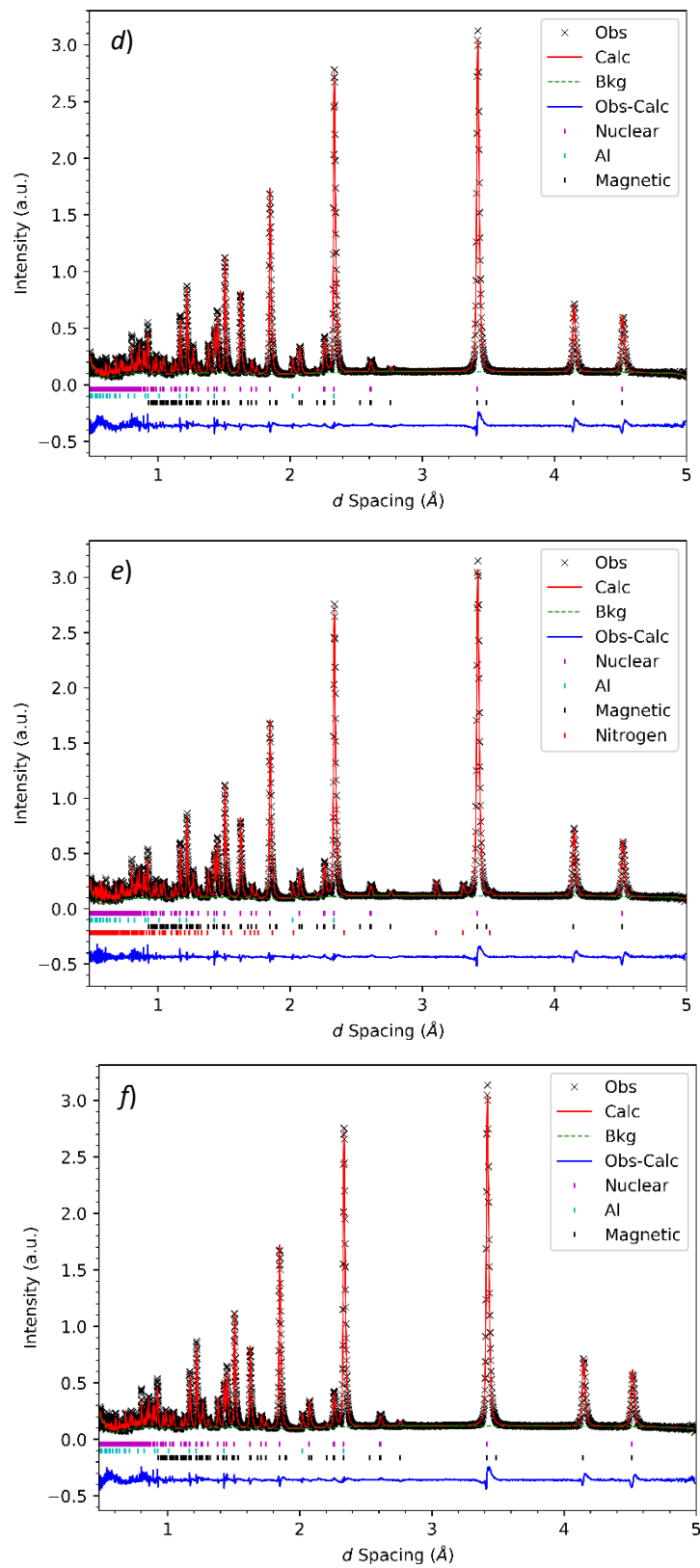


Fig.App.1.4: Rietveld refinements of neutron powder diffraction data collected in an applied magnetic field of 3 T, in zero field cooled conditions at: d) 40 K, e) 50 K, f) 60 K.

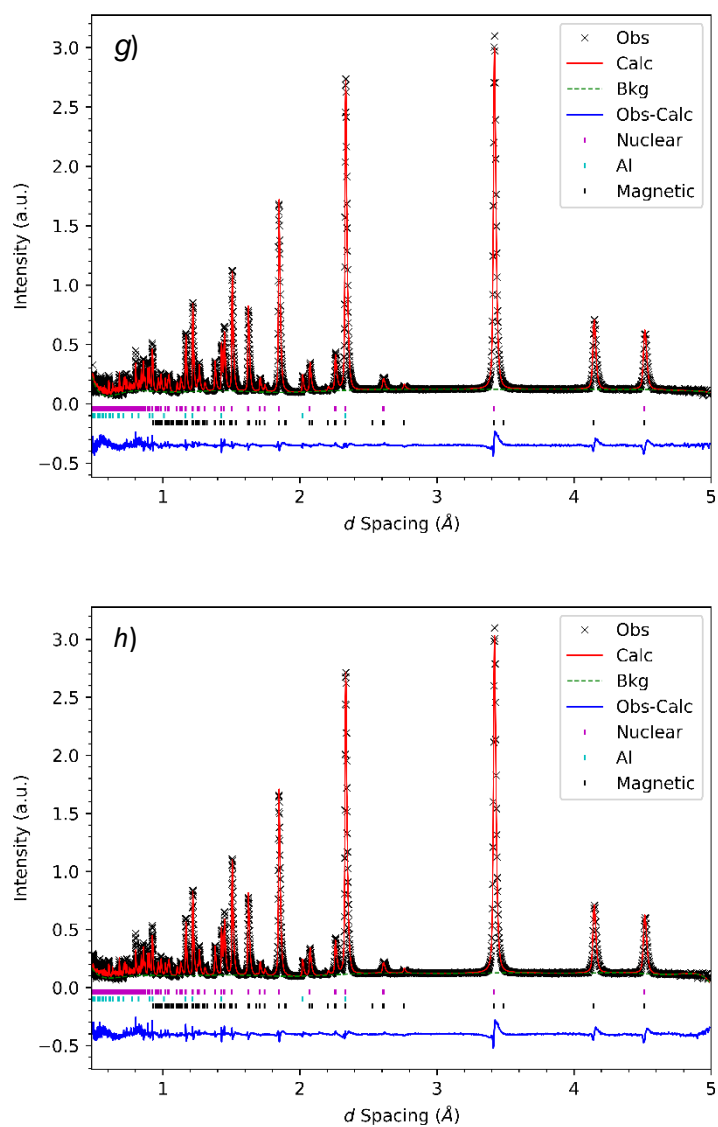


Fig.App.1.4: Rietveld refinements of neutron powder diffraction data collected in an applied magnetic field of 3 T, in zero field cooled conditions at: g) 80 K, h) 94 K.

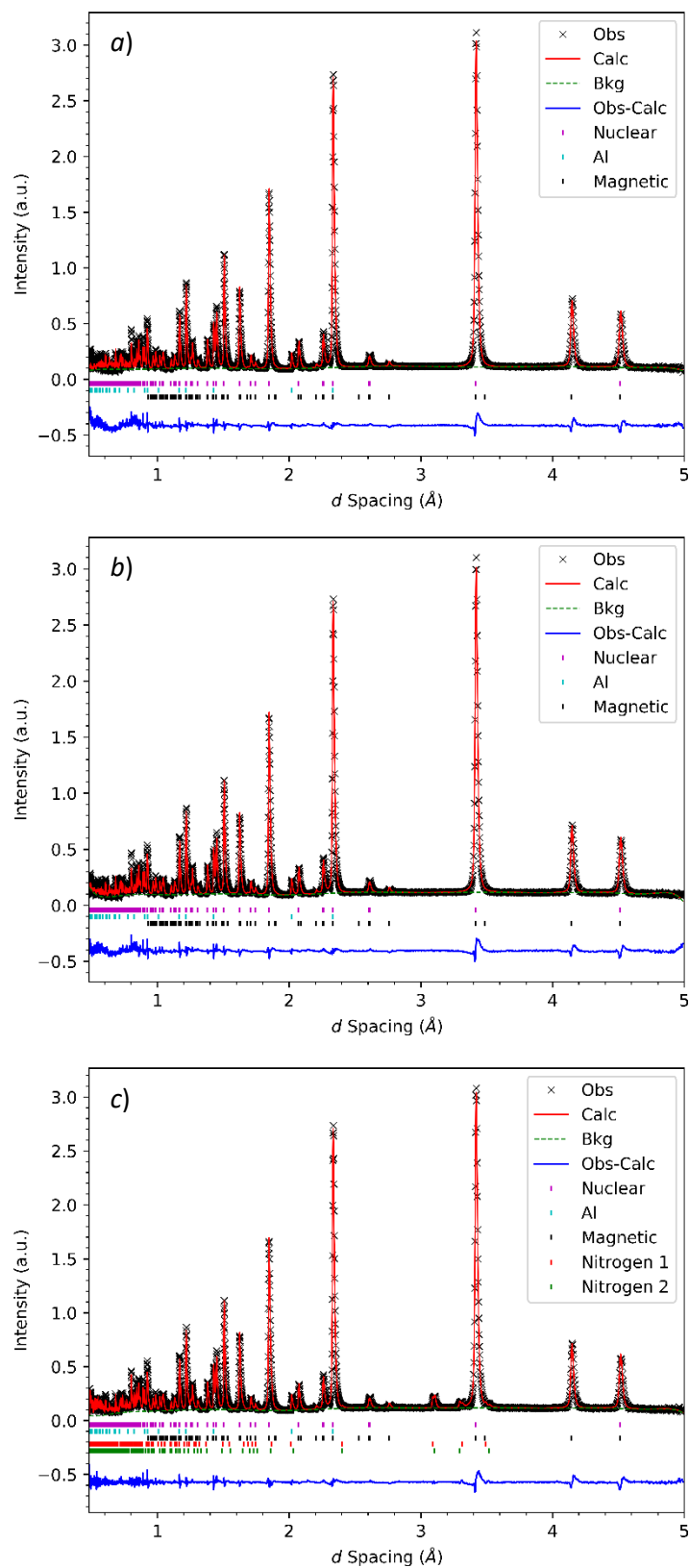


Fig.App.1.5: Rietveld refinements of neutron powder diffraction data collected in an applied magnetic field of 7 T, in zero field cooled conditions at: a) 1 K, b) 10 K, c) 50 K.

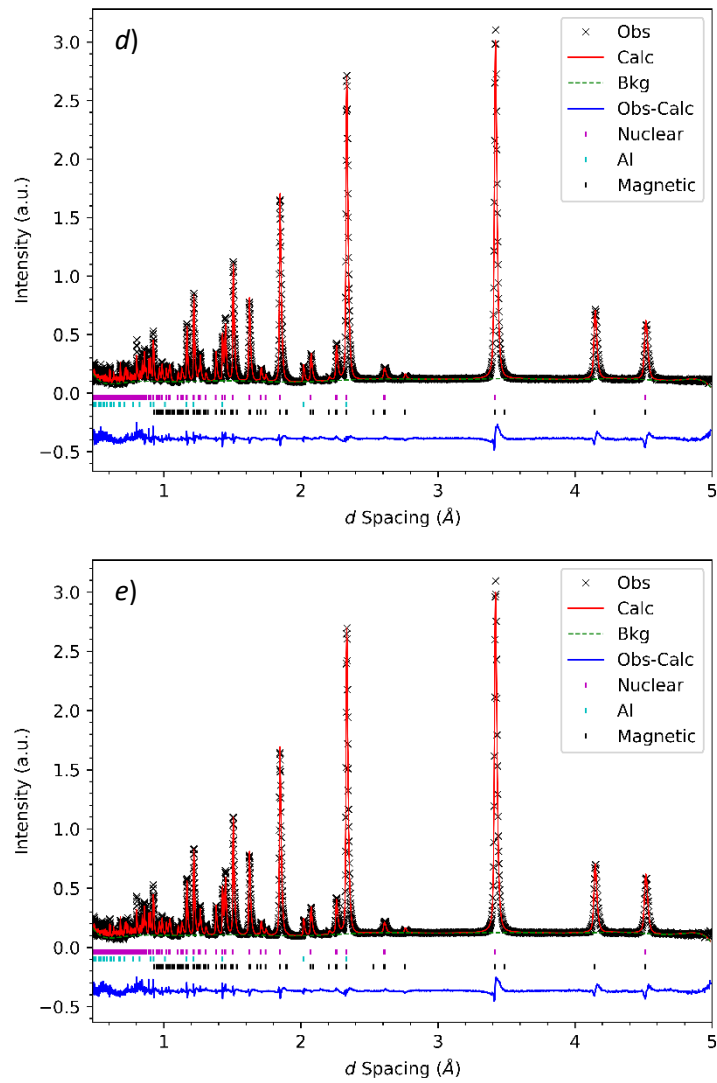


Fig.App.1.5: Rietveld refinements of neutron powder diffraction data collected in an applied magnetic field of 7 T, in zero field cooled conditions at: d) 80 K, e) 100 K.

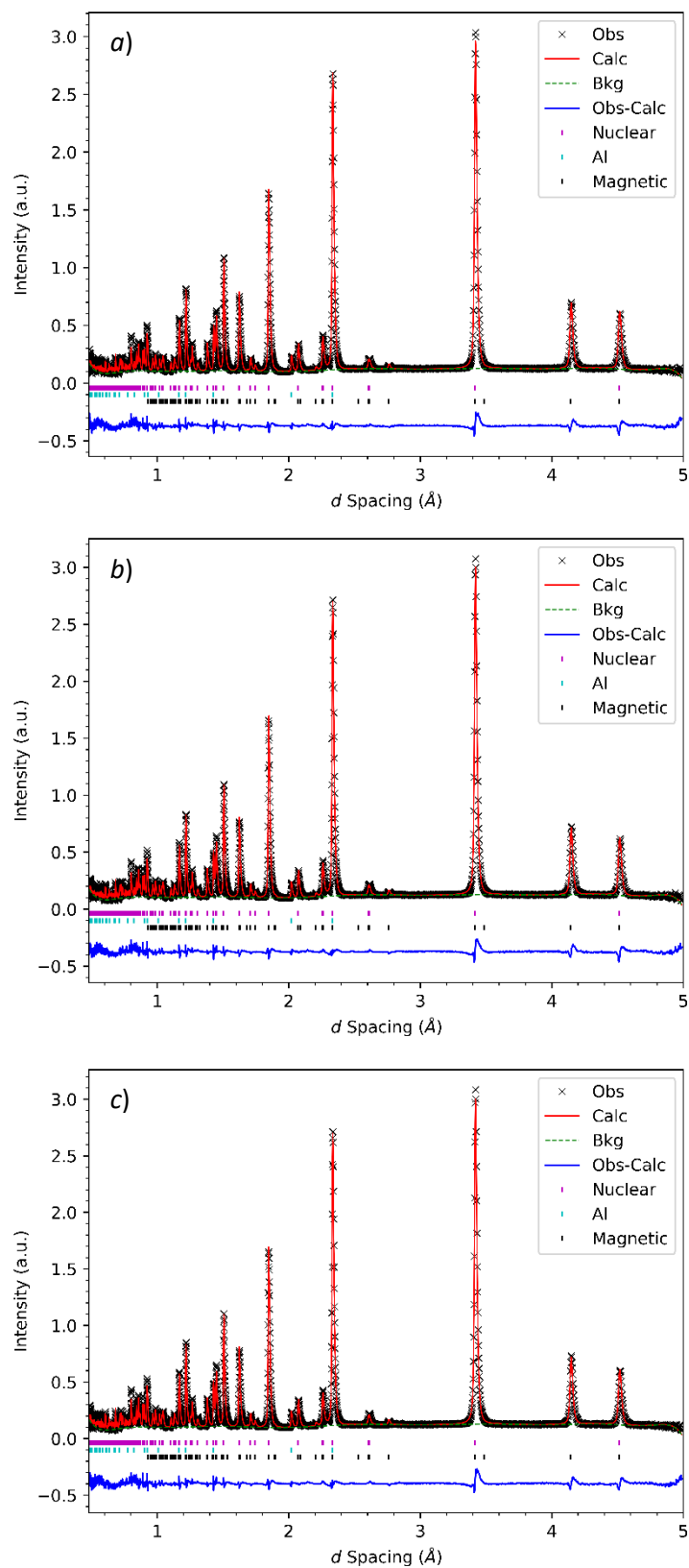


Fig.App.1.6: Rietveld refinements of neutron powder diffraction data collected in zero applied field, upon cooling at: a) 150 K, b) 100 K, c) 80 K.

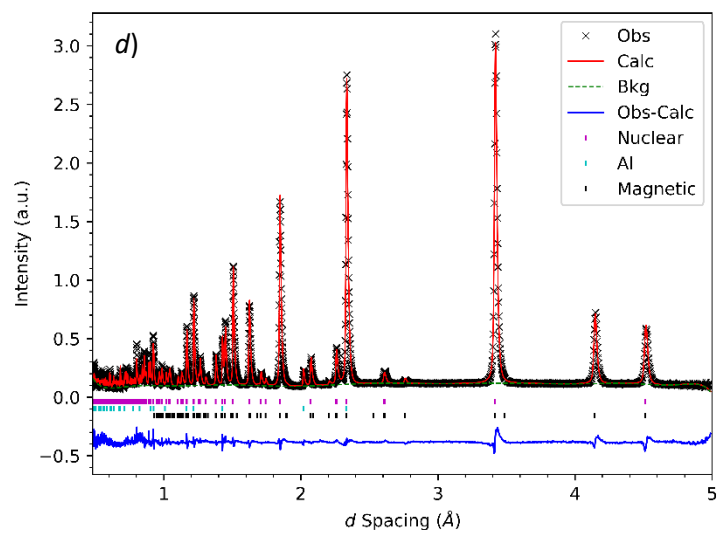


Fig.App.1.6 d): Rietveld refinement of neutron powder diffraction data collected in zero applied field, upon cooling at 50 K.

Table. App1.1: Refinement parameters for the NPD data collected in an applied field of 0.1 T at temperatures from 1 to 150 K, having been zero field cooled. Both the SrRu₂O₆ and aluminium (Al) phases are included. Note that the magnetic phase of SrRu₂O₆ has the same parameters as shown only with the c-axis doubled.

Refined parameter	1 K	10 K	20 K	30 K	40 K	50 K	60 K	80 K	100 K	150 K
Rp (%)	5.01	5.02	4.89	4.98	5.05	4.97	4.98	4.92	4.88	4.78
wRp (%)	5.34	5.43	5.33	5.39	5.42	5.32	5.37	5.27	5.30	5.17
χ^2	14.03	14.51	13.99	14.28	14.42	13.90	14.15	13.65	13.85	13.21
SrRu2O6 Phase										
$a = b$ (Å)	5.21084(11)	5.21069(7)	5.21081(7)	5.21079(7)	5.21078(7)	5.21067(7)	5.21063(7)	5.21052(8)	5.21034(7)	5.21005(7)
c (Å)	5.22522(21)	5.22539(14)	5.22535(14)	5.22543(14)	5.22540(14)	5.22556(14)	5.22575(15)	5.22588(15)	5.22637(15)	5.22777(15)
Cell volume (Å ³)	122.871(6)	122.868(4)	122.873(4)	122.874(4)	122.872(4)	122.872(4)	122.874(4)	122.872	122.875(4)	122.894(4)
Sr - Uiso/Ue x 100 (Å ²)	1.77(6)	1.84(6)	.82(6)	1.86(6)	1.84(6)	1.88(6)	1.90(6)	1.91(6)	1.97(6)	1.99(6)
Ru - Uiso/Ue x 100 (Å ²)	0.45(5)	0.41(5)	0.43(5)	0.41(5)	0.42(5)	0.45(5)	0.45(5)	0.49(5)	0.46(5)	0.50(5)
O - Uiso/Ue x 100 (Å ²)	1.25(4)	1.28(4)	1.28(4)	1.32(4)	1.32(4)	1.32(4)	1.34(4)	1.33(4)	1.41(4)	1.43(4)
Sr (0, 0, 0)	-	-	-	-	-	-	-	-	-	-
Ru (1/3, 2/3, 1/2)	-	-	-	-	-	-	-	-	-	-
O (x, 0, z)	0.37790(16) 0.3005(4)	0.37804(16) 0.3011(4)	0.37797(16) 0.3007(4)	0.37802(16) 0.3011(4)	0.37802(16) 0.3010(4)	0.37802(16) 0.3008(4)	0.377933(16) 0.301035(40)	0.377936(16) 0.300667(40)	0.378104(16) 0.301188(40)	0.37826(16) 0.3009(4)
Al Phase										
$a = b = c$ (Å)	4.03390(13)	4.03358(13)	4.03388(13)	4.03383(13)	4.03383(13)	4.03399(13)	4.03404(13)	4.03475(13)	4.03523(13)	4.03758(12)
Cell volume (Å ³)	65.641(4)	65.625(4)	65.640(4)	65.638(4)	65.638(4)	65.645(4)	65.648(4)	65.683(4)	65.706(4)	65.8209(35)
Al - Uiso/Ue x 100 (Å ²)	1.65(16)	1.62(16)	1.61(15)	1.52(15)	1.62(16)	1.57(15)	1.56(15)	1.56(15)	1.66(16)	1.82(16)
Al (0, 0, 0)	-	-	-	-	-	-	-	-	-	-

Table.App1.2: Refinement parameters for the NPD data collected in an applied field of 0.1 T at temperatures from 1 to 150 K, having been field cooled. Both the SrRu₂O₆ and aluminium (Al) phases are included. Note that the magnetic phase of SrRu₂O₆ has the same parameters as shown only with the *c*-axis doubled and μ_{Ru} is shown as this was not shown earlier with the refined moments in the results section.

Refined parameter	1 K	10 K	20 K	30 K	40 K	50 K	60 K	80 K
R _p (%)	5.04	4.90	4.94	4.88	4.78	4.86	4.83	5.12
wR _p (%)	5.36	5.25	5.31	5.30	5.25	5.29	5.24	5.41
χ^2	14.13	13.56	13.91	13.83	13.57	13.80	13.58	5.68
SrRu₂O₆ Phase								
<i>a</i> = <i>b</i> (Å)	5.21071(7)	5.21078(7)	5.21090(7)	5.21092(7)	5.21088(7)	5.21075(8)	5.21072(7)	5.21065(7)
<i>c</i> (Å)	5.22535(15)	5.22524(14)	5.22553(14)	5.22544(14)	5.22549(15)	5.22557(17)	5.22569(14)	5.22587(15)
Cell volume (Å ³)	122.868(4)	122.869(4)	122.822(4)	122.880(4)	122.880(4)	122.875(5)	122.877(4)	122.878(4)
Sr - U _{iso} /U _e x 100 (Å ²)	1.75(6)	1.77(6)	1.65(6)	1.80(6)	1.81(6)	1.82(6)	1.86(6)	1.88(7)
Ru - U _{iso} /U _e x 100 (Å ²)	0.45(5)	0.41(5)	0.41(5)	0.45(5)	0.40(5)	0.46(5)	0.48(5)	0.45(5)
O - U _{iso} /U _e x 100 (Å ²)	1.25(4)	1.25(4)	1.25(4)	1.24(4)	1.27(4)	1.29(4)	1.28(4)	1.32(4)
Sr (0, 0, 0)	-	-	-	-	-	-	-	-
Ru (1/3, 2/3, 1/2)	-	-	-	-	-	-	-	-
O (<i>x</i> , 0, <i>z</i>)	0.377972(16)	0.378054(16)	0.378237(16)	0.37788(16)	0.378295(16)	0.37799(16)	0.37795(16)	0.37811(16)
	0.300616(4)	0.300647(4)	0.301482(40)	0.3005(4)	0.301018(40)	0.3007(4)	0.3006(4)	0.3010(4)
μ_{Ru} (μ _B)	1.467(13)	1.466(13)	1.442(14)	1.466(13)	1.465(15)	1.466(13)	1.466(13)	1.470(14)
Al Phase								
<i>a</i> = <i>b</i> = <i>c</i> (Å)	4.00389(13)	4.03394(13)	4.03405(13)	4.03397(13)	4.03397(13)	4.03417(13)	4.03422(13)	4.03473(13)
Cell volume (Å ³)	65.640(4)	65.643(4)	65.648(4)	65.644(4)	65.644(4)	65.654(4)	65.657(4)	65.682(4)
Al - U _{iso} /U _e x 100 (Å ²)	1.64(16)	1.61(16)	1.61(16)	1.55(15)	1.62(15)	1.61(15)	1.65(16)	1.63(16)
Al (0, 0, 0)	-	-	-	-	-	-	-	-

Table.App1.3: Refinement parameters for the NPD data collected in an applied field of 0.5 T at temperatures from 1 to 150 K, having been zero field cooled. Both the SrRu₂O₆ and aluminium (Al) phases are included. Note that the magnetic phase of SrRu₂O₆ has the same parameters as shown only with the *c*-axis doubled.

Refined parameter	1 K	10 K	20 K	30 K	40 K	50 K	60 K	80 K	100K	150 K
R _p (%)	4.99	5.03	5.08	4.97	5.01	4.41	4.37	4.95	4.93	4.78
wR _p (%)	5.36	5.31	5.40	5.33	5.38	4.63	4.53	5.30	5.23	5.12
χ ²	9.431	9.178	9.511	9.262	9.443	6.992	6.727	9.256	9.042	9.896
SrRu₂O₆ Phase										
<i>a</i> = <i>b</i> (± 7 × 10 ⁻⁵ Å)	5.21087	5.21096	5.21088	5.21090	5.21083	5.21076	5.21078	5.21071	5.21052	5.21017
<i>c</i> (± 14 × 10 ⁻⁵ Å)	5.22544	5.22546	5.22551	5.22543	5.22555	5.22565	5.22573	5.22598	5.22645	5.22805
Cell volume ((± 4 × 10 ⁻³ Å ³)	122.878	122.883	122.880	122.879	122.879	122.878	122.881	122.883	122.885	122.906
Sr - U _{iso} /U _e × 100 (Å ²)	1.77(6)	1.79(6)	1.81(6)	1.80(6)	1.81(6)	1.78(6)	1.84(6)	1.85(6)	1.92	1.95(6)
Ru - U _{iso} /U _e × 100 (Å ²)	0.41(5)	1.00	0.41(5)	0.44(5)	0.44(5)	0.49(5)	0.45(5)	0.48(5)	0.5	0.55(5)
O - U _{iso} /U _e × 100 (Å ²)	1.23(4)	1.18(4)	1.23(4)	1.26(4)	1.26(4)	1.25(4)	1.29(4)	1.31(4)	1.33	1.39(4)
Sr (0, 0, 0)	-	-	-	-	-	-	-	-	-	-
Ru (1/3, 2/3, 1/2)	-	-	-	-	-	-	-	-	-	-
O (<i>x</i> , 0, <i>z</i>)	0.37802(16) 0.3008(4)	0.37718(14) 0.29853(33)	0.37809(16) 0.3010(4)	0.37795(16) 0.3008(4)	0.37798(16) 0.3008(4)	0.37784(16) 0.3004(4)	0.37804(16) 0.3008(4)	0.37798(16) 0.3007(4)	0.378150 0.300627	0.37814(16) 0.3005(4)
Al Phase										
<i>a</i> = <i>b</i> = <i>c</i> (Å)	4.03394(13)	4.03393(13)	4.03381(13)	4.03392(13)	4.03404(13)	4.03411(13)	4.03423(13)	4.03465(12)	4.03537(13)	4.03758(12)
Cell volume (Å ³)	65.643(4)	65.643(4)	65.637(4)	65.642(4)	65.648(4)	65.652(4)	65.657(4)	65.6778(35)	65.713(4)	65.8208(34)
Al - U _{iso} /U _e × 100 (Å ²)	1.64(16)	1.00	1.55(15)	1.63(15)	1.54(15)	1.56(15)	1.60(15)	1.60(15)	1.59	1.82(16)
Al (0, 0, 0)	-	-	-	-	-	-	-	-	-	-

Table. App1.4: Refinement parameters for the NPD data collected in an applied field of 3 T at temperatures from 1 to 150 K, having been zero field cooled. Both the SrRu₂O₆ and aluminium (Al) phases are included. Note that the magnetic phase of SrRu₂O₆ has the same parameters as shown only with the *c*-axis doubled.

Refined parameter	1 K	10 K	20 K	30 K	40 K	50 K	60 K	80 K	100K	150 K
Rp (%)	4.96	4.92	4.57	4.55	4.58	4.01	4.52	4.33	4.99	4.70
wRp (%)	5.12	5.13	4.93	4.89	4.91	4.34	4.84	4.55	5.36	4.81
χ^2	8.583	8.629	7.965	7.825	7.910	6.205	7.747	6.867	9.243	7.715
SrRu2O6 Phase										
$a = b$ (Å)	5.21091(7)	5.21087(7)	5.21084(6)	5.21085(6)	5.21080(6)	5.21079(7)	5.21071(6)	5.21046(6)	5.21044(7)	5.21011(6)
c (Å)	5.22544(13)	5.22544(13)	5.22549(13)	5.22547(13)	5.22549(13)	5.22566(15)	5.22578(13)	5.22594(12)	5.22697(14)	5.22864(13)
Cell volume (Å ³)	122.880(4)	122.878(4)	122.878(4)	122.878(4)	122.876(4)	122.880(4)	122.879(4)	122.8702(35)	122.894(4)	122.918(4)
Sr - Uiso/Ue x 100 (Å ²)	1.69(6)	1.68(6)	1.72(6)	1.74(6)	1.72(6)	1.72(7)	1.75(6)	1.73(5)	1.85(7)	1.86(6)
Ru - Uiso/Ue x 100 (Å ²)	0.46(4)	0.49(4)	0.46(4)	0.47(4)	0.51(4)	0.47(5)	0.49(4)	0.51(4)	0.49(5)	0.59(4)
O - Uiso/Ue x 100 (Å ²)	1.21(4)	1.20(4)	1.21(4)	1.23(4)	1.22(4)	1.22(4)	1.25(4)	1.23(4)	1.33(4)	1.32(4)
Sr (0, 0, 0)	-	-	-	-	-	-	-	-	-	-
Ru (1/3, 2/3, 1/2)	-	-	-	-	-	-	-	-	-	-
O (x, 0, z)	0.37782(15) 0.3008(4)	0.377919(16) 0.300505(40)	0.37800(15) 0.3008(4)	0.37803(14) 0.3009(4)	0.37788(15) 0.3009(4)	0.37980(17) 0.300888(40)	0.37786(15) 0.3007(4)	0.37808(14) 0.30061(33)	0.37801(16) 0.3012(4)	0.37797(15) 0.3002(4)
Al Phase										
$a = b = c$ (Å)	4.03385(12)	4.03390(12)	4.03394(12)	4.03395(12)	4.03402(12)	4.03407(14)	4.03422(12)	4.03476(11)	4.03503(13)	4.03792(12)
Cell volume (Å ³)	65.6385(35)	65.6409(35)	65.6430(34)	65.6436(34)	65.6469(34)	65.650(4)	65.6565(34)	65.6829(31)	65.696(4)	65.8375(34)
Al - Uiso/Ue x 100 (Å ²)	1.78(16)	1.71(16)	1.69(15)	1.86(16)	1.74(15)	1.84(16)	1.87(16)	1.74(14)	1.86(17)	1.91(15)
Al (0, 0, 0)	-	-	-	-	-	-	-	-	-	-

Table.App1.5: Refinement parameters for the NPD data collected in an applied field of 7 T at temperatures from 1 to 150 K, having been zero field cooled. Both the SrRu₂O₆ and aluminium (Al) phases are included. Note that the magnetic phase of SrRu₂O₆ has the same parameters as shown only with the *c*-axis doubled.

Refined parameter	1 K	10 K	30 K	50 K	80 K	100K	150K
R _p (%)	5.03	5.04	5.02	4.17	4.89	4.85	4.91
wR _p (%)	5.46	5.27	5.19	4.44	5.14	5.10	5.26
χ ²	9.729	9.033	8.775	6.475	8.707	8.633	9.135
SrRu₂O₆ Phase							
<i>a</i> = <i>b</i> (Å)	5.21096(7)	5.21097(7)	5.21088(7)	5.21083(8)	5.210723(34)	5.21049(7)	5.21010(7)
<i>c</i> (Å)	5.22545(14)	5.22558(14)	5.22558(14)	5.22574(16)	5.22613(5)	5.22693(14)	5.22885(14)
Cell volume (Å ³)	122.882(4)	122.886(4)	122.881(4)	122.883(5)	122.8872(16)	122.895(4)	122.922(4)
Sr - U _{iso} /U _e x 100 (Å ²)	1.75(6)	1.71(6)	1.75(6)	1.72(6)	1.77(6)	1.85(6)	1.96(6)
Ru - U _{iso} /U _e x 100 (Å ²)	0.40(5)	0.46(5)	0.43(5)	0.47(5)	0.47(5)	0.50(5)	0.56(5)
O - U _{iso} /U _e x 100 (Å ²)	1.27(4)	1.23(4)	1.23(4)	1.21(4)	1.28(4)	1.32(4)	1.41(4)
Sr (0, 0, 0)	-	-	-	-	-	-	-
Ru (1/3, 2/3, 1/2)	-	-	-	-	-	-	-
O (<i>x</i> , 0, <i>z</i>)	0.37799(16) 0.3008(4)	0.37791(16) 0.3009(4)	0.37797(15) 0.3009(4)	0.377901(15) 0.300797(40)	0.37796(16) 0.3009(4)	0.377926(16) 0.300761(4)	0.378103(16) 0.300153(4)
Al Phase							
<i>a</i> = <i>b</i> = <i>c</i> (Å)	4.03389(13)	4.03377(13)	4.03390(13)	4.03400(15)	4.03457(13)	4.03533(13)	4.03779(13)
Cell volume (Å ³)	65.641(4)	65.635(4)	65.641(4)	65.646(4)	65.674(4)	65.711(4)	65.831(4)
Al - U _{iso} /U _e x 100 (Å ²)	1.68(16)	1.74(16)	1.74(16)	1.85(16)	1.70(16)	1.85(16)	1.78(16)
Al (0, 0, 0)	-	-	-	-	-	-	-

Table.App1.6: Refinement parameters for the NPD data collected in zero applied field as the sample was cooled from 150 to 50 K. Both the SrRu₂O₆ and aluminium (Al) phases are included. Note that the magnetic phase of SrRu₂O₆ has the same parameters as shown only with the c-axis doubled.

Refined parameter	150 K	100 K	80 K	50 K
R _p (%)	4.74	4.88	4.84	4.95
wR _p (%)	4.96	5.03	5.07	5.19
χ ²	8.163	8.421	8.580	8.821
SrRu₂O₆ Phase				
<i>a</i> = <i>b</i> (Å)	5.21009(6)	5.21040(7)	5.21073(7)	5.21087(7)
<i>c</i> (Å)	5.22917(14)	5.22770(14)	5.22655(14)	5.22574(14)
Cell volume (Å ³)	122.929(4)	122.909(4)	122.898(4)	122.885(4)
Sr - U _{iso} /U _e x 100 (Å ²)	1.94(6)	1.87(6)	1.53(6)	1.75(6)
Ru - U _{iso} /U _e x 100 (Å ²)	0.59(5)	0.52(5)	0.39(5)	0.47(5)
O - U _{iso} /U _e x 100 (Å ²)	1.39(4)	1.36(4)	1.07(4)	1.25(4)
Sr (0, 0, 0)	-	-	-	-
Ru (1/3, 2/3, 1/2)	-	-	-	-
O (<i>x</i> , 0, <i>z</i>)	0.378021(16)	0.378100(16)	0.377987(16)	0.37788(15)
	0.300338(40)	0.301072(40)	0.300454(4)	0.3009(4)
Al Phase				
<i>a</i> = <i>b</i> = <i>c</i> (Å)	4.03810(12)	4.03573(12)	4.03490(13)	4.03404(13)
Cell volume (Å ³)	65.8464(35)	65.7306(35)	65.690(4)	65.648(4)
Al - U _{iso} /U _e x 100 (Å ²)	2.04(16)	1.88(16)	2.00(16)	1.68(15)
Al (0, 0, 0)	-	-	-	-

Table.App1.7: Bond lengths and bond angles for the SrRu_2O_6 phase; obtained from refinement of the NPD data in an applied field of 0.1 T at temperatures from 1 to 150 K, having been zero filed cooled.

Bond Length (Å)	1 K	10 K	20 K	30 K	40 K	50 K	60 K	80 K	100 K	150 K
Sr-O	2.5186(16)	2.5212(16)	2.5194(16)	2.5212(16)	2.5206(16)	2.5199(16)	5.2047(3)	2.51927(4)	2.52169(4)	2.5215(16)
Ru-Ru	3.00845(6)	3.00836(4)	3.00843(4)	3.00842(4)	3.00841(4)	3.00835(4)	3.00833(4)	3.00826(4)	3.00816(4)	3.00799(4)
Ru-O	3.00854(6)	3.00845(4)	3.00852(4)	3.00851(4)	3.00850(4)	3.00844(4)	3.00842(4)	3.00835(4)	3.00825(4)	3.00808(4)
	1.9376(12)	1.9355 (12)	1.9370(12)	1.9356(12)	1.9361(12)	1.9366(12)	1.93602(2)	1.93703(2)	1.93529 (2)	1.9360(12)
Bond Angle (°)										
Sr-O-Sr	126.309(27)	126.271(28)	126.296(27)	126.273(28)	126.279(28)	123.288(27)	126.290(1)	126.303(1)	126.266(1)	126.262(28)
	126.310(27)	126.272(28)	126.297(27)	126.274(28)	126.280(28)	126.289(27)	126.292(1)	126.304(1)	126.267(1)	126.263(28)
Ru-O-Ru	101.86(9)	102.00(9)	101.90(27)	102.00(9)	101.96(9)	101.92(9)	101.963(1)	101.886(1)	102.008(1)	101.95(9)

Table.App1.8: Bond lengths and bond angles for the SrRu_2O_6 phase; obtained from refinement of the NPD data in an applied field of 0.1 T at temperatures from 1 to 80 K, having been filed cooled.

Bond Length (Å)	1 K	10 K	20 K	30 K	40 K	50 K	60 K	80 K
Sr-O	2.51921(4)	2.51965(3)	2.52320(3)	2.5187 (15)	2.52191(4)	2.5194(16)	2.5193(15)	2.5211(16)
Ru-Ru	3.00838(4)	3.00842(4)	3.00848(4)	3.00849(4)	3.00847(4)	3.00840(5)	3.00838(4)	3.00834(4)
	3.00847(4)	3.00851(4)	3.00858(4)	3.00859(4)	3.00856(4)	3.00849(5)	3.00847(4)	3.00843(4)
Ru-O	1.93711(3)	1.93691(2)	1.93429(12)	1.9376 (12)	1.93548(3)	1.9370(12)	1.9371(12)	1.9358(12)
Bond Angle (°)								
Sr-O-Sr	126.298(1)	126.285(1)	126.233(1)	126.312(27)	126.241(1)	126.295(27)	126.301(27)	126.268(28)
	126.299(1)	126.286(1)	126.234(1)	126.313(27)	126.242(1)	126.296(27)	126.302(27)	126.269(28)
Ru-O-Ru	101.885(1)	101.903(1)	102.096(1)	101.86(9)	102.008(1)	101.89(9)	101.89(9)	101.98(9)

TableApp1.19: Bond lengths and bond angles for the $SrRu_2O_6$ phase; obtained from refinement of the NPD data in an applied field of 0.5 T at temperatures from 1 to 150 K, having been zero filed cooled.

Bond Length (Å)	1 K	10 K	20 K	30 K	40 K	50 K	60 K	80 K	100 K	150 K
Sr-O	2.5201(16)	2.5093(13)	2.5209(16)	2.5196(16)	2.5200(16)	2.5182(15)	2.5203(16)	2.5197(16)	2.52012(3)	2.5198(16)
Ru-Ru	3.00847(4)	3.00852(4)	3.00847(4)	3.00848(4)	3.00844(4)	3.00840(4)	3.00842(4)	3.00837(4)	3.00827(4)	3.00806(4)
Ru-O	3.00856(4)	3.00861(4)	3.00856(4)	3.00857(4)	3.00853(4)	3.00849(4)	3.00851(4)	3.00846(4)	3.00836(4)	3.00815(4)
Ru-O	1.9365(12)	1.9444(10)	1.9360(12)	1.9368(12)	1.9366(12)	1.9378(12)	1.9364(12)	1.9369(12)	1.93684(2)	1.9373(12)
Bond Angle (°)										
Sr-O-Sr	126.285(27)	126.471(23)	126.270(28)	126.295(27)	126.290(28)	126.322(27)	126.283(28)	126.295(28)	126.279(1)	126.291(27)
Ru-O-Ru	126.286(27)	126.472(23)	126.271(28)	126.296(27)	126.291(28)	126.323(27)	126.284(28)	126.296(28)	126.280(1)	126.293(27)
Ru-O-Ru	101.93(9)	101.36(7)	101.97(9)	101.91(9)	101.93(9)	101.83(9)	101.94(9)	101.90(9)	101.9(1)	101.86(9)

Table.App1.10: Bond lengths and bond angles for the $SrRu_2O_6$ phase; obtained from refinement of the NPD data in an applied field of 3 T at temperatures from 1 to 150 K, having been zero filed cooled.

Bond Length (Å)	1 K	10 K	20 K	30 K	40 K	50 K	60 K	80 K	100 K	150 K
Sr-O	2.5191(15)	2.51870(3)	2.5200(14)	2.5203(14)	2.5197(14)	2.5202(17)	2.5189(14)	2.5197(13)	2.5216(17)	2.5184(14)
Ru-Ru	3.00849(4)	3.00847(4)	3.00845(4)	3.00845(4)	3.00843(4)	3.00843(4)	3.00838(4)	3.00823(3)	3.00822(4)	3.00803(4)
Ru-O	3.00858(4)	3.00856(4)	3.00854(4)	3.00854(4)	3.00852(4)	3.00852(4)	3.00847(4)	3.00832(3)	3.00831(4)	3.00812(4)
Ru-O	1.9370(11)	1.93756(2)	1.9365(11)	1.9363(11)	1.9366(11)	1.9364(13)	1.9372(11)	1.9369(10)	1.9354(13)	1.9384(11)
Bond Angle (°)										
Sr-O-Sr	126.313(26)	126.308(1)	126.288(25)	126.281(25)	126.302(25)	126.288(30)	126.313(25)	126.287(24)	126.278(29)	126.325(26)
Ru-O-Ru	126.314(26)	126.309(1)	126.289(25)	126.283(25)	126.303(25)	126.289(30)	126.314(25)	126.288(24)	126.279(29)	126.326(26)
Ru-O-Ru	101.90(8)	101.857(1)	101.93(8)	101.95(8)	101.92(8)	101.94(9)	101.87(8)	101.89(7)	102.00(9)	101.78(8)

Table.App1.11: Bond lengths and bond angles for the $SrRu_2O_6$ phase; obtained from refinement of the NPD data in an applied field of 7 T at temperatures from 1 to 150 K, having been zero field cooled.

Bond Length (Å)	1 K	10 K	30 K	50 K	80 K	100 K	150 K
Sr-O	2.5200(16)	2.5200(16)	2.5204(15)	2.5196(18)	2.5203(16)	2.51973(3)	2.51871(3)
Ru-Ru	3.00852(4)	3.00853(4)	3.00847(4)	3.00845(5)	3.00838(2)	3.00825(4)	3.00802(4)
Ru-O	1.9366(12)	1.9365(12)	1.9362(12)	1.9368(14)	1.9364(12)	1.93687(2)	1.93840(2)
Bond Angle (°)							
Sr-O-Sr	126.289(28)	126.296(27)	126.287(27)	126.302(32)	126.292(27)	126.305(1)	126.311(1)
Ru-O-Ru	101.93(9)	101.94(9)	101.95(9)	101.91(10)	101.94(9)	101.895(1)	101.775(1)

Table.App1.12: Bond lengths and bond angles for the $SrRu_2O_6$ phase; obtained from refinement of the NPD data in zero applied field as the sample was cooled from 150 to 50 K.

Bond Length (Å)	150 K	100 K	80 K	50 K
Sr-O	2.51904(3)	2.52157(3)	2.51898(3)	2.5200(15)
Ru-Ru	3.00802(4)	3.00819(4)	3.00839(4)	3.00847(4)
Ru-O	1.93805(2)	1.93577(2)	1.93767(2)	1.9365(12)
Bond Angle (°)				
Sr-O-Sr	126.300(27)	126.305(1)	126.275(1)	126.317(1)
Ru-O-Ru	101.94(9)	101.845(1)	101.974(1)	101.800(1)

Table.App.1.13: The refined parameters for the Nitrogen phases used to account for the nitrogen contamination within the NPD data collected at 50 K, for fields of 0.5, 3 and 7 T. These phases were fitted using the Le Bail method. P1 and P2 in the 7 T columns stand for phase 1 and phase 2 of the two nitrogen phases added to the 7 T refinements.

Refined parameter	0.5 T	3 T	7 T (P1)	7 T (P2)
$a = b$ (Å)	4.03539(22)	4.05701(31)	4.0302(4)	4.0634(4)
c (Å)	6.6582(6)	6.6159(6)	6.6274(11)	6.5869(8)
Cell volume (Å ³)	93.899(11)	94.305(13)	93.223(20)	94.189(18)

Table.App.1.14: The refined parameters for the Nitrogen phases used to account for the nitrogen contamination within the 0.5 T NPD data collected at 60 K. This phase was fitted using the Le Bail method.

Refined Parameter	Value
$a = b$ (Å)	4.04440(33)
c (Å)	6.6611(7)
Cell volume (Å ³)	94.360(15)

Appendix 2

Table.App.2.1: The calculated values for the volume magnetostriction over all fields and temperatures. Temperatures in brackets indicate the temperature at which the data was collected in cases where the temperature was not quite 100 and 150 K.

Temperature (K)	Applied Field (T)		
	0.5	3	7
	Magnetostriction ($\pm 5 \times 10^{-5} \lambda_V$)		
1.00	6×10^{-5}	7×10^{-5}	9×10^{-5}
10.00	12×10^{-5}	8×10^{-5}	15×10^{-5}
20.00	6×10^{-5}	4×10^{-5}	-
30.00	4×10^{-5}	3×10^{-5}	6×10^{-5}
40.00	6×10^{-5}	3×10^{-5}	-
50.00	5×10^{-5}	7×10^{-5}	9×10^{-5}
60.00	6×10^{-5}	4×10^{-5}	-
80.00	9×10^{-5}	-2×10^{-5}	12×10^{-5}
100.00	8×10^{-5}	16×10^{-5} (@94 K)	16×10^{-5}
150.00	10×10^{-5}	20×10^{-5} (@130 K)	23×10^{-5}

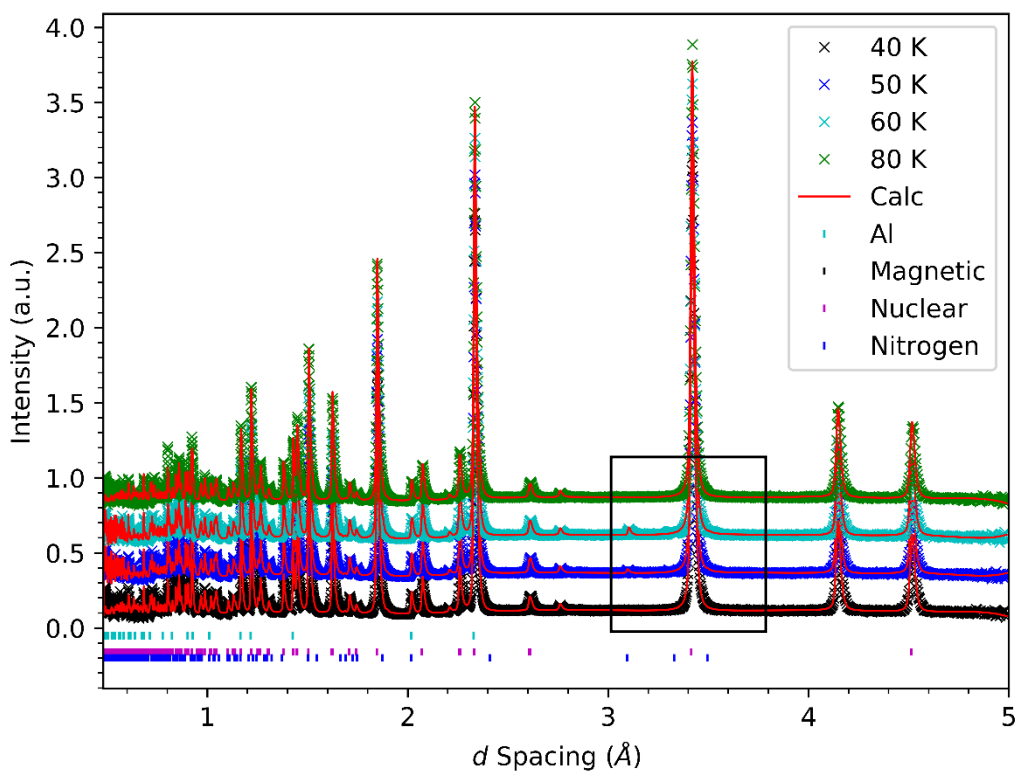


Fig.App.2.1a: Waterfall plot of Rietveld refinements of neutron powder diffraction data collected in an applied field of 0.5T, for a range of temperatures, from 40 to 80 K.

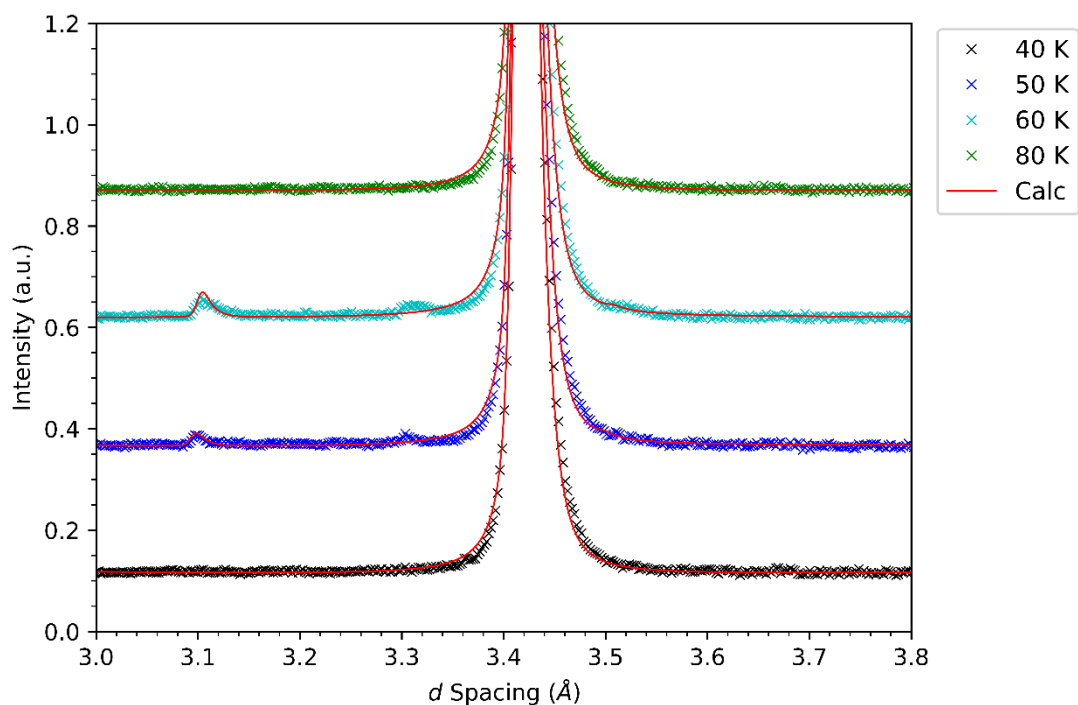


Fig.App.2.1b: Magnification of the outlined area in Fig.App.2.1a; of a waterfall plot of Rietveld refinements of neutron powder diffraction data collected in an applied field of 0.5T, for a range of temperatures, from 40 to 80 K.

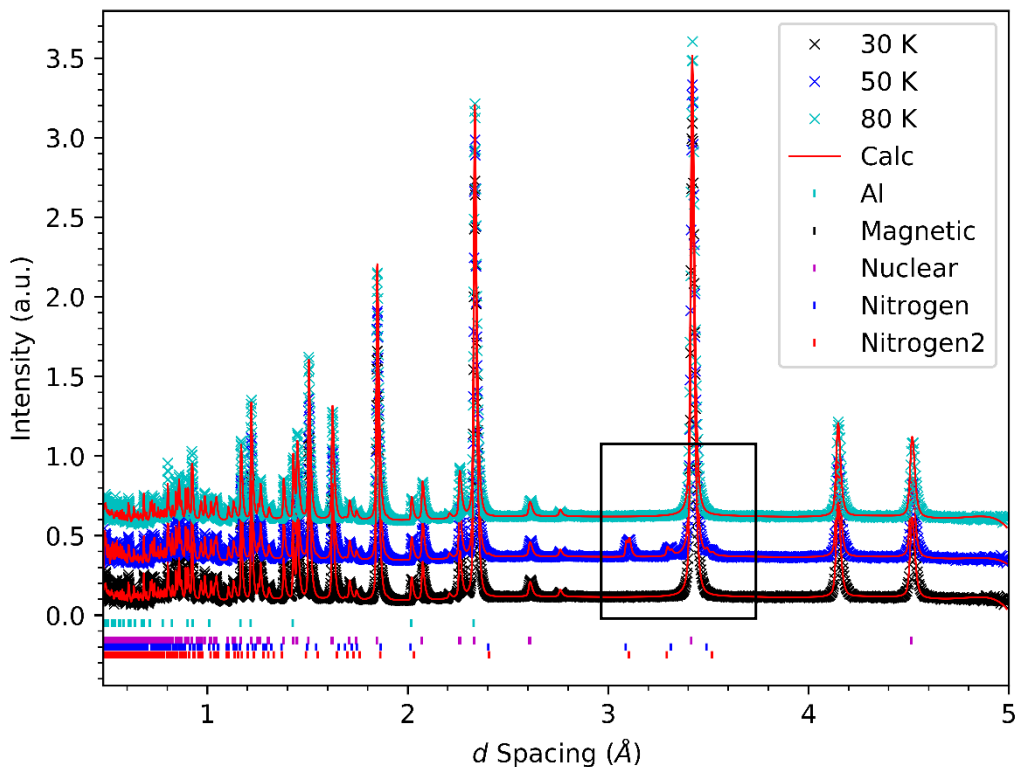


Fig.App.2.2a: Waterfall plot of Rietveld refinements of neutron powder diffraction data collected in an applied field of 7T, for a range of temperatures, from 30 to 80 K. Nitrogen 2 represents the second phase of nitrogen used to explain the peak splitting.

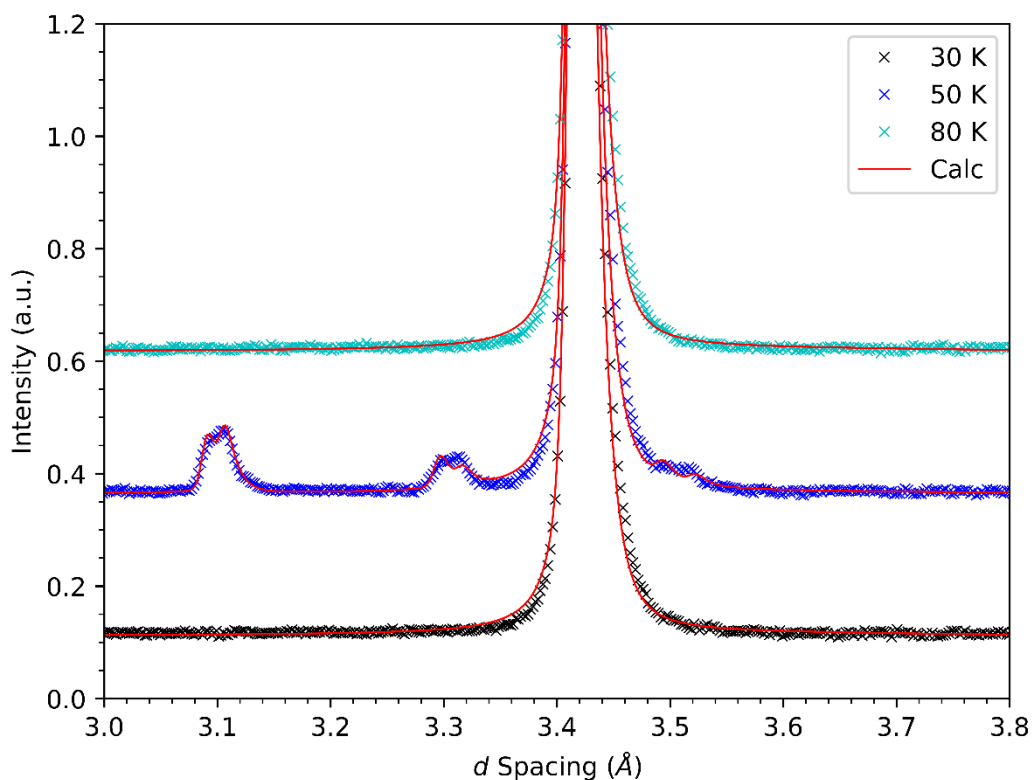


Fig.App.2.2b: Magnification of the outlined area in Fig.App.2.1a; of a waterfall plot of Rietveld refinements of neutron powder diffraction data collected in an applied field of 7T, for a range of temperatures, from 30 to 80 K.